IMPROVEMENTS TO WHOLE LENS RECONSTRUCTION FOR SALINE SUBMERGED SOFT CONTACT LENSES

by

Christopher J. Guido

A Thesis Submitted to the Faculty of the

COLLEGE OF OPTICAL SCIENCES

In Partial Fulfillment of the Requirements
For the Degree of

MASTER OF SCIENCE

In the Graduate College

THE UNIVERSITY OF ARIZONA

2016

STATEMENT BY AUTHOR

The thesis titled "Improvements to Whole Lens Reconstruction for Saline Submerged Soft Contact Lenses" prepared by Christopher Guido has been submitted in partial fulfillment of requirements for a master's degree at the University of Arizona and is deposited in the University Library to be made available to borrowers under rules of the Library.

Brief quotations from this thesis are allowable without special permission, provided that an accurate acknowledgement of the source is made. Requests for permission for extended quotation from or reproduction of this manuscript in whole or in part may be granted by the head of the major department or the Dean of the Graduate College when in his or her judgment the proposed use of the material is in the interests of scholarship. In all other instances, however, permission must be obtained from the author.

SIGNED: Christopher Guido

APPROVAL BY THESIS DIRECTOR

This thesis has been approved on the date shown below:

John E. Greivenkamp	Date
Professor of Optical Sciences	

ACKNOWLEDGEMENTS

I would like to acknowledge my wife Patricia along with my parents for their continuous support during my thesis work. I would also like to express my gratitude to my advisor Dr. John Greivenkamp for providing with me a challenging and rewarding project. Last but not least, I would also like to thank my friends and colleagues (both past and present) for providing me with the knowledge and motivation to move forward.

Table of Contents

List of Figures

List of Tables

The University of Arizona

ABSTRACT

College of Optical Sciences

Master of Science

By Christopher Guido

A method for measuring the thickness and surface profiles of soft contact lenses while submerged in a saline solution has been implemented utilizing a low coherence Twyman-Green Interferometer. Although the original measurements demonstrated that features on the contact lens surfaces could be accurately determined, it was believed that the layout of the system also induced surface profile distortions. A new opto-mechanical layout has been implemented which eliminates many of these low frequency distortions. Improvements to the original phase unwrapping algorithms have also been developed to overcome the low visibility output inherent to the measurement allowing for a more complete analysis of the two surfaces of a contact lens.

1 INTRODUCTION

In 1971, the first FDA-approved soft contact lenses were developed by Bausch and Lomb. Since then, the design of soft contact lenses has become increasingly complex in shape with the introduction of bifocal and toroidal lenses as well as in material with the introduction of silicone hydrogel lenses in 1999. Because of the nature of the silicone hydrogel, as well as the typical thickness of contact lenses (on the order of 100-200 μm), the ability to accurately compare the product to the design has become increasingly complex and more desirable (Greivenkamp et al., 2014).

In recent years, to ensure the performance of the contact lenses, several instruments have been developed with a notable contribution from CLOVER (Contact Lens Optical Verification). CLOVER is a Mach-Zehnder interferometer that measures the transmission wavefront from a submerged contact lens in saline solution (Williby, Smith, Brumfield, & Greivenkamp, 2003). It is necessary to submerge the contact lens in saline so that it retains the designed shape. Out of saline, the contact lens will begin to deform and buckle which will not provide the expected wavefront when in use.

To further improve upon the accuracy of CLOVER, two separate instruments were constructed to measure the index of refraction of the silicone hydrogel and the saline solution. A Hilger-Chance refractometer was designed to measure the refractive index of saline (Pixton & Greivenkamp, 2006) while a separate low coherence Twyman-Green interferometer paired with a Mach-Zehnder was designed to measure the thickness and index of the contact lens (Goodwin, 2007). This dual interferometer is referred to as Engage.

These devices provided much information for the performance of the contact lens; however, if there was an error in the emitted wavefront, it could not be pointed back to a particular defect on the contact lens surfaces. This led to the development of another low coherence Twyman-Green

Interferometer abbreviated as LOCOH (Heideman & Greivenkamp, 2016), (Heideman, 2014). LOCOH was successful in providing surface measurements as well as a thickness measurement.

Combined with Engage and the Hilger Chance refractometer, the results from LOCOH could be used to generate a 3D model of the contact lens which was referred to as whole lens reconstruction. A simulated transmitted wavefront could also be generated from the whole lens reconstruction and compared with the results of CLOVER for verification. Of course, there were still some features with LOCOH's first build that could be improved upon to provide more accurate results and robustness.

The design concepts, initial results, and limitations of the first build of LOCOH will be discussed in this paper in order to setup the background needed to understand the new design improvements put into place as well as the results that followed. This discussion will then be followed up with possible future improvements as needed.

2   LOCOH DESIGN

As mentioned earlier, LOCOH is a Twyman-Green interferometer; however, the complexity of LOCOH is beyond that of the classical Twyman-Green interferometer. To be more specific, LOCOH is a phase-shifting, low-coherence, polarization-splitting, non-null Twyman Green interferometer. In this chapter, a simple Twyman-Green layout will be built upon to develop an understanding of why the interferometer is designed to have these features as well provide an understanding to the benefits of each of these features.

2.1   Twyman-Green layout

A Twyman-Green interferometer is typically taught as having a collimated laser incident onto a beam splitter which divides the amplitude of the incident beam. The divided beams are then propagated down two different paths typically referred to as the test and reference paths. As the divided beam

propagates down each respective path, it is reflected by the reference and test surface, which send the

light back to the beam splitter. At this point, the two beams are recombined and redirected towards a

detector. This recombination of the beam provides an interference pattern which is directly relatable to

differences in the optical path lengths between each path. A schematic of this typical layout is shown in

Figure 2.1. Often an imaging lens system is used to magnify and observe the interference pattern.
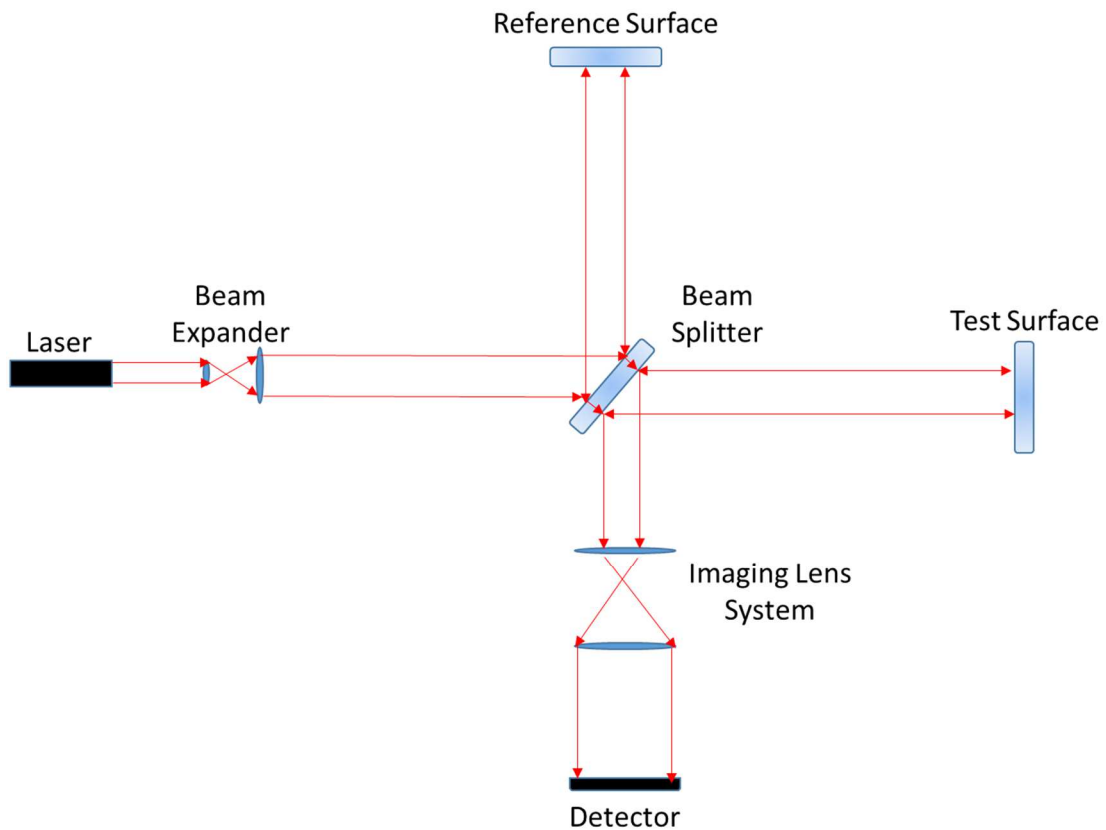
Figure 2.1) Typical Twyman-Green Layout

When the two beams interfere at the detector, periods of bright and dark fringes appear which

show constructive and destructive interference respectively. Bright fringes occur when the optical path

difference (OPD) between the arms is defined as

$$OPD_{TG} = 2(d_1 - d_2) = m\lambda \qquad \text{(2.1.1)}$$

Dark fringes occur when

$$OPD_{TG} = 2(d_1 - d_2) = m\left(\lambda + \frac{1}{2}\right) \qquad \text{(2.1.2)}$$

where d_1 and d_2 are the optical path lengths in the different arms , λ is the wavelength of the laser source, and m is an integer value.

In the example shown in Figure 2.1, the two mirrors are flat and any height deviation on the test mirror (relative to the reference mirror) can be determined from

$$OPD_{TG}(x_0, y_0) = 2(d_1 - d_2) - 2\epsilon(x_0, y_0) \qquad \text{(2.1.3)}$$

where ϵ is the height deviation from the nominal surface shape located at a particular x_0 and y_0. This equation can also be applied to non-flat surfaces such as two identical spheres or two identical aspheres; however, when generating complex optical surfaces such as aspheres, it is not common to have two identical surfaces. Typically, a reference flat is still used even with a non-flat test surface. To account for this change in surface shapes, an extra element must be placed in the interferometer such as a diverger lens system. The diverger lens system is placed in the test path to generate a wavefront that is nominally the shape of the measured surface.

Another element commonly found in interferometers is a compensation optic. The compensation optic is usually a window placed in the reference arm to account for OPL difference between the two arms as well as the dispersion properties of the diverger lens system. Often when using a laser, it assumed that the laser source is very narrow in bandwidth, so dispersion is not a common problem; however, if the laser source is replaced with a broader band source, this dispersion

correction is necessary for accuracy. This compensation plate and the diverger lens system mentioned previously is shown in Figure 2.2.
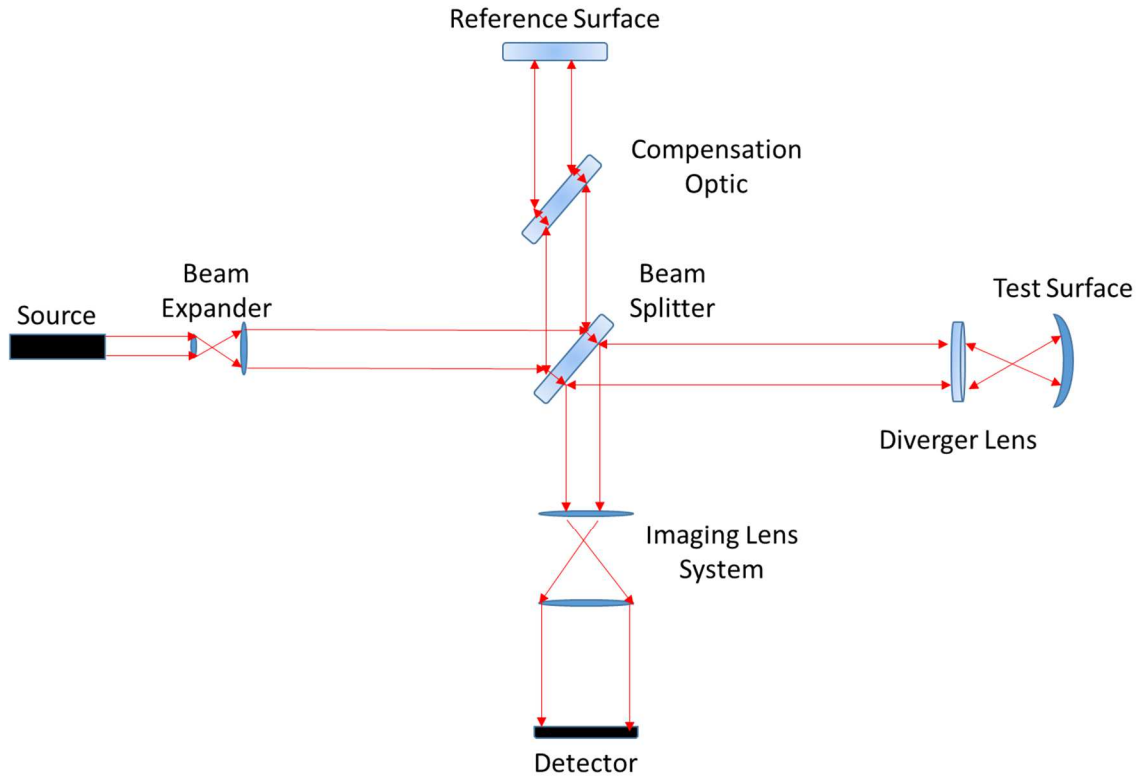
Figure 2.2) Twyman-Green Layout for a Non-Flat Test Surface

When the two wavefronts returning to the beam splitter from each path are intended to be relatively identical, this is referred to as null interferometry. Ideally, there are optimum positions for the test surface, relative to the reference surface, that will produce a single fringe or null fringe. In order for this to be valid for testing a curved surfaces against a flat reference, this would imply that the diverger lens system must produce a wavefront identical to the test surface. (To simplify things, the diverger lens system from this point forward will be referred to as "the diverger.") In this situation, the output wavefront from the diverger will come to focus at the center of curvature of the test surface. By doing so, the wavefront will reflect normal to the test surface, and all rays will back track along their original

trajectory. In this situation, the test path wavefront returns to the beam splitter collimated or as a flat

wavefront. An example is shown in Figure 2.3.
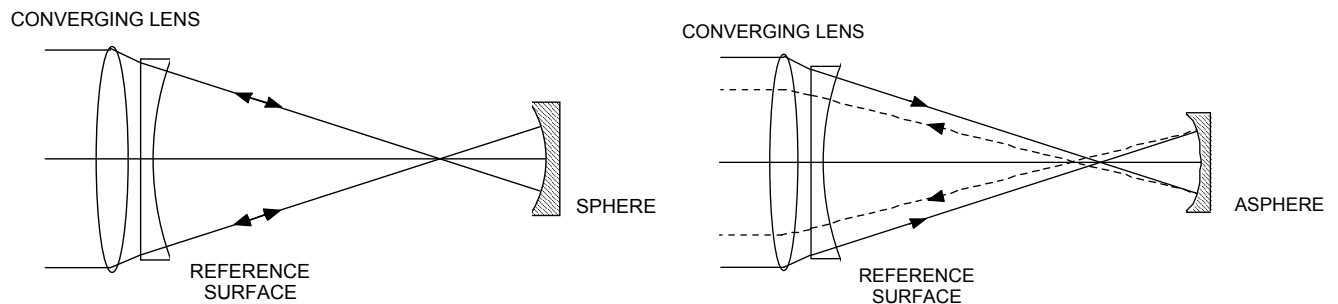
Figure 2.3) Diverger Lens
(Left) Null interferometer, (Right) Non-null interferometer

Also shown in Figure 2.3 is a diverger used in a non-null sense. Non-null interferometers use the

diverger to produce a wavefront that only nominally match the test surface. This allows for a variety of

test surfaces to be measured; however, the complexity required to determine the test surface shape

increases. The need to reverse ray trace is placed onto the interferometer and requires thorough

calibration of all surfaces used in the interferometer. (Jason D Micali & Greivenkamp, 2016)

Reverse ray tracing is an intricate topic that will only be briefly discussed here. The concept of

reverse raytracing is relatively simple to grasp but difficult to execute. By understanding that an

interferometer is nothing more than an imaging system, it can be understood that each active pixel in

the detector has a conjugate point on the nominal test surface produced by the diverger as shown in

Figure 2.4.
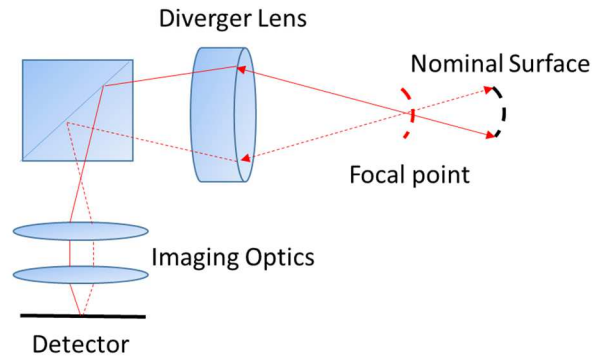
Figure 2.4) Detector and test surface as image conjugates

Unfortunately, if the actual surface deviates from the nominal wavefront surface generated by the diverger lens, the returning ray will accumulate an OPD error and will return to an incorrect pixel location. This will alter the fringe pattern generating a false representation of the actual surface deviations. For clarification, this is shown in Figure 2.5 where the blue dashed line is the actual return path of the solid red line. The image on the right of the figure is simply an enlarged image of the surface to help visual the OPD accumulation.
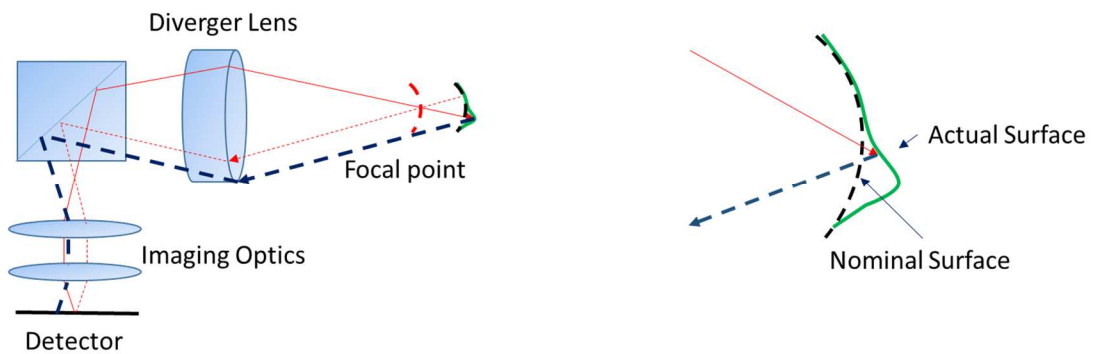
Figure 2.5) Deviation of Actual Surface from detector conjugate surface

Reverse ray tracing is typically an intensive algorithm which determines the errors introduced from incorrect ray propagations by projecting the measured OPD profile at the detector back to the nominal surface. For this to be successful, this requires a thorough characterization of the optical elements in

terms of their surface profiles, radii, thickness profiles, indices, and actual position relative to the detector. (Jason D Micali & Greivenkamp, 2016). As stated earlier, LOCOH is a non-null Twyman-Green which utilizes reverse ray tracing.

2.2   SLED source and Coherence Length

As shown previously, Twyman-Green interferometers utilize a laser source, and lasers are used due to the narrow bandwidth of their spectral output producing a highly coherent source. Coherence is defined as a statistical measure of how well light can interfere with itself. (Goodman, 2000) This statistical measure is often quoted as a coherence length, or coherence window, which can be quickly summarized as the range of distance that light can travel and still interfere with itself. A narrow bandwidth source such as a laser has a long coherence length which, when applied to the Twyman-Green, implies that the OPD between the two arms can have many orders of "m" in equation (2.1.1). Another way to think of coherence length is how much the optical path lengths (OPL's) in each arm can deviate from being identical. For example, if a laser has a coherence length of 1 meter, the OPL's in the test and reference paths can vary from nominally equal to within $\pm$ 500 mm. For most lasers, the coherence length is much longer than the thickness of the contact lens.

As stated in chapter 1, LOCOH was built with the intention to measure the surfaces of the contact lens. If the contact lens is placed in the test arm such that the posterior surface is to be measured, or interfered with the reference surface, the transmissive nature of the contact lens will still have light propagate past the posterior surface going towards the anterior surface. If the optical path lengths of the reference path and the test path up to the posterior surface are the same, the optical path length of the reference path and the test path up to the anterior surface are still within the coherence window of the laser. This implies that interference patterns from both surfaces will be projected onto the detector simultaneously, and the OPD error computed cannot accurately be matched to the surface errors of just

the posterior surface. In other words, the anterior and posterior surface errors are not isolated from one another when using a source with a coherence length longer than the contact lens thickness.

To decrease the coherence length, a broad-band source can be used in place of a laser. LOCOH uses a super luminescent light emitting diode, typically referred to as a SLED, to achieve a small coherence length. In particular, LOCOH uses the EXALOS (Langhorne, PA) SLED which has a Gaussian spectral distribution centered at 651.6nm with a 3-dB bandwidth of 5.9 nm. This gives a coherence length of approximately 57 μm using equation (2.2.1).

$$l_c = \sqrt{\frac{2}{\pi} \frac{\lambda^2}{\Delta\lambda}}$$
(2.2.1)

Since the coherence length of the source is less than the typical contact lens thickness, which is usually on the order of $75 - 200 \ \mu m$, this ensures that each surface will be isolated during measurements. This does lead to a constraint however between the reference arm and test arm optical path lengths. The two arms now must be path matched to within 57 μm to generate fringes at the detector plane.

2.3   Irradiance Balance and Polarization

Now that the Twyman-Green layout is understood, the next consideration to achieve a working interferometer is to have good visibility between the arms. Visibility is defined as a measure of the fringe modulation at the detector. If there is poor visibility between the arms, it will be difficult to obtain accurate measurements of the surface. Mathematically, visibility is defined by equation (2.3.1). (Schwiegerling, 2014)

$$V = \frac{I_{max} - I_{min}}{I_{max} + I_{min}} = \frac{2\sqrt{I_1 I_2} p_{12}}{I_1 + I_2}$$
(2.3.1)

I_1 and I_2 are the irradiance from each arm and p_{12} is the cross product of the Jones vector for the two beams. Thus if the beams are of opposite polarization, say one is linearly polarized in s and the other in p, there will be no interference between the beams and thus no visibility of the fringes.

Looking at equation (2.3.1), it can also be seen that if I_1 and I_2 are not well balanced, the visibility will also suffer. Looking at the two extremes, if the energy in each arm is equal, then the visibility will be at a maximum. In the situation where all of the energy is in one arm and not the other, there will be zero visibility. Using the same source, it is not possible to have a visibility greater than 1. Typically a visibility of 50% or 0.5 is consider adequate for most measurements (Hariharan, 2007).

In LOCOH, obtaining sufficient visibility is very challenging due to the low reflectivity of a contact lens in saline and the inherent stray light in the system. At normal incidence, the reflectivity of a contact lens is about 0.063% using equation (2.3.2) where n_1 = 1.336 for saline (Pixton & Greivenkamp, 2006) and n_2 = 1.405 for the hydrogel (Goodwin, 2007).

$$R = \left(\frac{n_2 - n_1}{n_2 + n_1}\right)^2$$

(2.3.2)

For the reference surface, an uncoated glass window made of N-BK7 is used in air which returns a reflectivity of about 4%.

Furthermore, there are also back reflections from the glass to air interfaces within the interferometer to consider. As an example, the test arm will have light back reflected from all 4 lenses in the diverger lens system. Even with high quality anti-reflection coatings placed on glass surfaces, about 0.25% of the incident light will still be reflected which is still 4 times larger than the contact lens reflection in saline. If it is assumed that every glass surface in the diverger lens assembly is coated with an anti-reflection coating that returns 0.25% of incident light, then the total light coming from the

contact lens back to the detector would only be approximately 0.061% of the total energy sent into the test arm. This approximation assumes only the 4 lenses in the diverger optics generate back reflections while the beam splitter and imaging optics transmit 100% of all energy. With these approximation, about 1.5% of the total light sent into the test arm will be reflected from the diverger lens system which is about 25 times the amount of light from the contact lens. This will obviously drown out the contact lens signal.

To ensure that the contact lens signal is not lost at the detector from the other back reflections, polarization control is used. Two orthogonal linear polarization states are sent from the SLED to a polarizing beam splitter and the amount of power in each state is controlled by a half wave plate. This ensures that there is equal return irradiance from each arm to maximize visibility. To have the return beams move towards the detector, a quarter wave plate is used to turn the input linear polarization circular. Upon reflection from either the test or reference surface, the return beams will pass the quarter wave plate again and switch to the orthogonal linear polarization state allowing each arm to send light back towards the detector. Since they are of orthogonal polarization, the light will not interfere. In order to generate interference at the detector, a linear polarizer with its fast axis at 45°, relative to the two incoming polarization states, is placed prior to the detector to extract the common component in both states. This is shown in Figure 2.6.
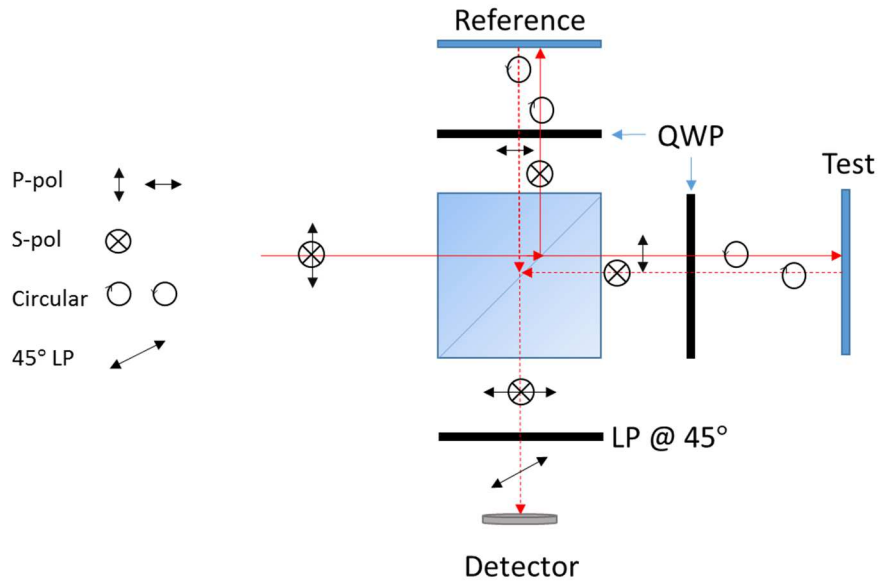
Figure 2.6) Polarization Splitting Interferometer

The option of where to put the quarter wave plate in the test arm is critical for maximizing

visibility. If the wave plate is placed prior to the diverger lens, all reflections from the diverger lens will

be sent back to the detector which does not solve the visibility problem. Since only the signal from the

contact lens is desired, it would be ideal to place the quarter wave plate after the diverger lens but prior

to the contact lens. That way, only the light reflected from the contact lens has its polarization state

altered to make it back to the detector. The stray reflections prior to the waveplate will maintain their

original polarization and not get to the detector. A new problem that arises from placing the quarter

wave plate there is that the stray reflections will now move back to the laser. This could damage the

SLED if unchecked. To ensure that this doesn't happen, a Faraday Isolator is placed after the SLED

(Heideman, 2014).

One last stray light design that should be considered is that actual surface shape of the lenses in

the diverger lens system. The design of the diverger lens was done to produce a particular wavefront to

match a nominal aspheric shape from the contact lenses. It was also designed to minimize stray light

back at the detector. In short, the curved lens surfaces were designed such that some of the light back

reflected would vignette in the system before reaching the detector. This would lower the background

DC signal on the detector to allow for a more sensitive readout of the actual contact lens signal.

2.4   Phase shifting and phase unwrapping

Another critical component to the LOCOH interferometer is phase shifting. When a static fringe

pattern is captured by the detector, there is no way to determine if the curvature measured is towards

the interferometer or away. By translating one surface by a known axial distance, the fringe pattern will

shift and the direction of the measured curvature can be determined. This axial translation of one path

is known as a phase shifting. Prior to phase shifting interferometry, interferograms were measured by

tracing along a fringe after finding the center of that fringe which was not always easily determined

(Schwiegerling, 2014).

The initial build of LOCOH utilized the Carré phase shifting algorithm (Schreiber & Bruning, 2007);

however, there are many different phase shifting methods which can be found in literature. The

irradiance given at the detector from the interfering beams is described by equation (2.4.1)

$$I(x_0, y_0; m) = I_{DC} + I_{AC} \cos\left(\frac{4\pi}{\lambda}\epsilon(x_0, y_0) + \gamma - \frac{\boldsymbol{4\pi(m)\Delta_d}}{\boldsymbol{\lambda}}\right)$$

(2.4.1)

$$I_{DC} = I_1 + I_2 \qquad I_{AC} = 2\sqrt{I_1 I}_2 \qquad \gamma = 2(d_1 - d_2)$$

Note that (m) is an integer value and Δ_d is an axial propagation distance from the nominal

position. The bolded portion of equation (2.4.1) is the only portion that will change when the OPL in one

arm is shifted. Unlike the classical 4-step method, the Carré method does not use a known phase step

but solves for it in its algorithm. Consider 4 different measured irradiances.

25

$$I_1' = I'(x_0, y_0; 0) = I_{DC} + I_{AC} \cos\left(\frac{4\pi}{\lambda}\epsilon(x_0, y_0) + \gamma - 3\alpha\right)$$

$$I_2' = I'(x_0, y_0; 1) = I_{DC} - I_{AC} \sin\left(\frac{4\pi}{\lambda}\epsilon(x_0, y_0) + \gamma - \alpha\right)$$

$$I_3' = I'(x_0, y_0; 2) = I_{DC} - I_{AC} \cos\left(\frac{4\pi}{\lambda}\epsilon(x_0, y_0) + \gamma + \alpha\right)$$

(2.4.2)

$$I_4' = I'(x_0, y_0; 3) = I_{DC} + I_{AC} \sin\left(\frac{4\pi}{\lambda}\epsilon(x_0, y_0) + \gamma + 3\alpha\right)$$

Note that α is an arbitrary step size and the steps are done in 2α intervals. Careful observation of the 4

equations will develop in

$$\alpha(x_0, y_0) = \tan^{-1}\left(\sqrt{\frac{3(I'_2 - I'_3) - (I'_1 - I'_4)}{(I'_1 - I'_4) + (I'_2 - I'_3)}}\right)$$

(2.4.3)

which ultimately leads to

$$\epsilon(x_0, y_0) = \frac{\lambda}{4\pi}\left\{\tan^{-1}\left(\frac{\sqrt{[3(I'_2 - I'_3) - (I'_1 - I'_4)][(I'_1 - I'_4) + (I'_2 - I'_3)]}}{(I'_2 + I'_3) - (I'_1 + I'_4)}\right) - \gamma\right\}$$

(2.4.4)

Equation (2.4.4) relates the surface figure error back to the 4 phase shifted interferograms;

however, it is not without complications. When determining the surface error, the arctangent operation

will have to be used, which has an ambiguity of 2π. This will cause the phase to be trapped between π

and $-\pi$ where phase is defined as

$$\psi = \frac{4\pi}{\lambda}\epsilon(x_0, y_0) + \gamma$$

(2.4.5)

This restricted phase is known as wrapped phase. Figure 2.7 and Figure 2.8 show an example of

wrapped phase in one and two dimensions respectively. As it can be seen, it is highly misrepresentative

of the true phase which represents the actual surface.

26
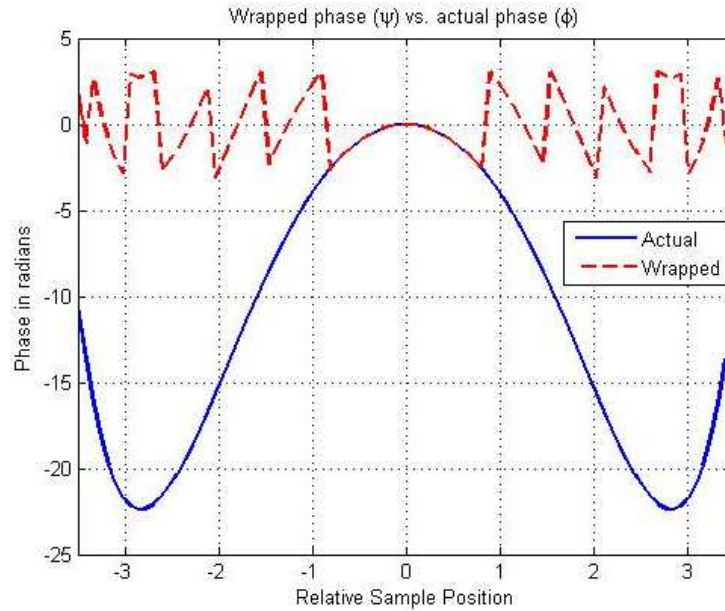
Figure 2.7) 1D Wrapped phase
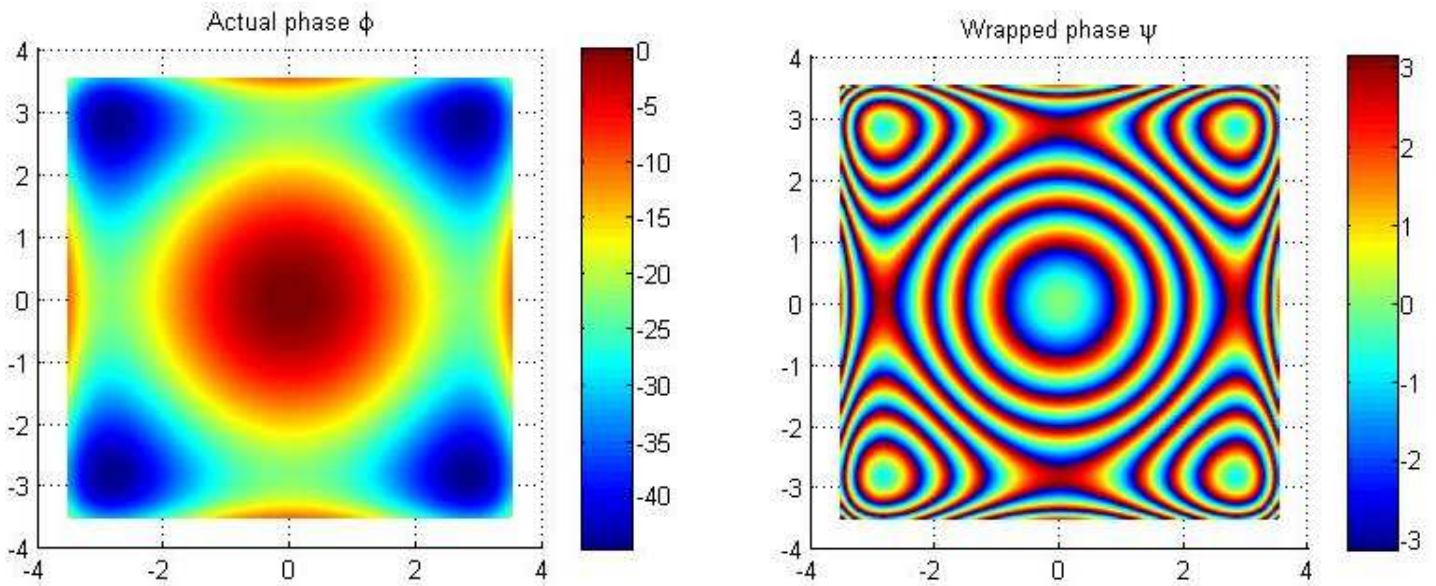
Figure 2.8) 2D Wrapped Phase

The algorithm necessary to unwrap the phase and get the actual phase is quite simple in concept but difficult in practice. There are many different phase unwrapping algorithms, but the base concept is similar. Starting at a seed point, the algorithm checks the slope of the surface at an adjacent point and if that point generates a slope with a magnitude greater than π, an interger value of 2π will either be

subtracted or added to that particular point. Though this is simple to understand, it is often difficult to find the appropriate seed point and get around the noise or lack of data in an array. Many different methods for getting past these issues, such as path following methods or minimum norm methods are discussed in literature and are outside of the scope of this paper (Ghiglia & Pritt, 1998). The initial build of LOCOH utilizes a quality-threshold raster scanning method to phase unwrap. Further details on this method are presented in chapter 7.

2.4.1 Methods of phase shifting

Phase shifting can occur through several methods. Some methods require moving a particular component a known distance while others are instantaneous and have no moving components. Consider Figure 2.9; a piezo-electric transducer (PZT) is placed in the reference path which can alter the OPL along the reference arm by translating a fold mirror. Having the PZT move the fold mirror allows for phase shifting; however, the repeatability and precision of the PZT greatly affects the accuracy of the surface measurement. If the phase acquisition method, such as the Carrè method, assumes equal phase steps, but the PZT does not alter the OPL equally every time it steps, print through errors can be seen in the unwrapped profiles. These errors will look similar to the wrapped profile of the acquired phase.
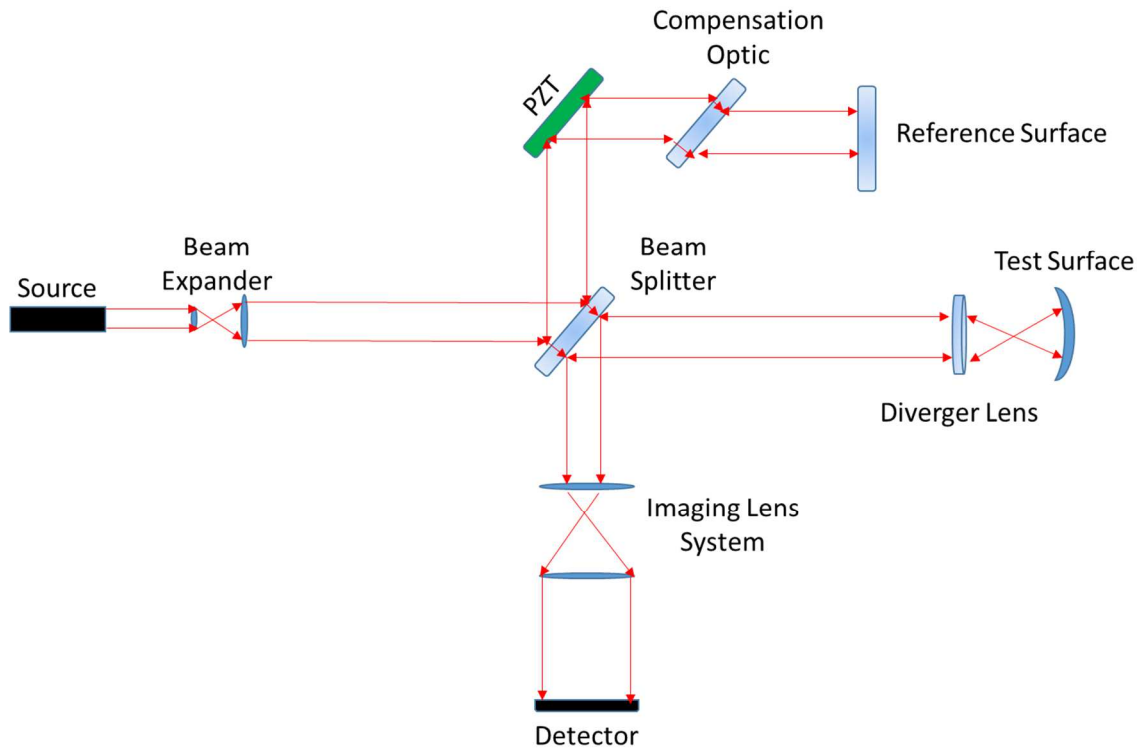
Figure 2.9) Phase Shifting Twyman-Green

A well-developed method for instantaneous phase shifting utilizes an array of polarizers placed in front of a detector such that each pixel has a corresponding linear polarizer. The polarizers are set up in grids of 4 and with circularly polarized light incident. By staggering the direction of the individual linear polarizers in the pattern shown in Figure 2.10, each super pixel (a 4x4 array of pixels) can receive 4 phase shifted interferograms instantaneously. These interferograms will have much less dependence on the lab environment and provide rapid results. (Millerd et al., 2004)
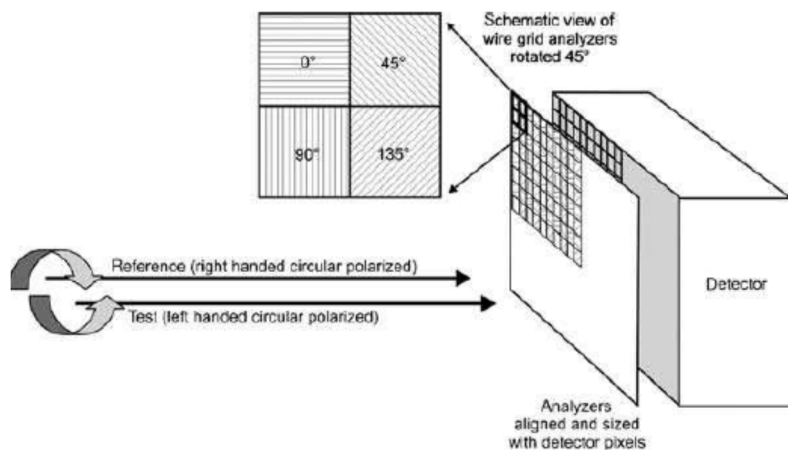
Figure 2.10) Polarized pixel array for instantaneous phase shifting
(Schreiber & Bruning, 2007)

Though this instantaneous method is robust and less sensitive to mechanical errors, LOCOH

utilizes a PZT to achieve its phase shifting.

2.5   Measurement and whole lens reconstruction

As mentioned previously, the goal of LOCOH was not only to take surface measurements; it was

also intended that enough data be captured to generate a 3D model of the lens known as whole lens

reconstruction. In order to achieve enough data to create a whole lens reconstruction, at least 4

separate measurements are needed. Two of these measurements are a cat's eye measurement, and one

is taken per surface. This cat's eye measurement occurs when the wavefront coming from the diverger is

focused directly onto the surface under test. Since the focal point occupies a very small area of the

contact lens surface, the contact lens area over that focal point spot size can be thought of as being

nearly flat. Therefore, the OPD of the test and reference arm can be easily tuned such that a single null

fringe occurs. This would imply that the OPD generates mostly destructive interference. By looking for

this null fringe, the cat's eye position can be easily found.

Since it is required to measure both surfaces of the contact lens and because the contact lens is not removed and repositioned in the mount, the cat's eye measurement for the second surface requires that the beam is refracted through the first surface of the contact lens. By moving the contact lens to generate an interference pattern with the same reference window position, the thickness measurement can be inferred from the actual distance the contact lens has translated and its refractive index. Figure 2.11 shows the contact lens position relative to the diverger's focal point for cat's eye on both surfaces.
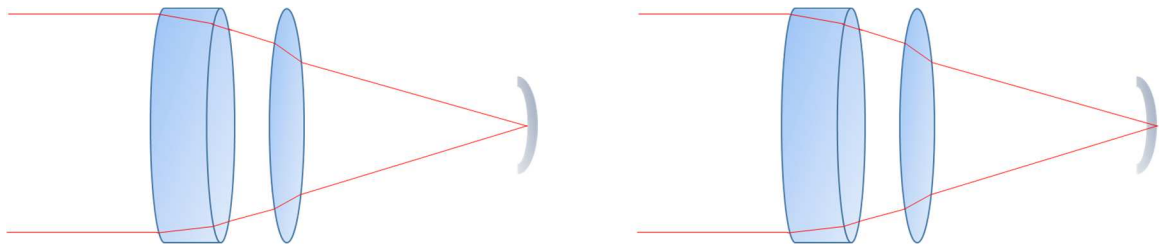
Figure 2.11) Cat's eye for both surfaces of a contact lens

After taking the cat's eye measurement, the contact lens is translated axially away from the diverger lens such that the beam is focused at the nominal radius of the contact lens. This is where the second measurement occurs and is known as the confocal measurement. By having the diverger come to focus at the radius of curvature of a surface, a larger portion of the surface area can be scanned than what was seen at the cat's eye position. This allows for the determination of surface variations. As with the cat's eye measurement, each surface is measured in a confocal state so to measure the back surface of the contact lens requires the rays to refract across the first surface. This is shown in Figure 2.12.

31
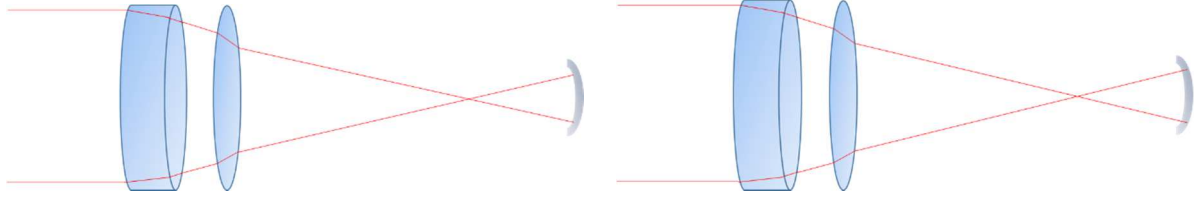
Figure 2.12) Confocal for both surfaces of the contact lens

The diverger lens in LOCOH is designed to measure at least 6mm in diameter across the contact lens surface. For reference, a contact lens is typically 14 mm in diameter. When processing the data, it is critical to determine the first surface shape prior to the second so that the errors induced by it are loaded into the reverse ray tracing algorithm. Also note that by taking a cat's eye measurement first, the radius of the surface and absolute aperture covered by the confocal measurement can be determined. The radius is simply the difference between the cat's eye and confocal position.

Thus, to summarize, each surface radii, the surface profiles, and the central thickness can be recovered by taking two cat's eye measurements and two confocal measurements. With these five known parameters, as well as prior knowledge or an assumption of the contact lens refractive index, a complete 3D model of the lens can be generated.

3   INTERFEROMETER COMPONENTS

All critical components of LOCOH have been discussed previously, and Figure 3.1 shows the first build of LOCOH. As it can be seen, the SLED is collimated by a fiber collimator followed by the half wave plate to control the irradiance in each arm. An isolator is placed prior to a spatial filter to prevent the back scattered light from interfering with the SLED. The spatial filter eliminates high frequency noise in the laser beam as well as expands it to roughly a 2 inch diameter with the aid of the collimating lens. The polarizing beam splitter divides the amplitude of the source between the two arms which is reflected

back through the beam splitter as explained in section 2.3. The imaging lens prior to the detector is a set

of relay lenses which is configured in an afocal fashion. The afocal imaging system is also doubly

telecentric in order to control the magnification at the detector. Following the afocal lens system is the

linear polarizer necessary to generate interference fringes and the camera used is the Manta G-283B

from Allied Vision (Exton, PA).
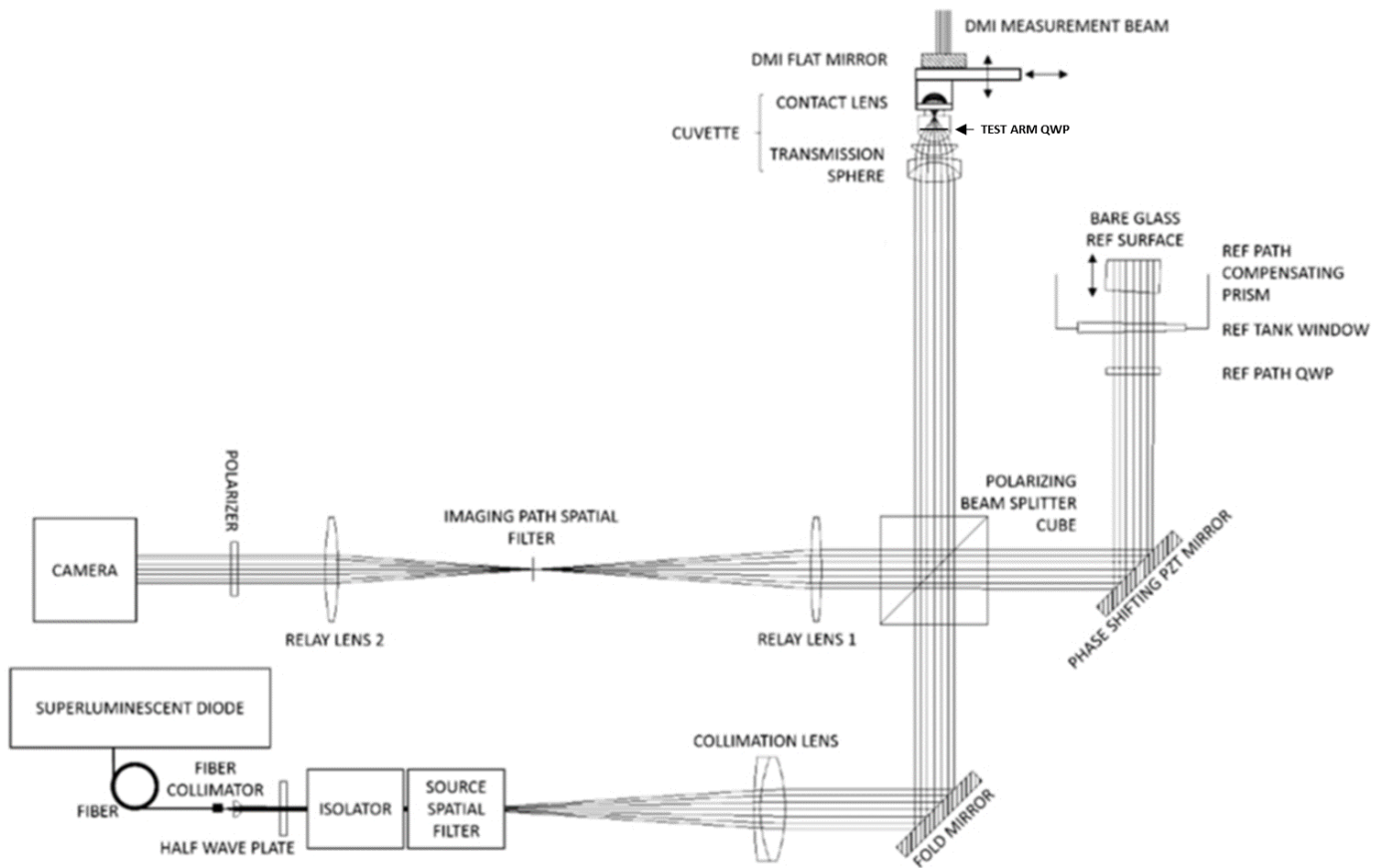
Figure 3.1) LOCOH

3.1   The reference arm

The reference arm consists of a 3" PZT fold mirror, a quarter wave plate, and the reference tank

assembly. The reference tank assembly holds saline similar to the test arm to ensure that the OPL

between itself and the test arm are similar. The reference tank assembly can be broken down into two

main components, the tank itself and the reference prism which contains the reference surface. This is

shown in Figure 3.2. The reference prism is axially translated using a Thorlabs (Newton, NJ) MTS50-Z8

linear stage. The stage has a range of 50 mm, so the arm is setup such that interference at both cat's eye

and confocal for the surfaces of the contact lens can occur within the linear stage's range.
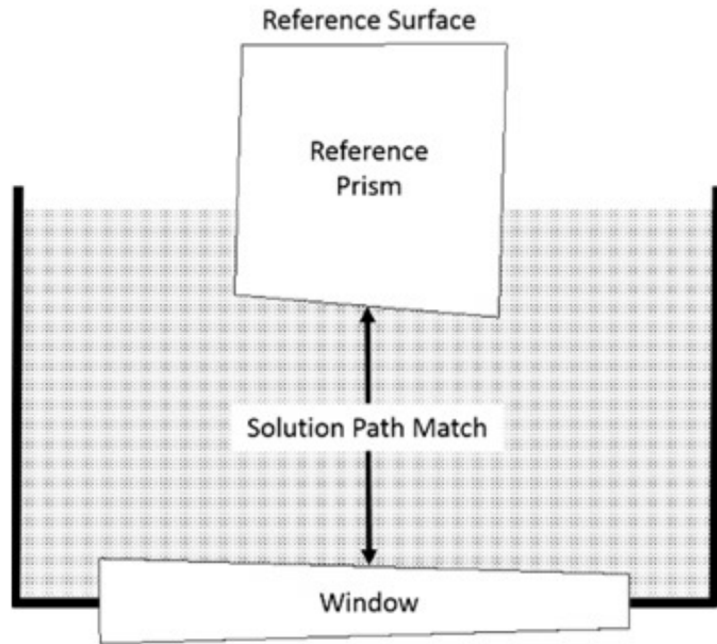
Figure 3.2) Reference Tank Layout

The tank is made out of Mil-A-8625, class 2, type II anodized aluminum and has a wedged N-BK7

window to allow light to pass into the saline solution. By introducing the wedge in the window, any stray

reflected beams will be directed away from the nominal axis and vignette before reaching the detector.

Because the window is wedged, the beam will deviate by an angle defined in equation (3.1.1) where α is

the wedge angle of the window.

$$\delta = -(n-1)\alpha$$

(3.1.1)

Since the beam is now propagating along a deviated path, the reference prism has a counter wedged

surface so the beam will return along the nominal path when it refracts into the prism. The last surface

34

is flat and ideally normal to the beam propagation so that a flat wavefront is sent back towards the detector (after passing through the wedges a second time).

The reference prism also serves the purpose as the compensation optic as discussed in section 2.1. The amount of glass in the reference prism is approximately the same as the amount of glass used in the diverger lens to account for dispersion.

3.2   The test arm

The test arm consists of the diverger lens, a quarter wave plate, the contact lens mount, and a distance measuring interferometer (DMI) from Zygo (Middlefield, CT).

In the first build of LOCOH, the mechanical housing for the diverger lens was also attached to the test arm tank. O-rings were placed between the lenses and their retaining rings to apply even force while also ensuring that the saline solution did not leak through the lens barrel. Like the reference tank, the housing is made of the same anodized aluminum that could withstand the saline.
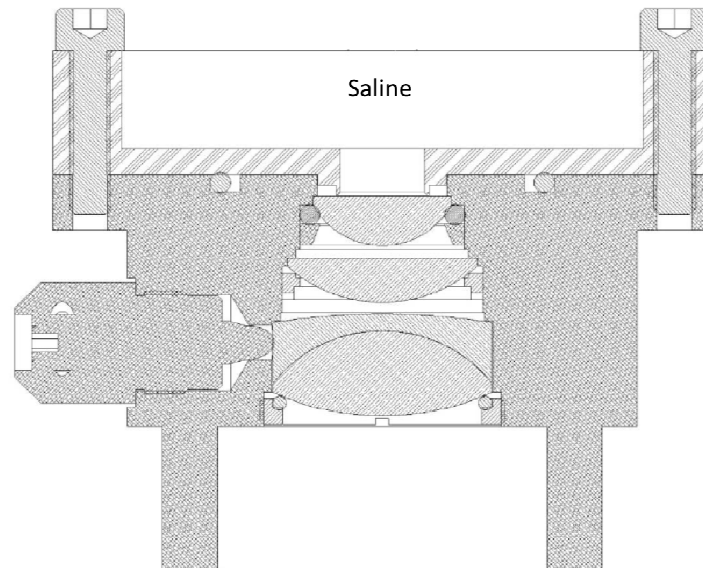
Figure 3.3) Test Arm Diverger Lens/ Tank assembly

The quarter wave plate used in the test arm is a sheet of film (APQW92-003-PC-165NM) from American Polarizers Inc. (Reading, PA). This is different from what is used in the reference arm. The waveplate sits on the last surface of the diverger lens assembly and can be rotated within the tank, but is not secured down.

The contact lens sits on a glass plate that is held in place by three arms. The three arms are attached to two Newport (Irvine, CA) AG-LS25 piezo motor driven linear stages to allow 50nm steps over a 12mm travel range in the axes orthogonal to the beam propagation axis. These stages are in turn attached to another Thorlabs (Newton, NJ) MTS50-Z8 50 mm linear stage, as used in the reference arm, so that the contact lens can translate along the beam propagation axis.

Since it is critical to know the distance the contact lens has travelled along the beam propagation axis, a DMI from Zygo (Middlefield, CT) is mounted such that it can measure the translation of the contact lens mount. The DMI can accurately measure the translation down to 10nm whereas the Thorlabs stages were measured to have an encoder error of 10-40 microns.

4   DATA ACQUISITION PROCESS

Now that the hardware is understood, the results of the first build can be discussed. All position data as well as captured images were obtained and stored using a custom graphical user interface (GUI) developed in IDL 8.3 (Exelis Visual Information Solutions, 2013）. Afterwards, the data was moved to a more powerful machine to be processed (stitched, phase unwrapped, reverse raytraced, and Zernike fitted) in another custom GUI also developed in IDL 8.3.

4.1   Four frame data, Unwrapping, and Stitching

As mentioned in section 252.4, LOCOH utilizes phase shifting. In particular, when an image is

acquired, 5 different frames of fringes are captured. Only 4 are used for equation (2.4.5) so the 5th frame

of data is often ignored. Figure 4.1 shows 4 frames of raw irradiance data taken from a single surface

measurement of a Etafilcon-A contact lens. It is difficult to see, but the fringes in each frame are slightly

offset from one another laterally. An area where the pixels are black in the first frame will lighten to

white by the fourth frame. In other words, a pixel will vary its signal with each phase shift.
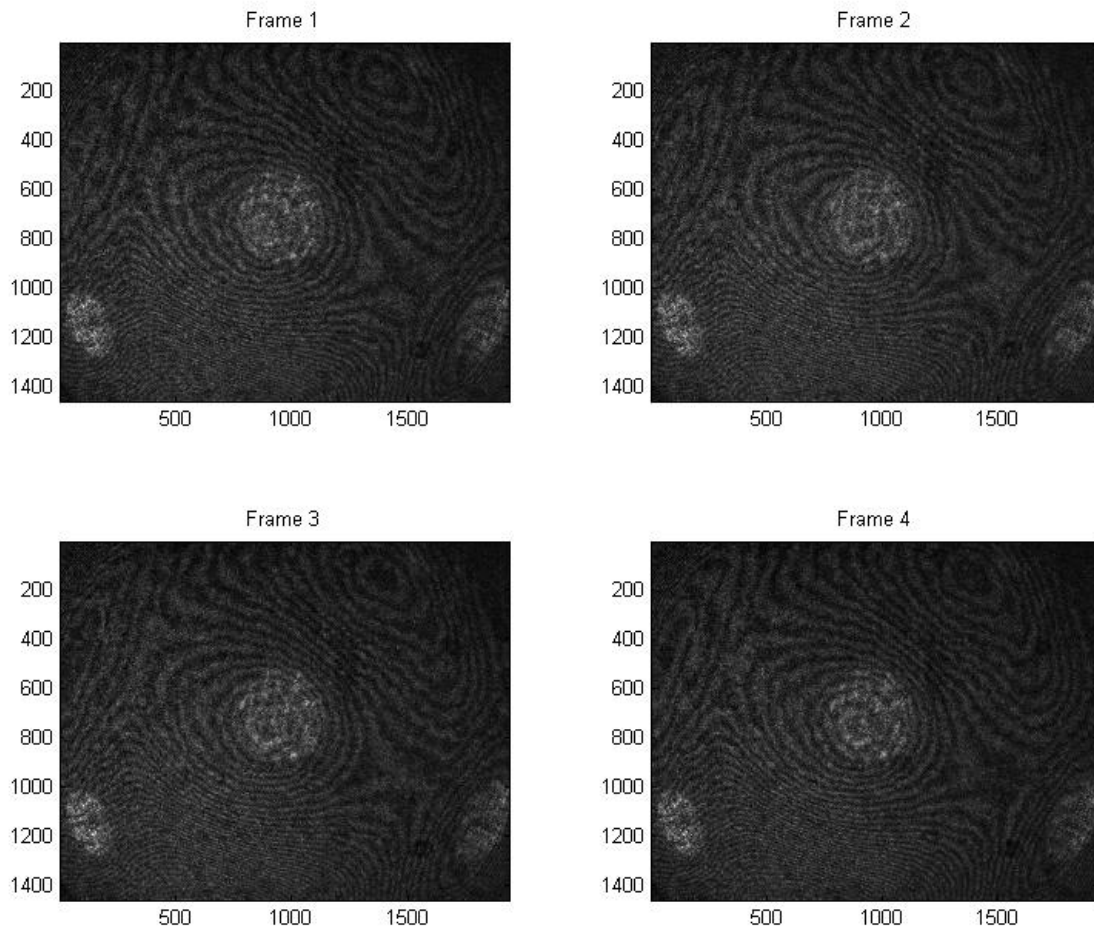
Figure 4.1) Single Confocal raw measurement

After the 4 frames are acquired, they are combined using equation (2.4.5) to generate the wrapped phase shown in Figure 4.2. Afterwards, the wrapped phase is unwrapped and stored to the side to be reverse ray traced. This unwrapped phase is shown in Figure 4.3. It should be noted that the white regions that appear in the unwrapped images are regions where the phase could not be unwrapped. This is either due to phase residues, noise, or lack of data at that pixel due to a high fringe frequency. Phase residues are regions where the value of the pixel suffers from an π ambiguity that cannot be resolved. While unwrapping, these residues will cause the algorithm to propagate errors so they are generally avoided. More information on this is discussed in section 7.1. It should also be noted that the hot spot in the center of the image is actually unwrapped but beyond the threshold values of the display, so it appears white. This data is actually taken into account for the true surface profile.
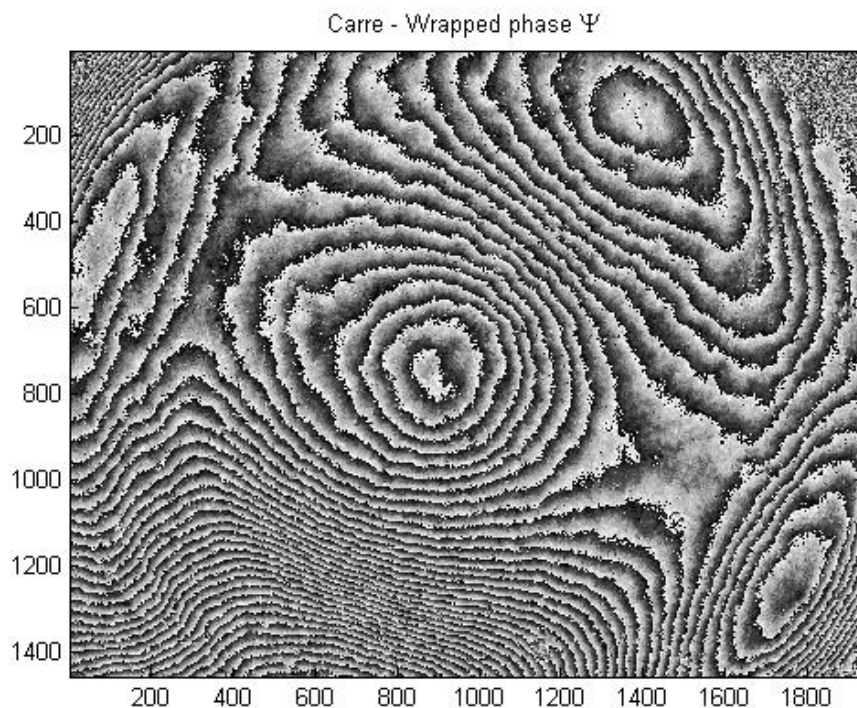
Figure 4.2) Wrapped phase of the 4-frame raw data
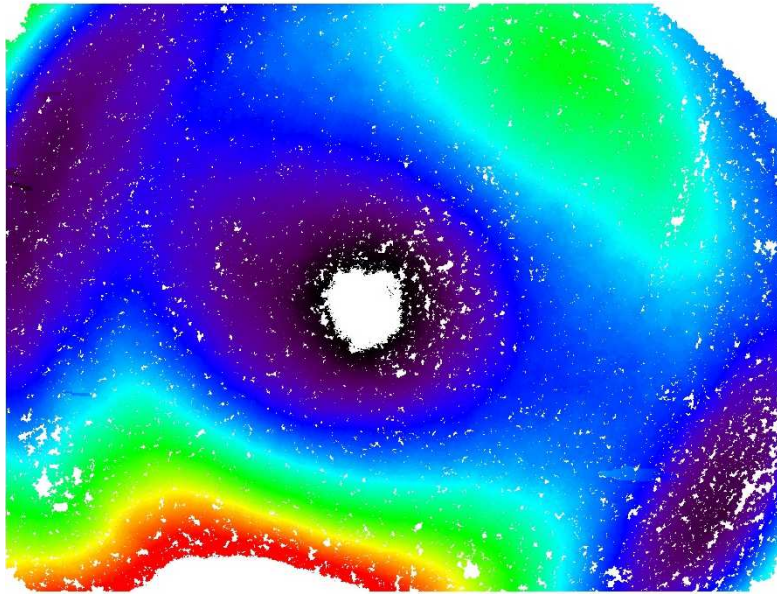
Figure 4.3) Unwrapped phase of the 4-frame raw data

With almost all data acquired in LOCOH, multiple sets of 5-frame fringe data are acquired per surface measurement and stitched together with one another. Stitching is a technique which segments the entire aperture to acquire surface slope data when the fringe spacing is too small (D Malacara, Creath, Schmit, & Wyant, 2007). By defocusing, areas where high frequency fringe spacing occur can achieve lower frequency at the cost of increasing the frequency in other regions. By knowing the amount of defocus, the entire aperture can be scanned over several defocus distance and recombined to create the actual surface. Figure 4.4 is taken from Malcara's "Optical Shop Testing" to demonstrate defocusing vs. fringe frequency. In image (a), the outer middle zones would not be unwrapped due to high fringe frequency. By defocusing a known amount, the middle region will start to have lower frequency as shown in image (b).

39
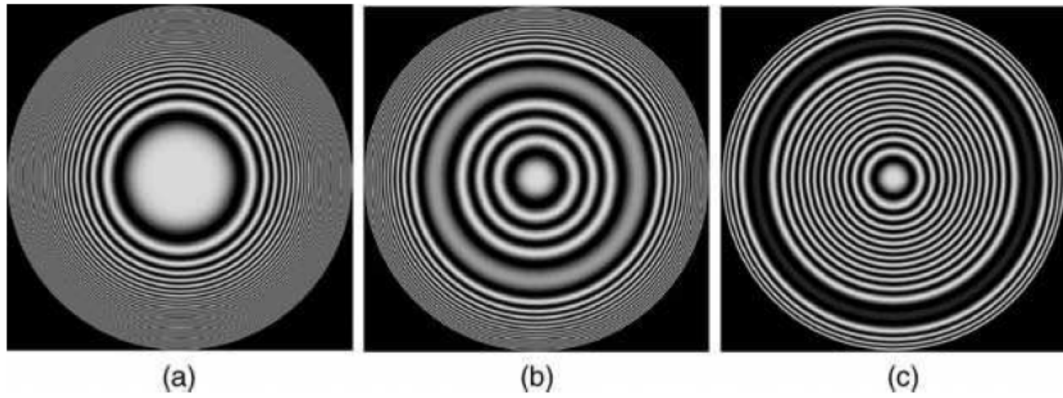
Figure 4.4) Fringe frequency vs. defocus
(D Malacara et al., 2007)

4.2 Reverse Ray tracing

After stitching the multiple images together, a surface profile is generated that represent the wavefront at the detector. This is still not the true surface profile however. As mentioned in section 2.3, reverse ray tracing is performed to remove the interferometer induced errors. Figure 4.5 and Figure 4.6 show a surface profile prior to reverse ray tracing and afterwards respectively. By reverse ray tracing, the general shape of the wavefront profile has undergone a drastic change. The horizontal and vertical scales shown in Figure 4.6 are in millimeters whereas the color bar is shown in microns.
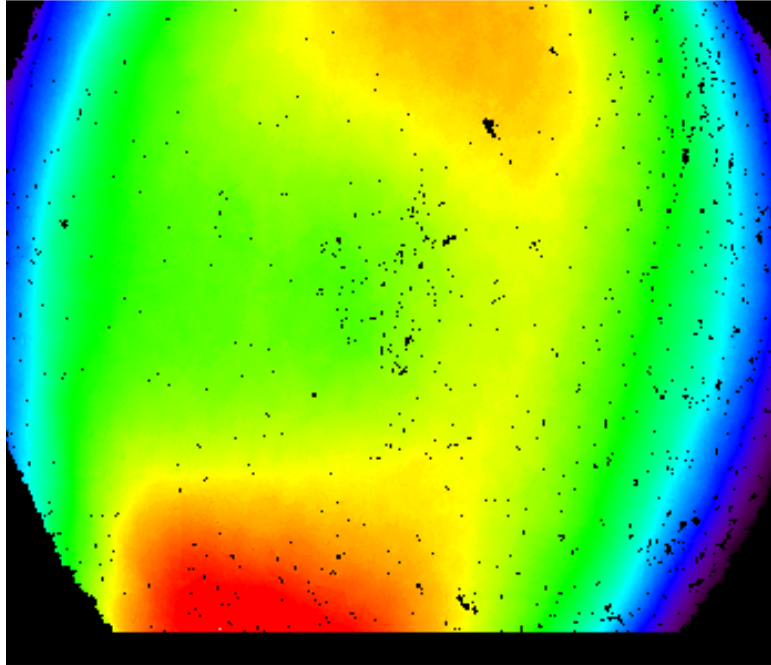
Figure 4.5) The stitched wavefront measured at the Detector
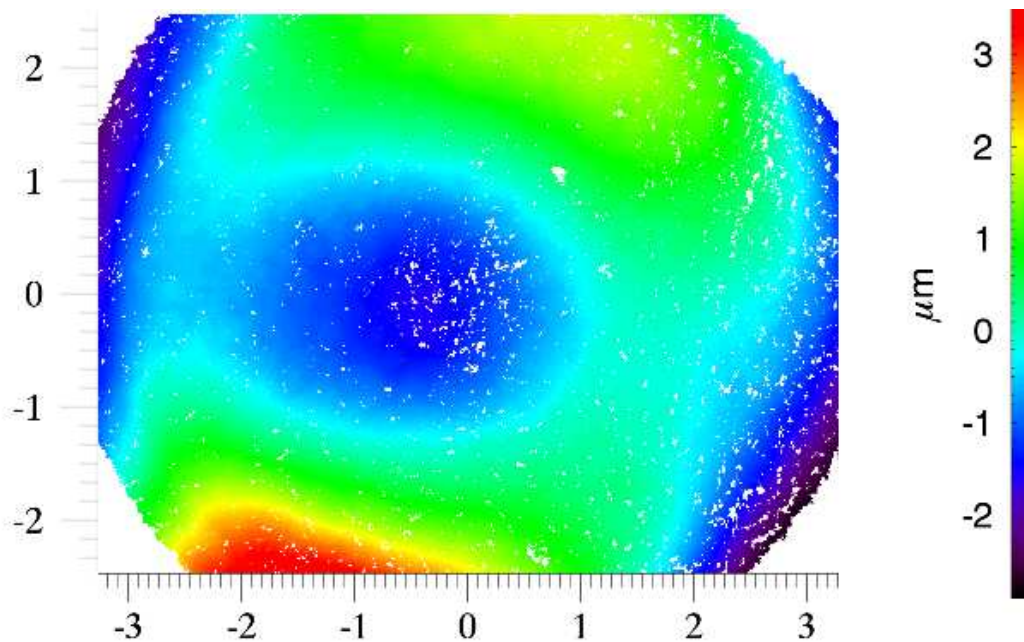
Figure 4.6) The stitched wavefront after reverse ray-tracing

4.3   Zernike Removal

Figure 4.6 displays the surface profile of the contact lens; however, there is interest in viewing high

frequency surface variations than just getting the general surface shape. To see these higher frequency

variations, Zernike polynomials are generated to represent the surface. These polynomials are then

subtracted from the surface to give a residual error of the surface which describes the higher frequency

variations.

Zernike Polynomials are two dimensional polynomials that are orthogonal over the unit circle. They

are useful for describing surface errors and can be related back to the Seidel aberrations. The first 15

orders of the Zernike expansion describe all the third order aberrations such as spherical aberration,

coma, astigmatism, field curvature, distortion as well as tilt and defocus. Table 4-1 below list the

polynomial equations and Figure 4.7 shows the mapping of the same polynomials over the unit circle.

Note that ρ is the ratio of the radial distance a point is within the pupil over the overall radius of the

pupil ($\rho = \frac{r}{R_p}$) and θ is the angle the radial arm makes with respect to the azimuth.

Table 4-1) First 15 Orders of the Zernike Polynomial expansion (Schwiegerling, 2014)

Order	$Z_n^m(\rho, \theta)$	Aberration Name
0	1	Piston
1	$2\rho \sin\theta$	Vertical Tilt
2	$2\rho \cos\theta$	Horizontal Tilt
3	$\sqrt{6}\rho^2 \sin2\theta$	Oblique Astigmatism
4	$\sqrt{3}(2\rho^2 - 1)$	Defocus
5	$\sqrt{6}\rho^2 \cos2\theta$	Horizontal Astigmatism
6	$\sqrt{6}\rho^3 \sin3\theta$	Oblique Trefoil
7	$\sqrt{8}(3\rho^3 - 2\rho)\sin\theta$	Oblique Coma
8	$\sqrt{8}(3\rho^3 - 2\rho)\cos\theta$	Horizontal Coma
9	$\sqrt{6}\rho^3 \cos3\theta$	Horizontal Trefoil
10	$\sqrt{10}\rho^4 \sin4\theta$	Oblique quatrefoil
11	$\sqrt{10}(4\rho^4 - 3\rho^2)\sin2\theta$	Oblique Secondary Astigmatism
12	$\sqrt{5}(6\rho^4 - 6\rho^2 + 1)$	Spherical Aberration
13	$\sqrt{10}(4\rho^4 - 3\rho^2)\cos2\theta$	Horizontal Secondary Astigmatism
14	$\sqrt{10}\rho^4 \cos4\theta$	Horizontal Quatrefoil
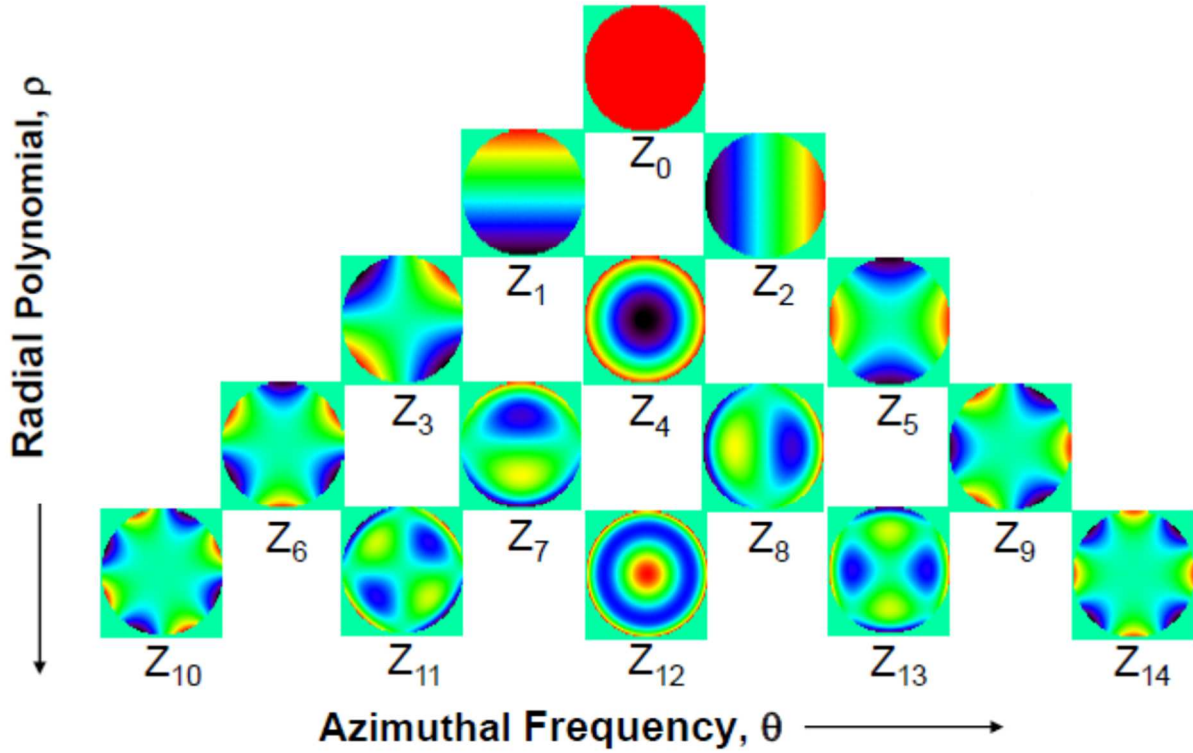
Figure 4.7) Zernike Polynomial Pyramid

The polynomials are fitted to the reverse-raytraced wavefront such that

$$A\vec{x} = \vec{b}$$

<div align="right">(4.3.1)</div>

$$where\ A = \begin{bmatrix} z_0(\rho_1, \theta_1) & z_1(\rho_1, \theta_1) & \cdots & z_{14}(\rho_1, \theta_1) \\ z_0(\rho_2, \theta_2) & z_1(\rho_2, \theta_2) & \cdots & z_{14}(\rho_2, \theta_2) \\ \vdots & \vdots & & \vdots \\ z_0(\rho_{14}, \theta_{14}) & z_1(\rho_{14}, \theta_{14}) & \cdots & z_{14}(\rho_{14}, \theta_{14}) \end{bmatrix}$$

$\vec{b}$ is a vector that contains all of the reverse-raytraced wavefront data points and $\vec{x}$ is the coefficient (or weight) of the Zernike polynomials. Since $\vec{b}$ is typically much longer than 14 elements, the matrix **A** and vector $\vec{x}$ is stacked so that the matrix dimensions satisfy equation (4.3.1). To determine the values of $\vec{x}$, least square fitting is applied as shown in equation (4.3.2) where (T) represents the transpose of the matrix.

$$\vec{x} = [A^T A]^{-1} A^T \vec{b}$$

Once the coefficients of the Zernike's are determined, the Zernike fitted surface can be subtracted from the actual measured (and reverse-raytraced) surface to generate a map of high frequency error from the base radius. Figure 4.8 shows the final profile generated for a confocal surface measurement. To clarify, this surface has been unwrapped, stitched, reverse-raytraced, and had the first 15 Zernike terms removed.
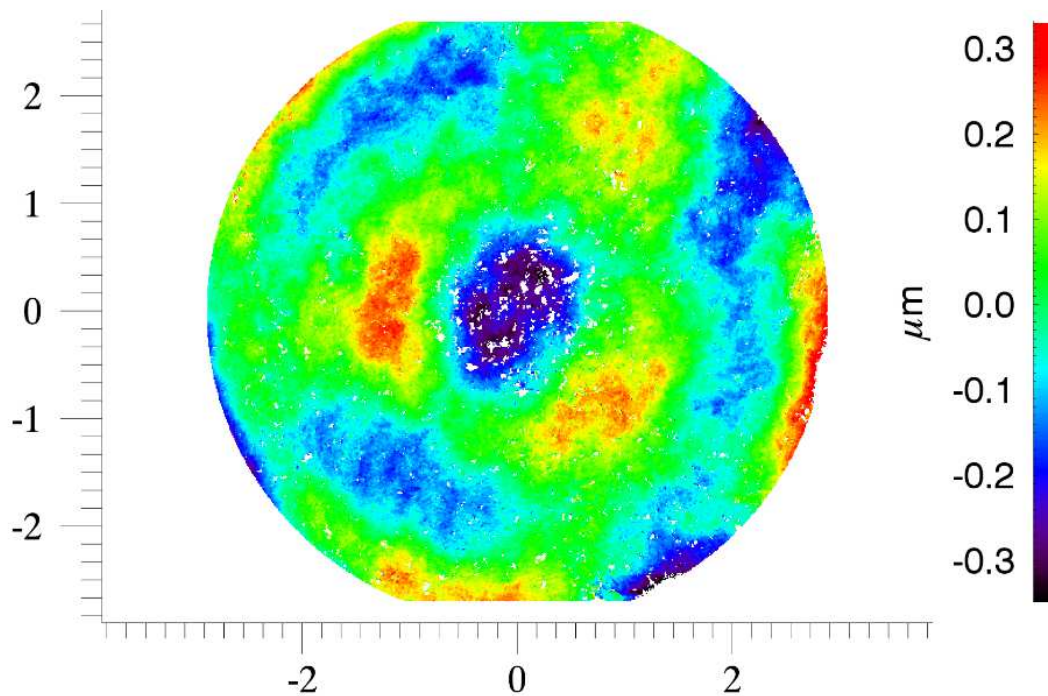
Figure 4.8) Reverse-Raytraced wavefront with the first 15 Zernike's removed

4.4   Processing order

The order in which the surfaces are analyzed is important to generating accurate profiles. To be precise, the cat's eye measurement for the posterior surface, the surface that rest on the eye, and the cat's eye measurement for the anterior surface must be loaded first. Afterwards, the posterior surface confocal profile must be unwrapped, stitched, and reverse-raytraced before beginning the analysis of the anterior surface. The results of the posterior surface are then taken into account in the reverse

raytracing algorithm for the anterior surface. The cat's eye measurement must be done first to determine the base radii of the surfaces. Once both surface profiles are generated, a thickness profile can be determined using the surface data and the axial difference measured by the DMI between the surfaces.

5   INITIAL SYSTEM RESULTS

The performance of the system was previously reported in (Heideman, 2014); however, the first part of this upgrade was to reevaluate the system with several different contact lenses. This section will display the results of several measurements and discuss the problems encountered using the theory discussed from section 2 through 4. Starting with commercially available lenses, curious features will be shown and analyzed followed by an evaluation of more advanced surfaces with known errors. Afterwards, the repeatability of the system will be presented and the limitations discussed.

5.1   Commercial Lenses

5.1.1   Etafilcon-A (8 Diopters)

Figure 5.1, Figure 5.2, and Figure 5.3 show the two measured surface profiles and thickness measurement for an Etafilcon-A lens. The lens has a spherical power of 8 diopters and a reported base curvature of 8.3 mm. Each figure shows the profile having the first 3 Zernikes removed to see the deviation from a sphere, followed by the first 15 Zernikes removed to see the high frequency variations.

One curious artifact of the images is the difference in area covered when looking at the profiles with and without the Zernikes. In Figure 5.1, the surface without 15 Zernikes removed shows a total area of about 12 mm (3 mm x 4 mm). When the 15 Zernikes are removed, the surface area changes to a circle rather than square. This is due to Zernikes only existing over a circle. The data outside the circle is cropped. Also note that the anterior surface does not cover the same area as the posterior surface. This

45

is due to a magnification change in the imaging since the second surface is further away from the detector. Even if it is moved towards the detector and placed in the same plane as the first surface, the rays refracted from the first surface alter the imaging system.
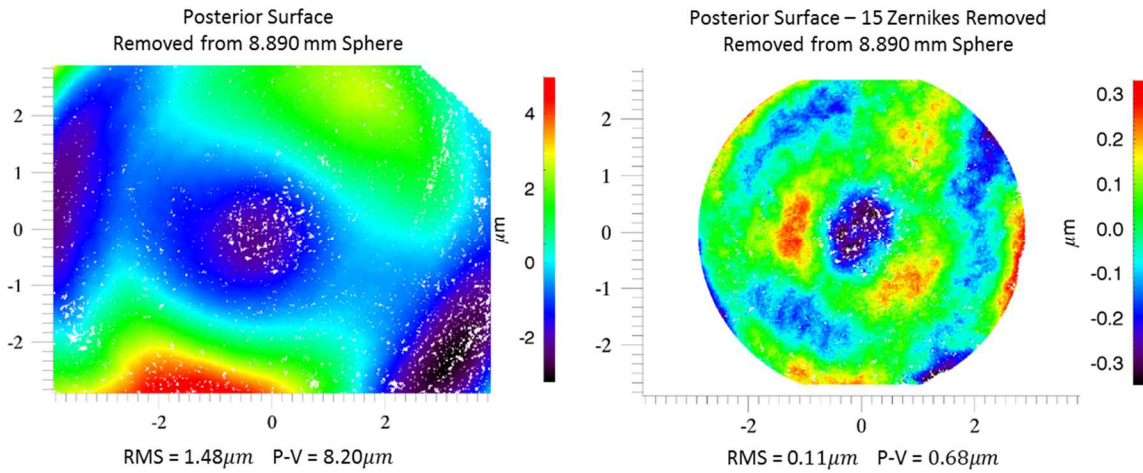
Figure 5.1) Posterior Surface of E2 Lens
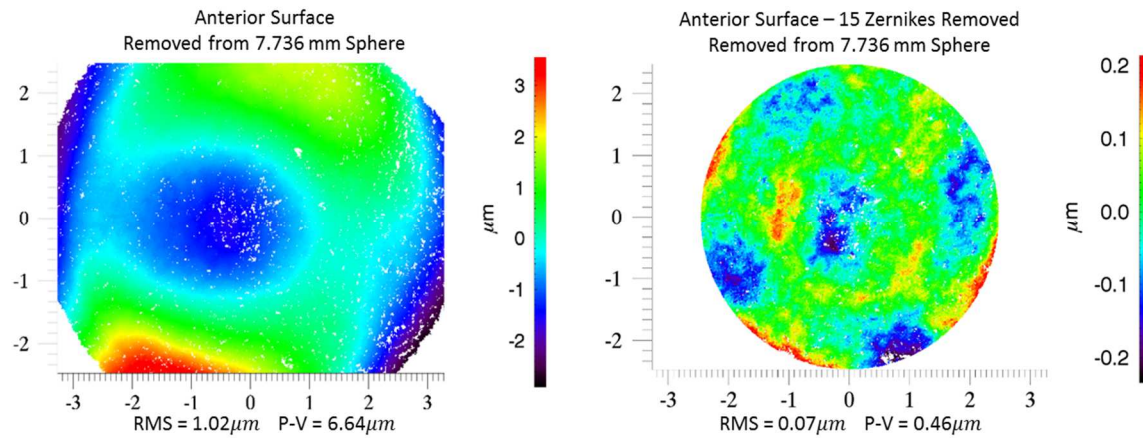
Figure 5.2) Anterior Surface of E2 Lens
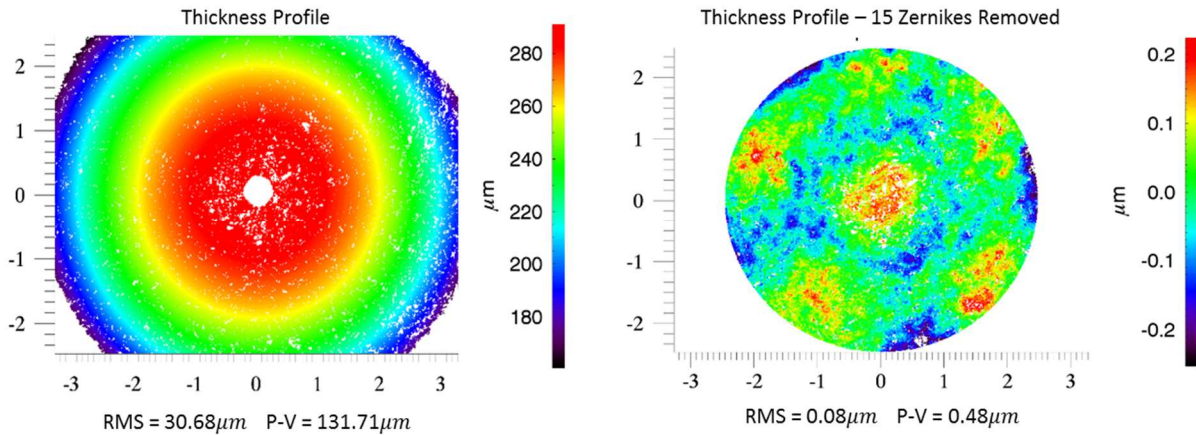
Figure 5.3) Thickness Profile of E2 Lens

As it should be expected, the two surface profiles are generally the same with a small difference between their peak to valley and RMS values. They show the same general contours in the same regions and have similar high frequency structures.

The thickness profile without having 15 Zernikes removed is curious and shows the general shape of the lens. It is not very useful for seeing how uniform the thickness is across the lens as much as the 15 Zernike removed profile; however, it is clear that the lens has positive power as it follows the standard thickness profile expected of a positive lens. It is thicker in the center and thins out radially. It should be noted that the white spot in the center of the thickness profile is beyond the z-range of the plot and is cutoff. The plot height is not simply scaled to see smaller features but rather a percentile threshold is applied. This percentile threshold crops the profile in all three dimensions rather than just pixels with a certain height value, and this is something that will need to be addressed in the software. The data is existent in these blank regions, so the profile can be deceptive by hiding the data.

To compare results, another Etafilcon-A lens of the same power and curvature was tested and the results are shown below in Figure 5.4, Figure 5.5, and Figure 5.6. To distinguish the lenses, this data set was assigned the tag number of E3 whereas the previous was tagged E2.

Although the surface profiles of the E3 lens are not as pronounced as they were in the E2 profiles, they are still very similar looking. This is more obvious when viewing the high frequency errors. The RMS and peak to valley values are pretty close to one another; however, the thickness profile appears more uniform though its peak to value is over two times higher.

To give an idea of numbers, the RMS measurements for the two lenses on the average agree to within 8.91 % with a standard deviation of 6.34% while the peak to valley measurements agree on the average to within 20.24 % with a standard deviation of 22.65%. The radius measurements agree to within 0.43 % with a standard deviation of 0.19%.
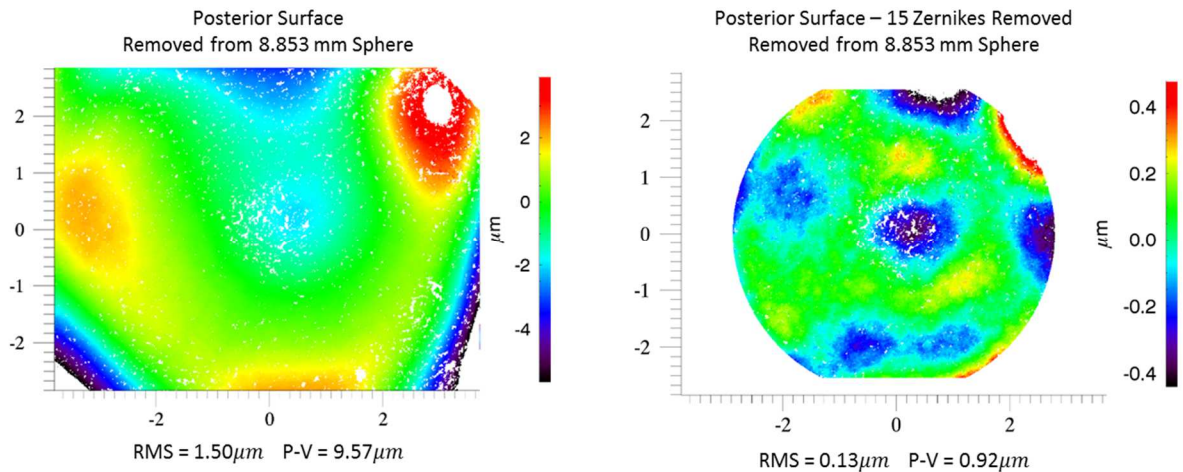
Figure 5.4) Posterior Surface of E3 Lens
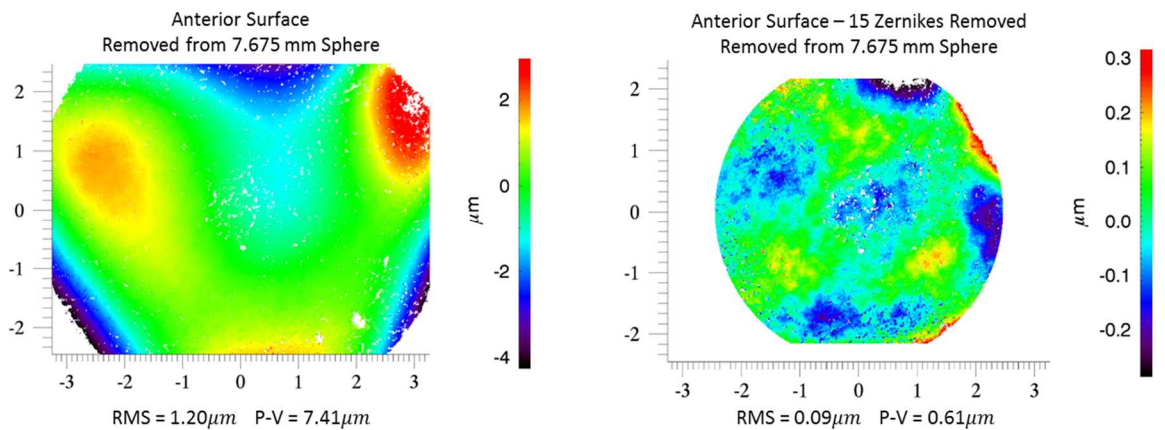
Figure 5.5) Anterior Surface of E3 Lens
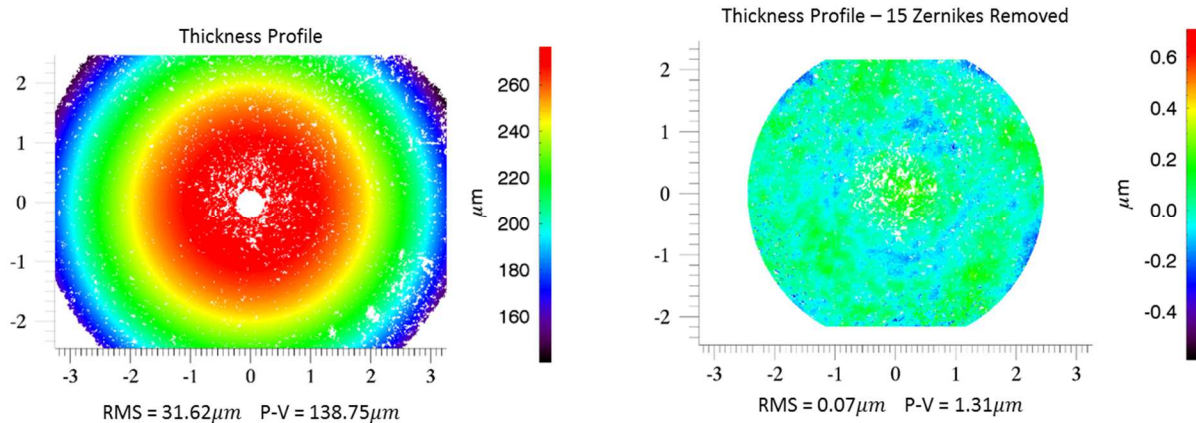
Figure 5.6) Thickness Profile of E3 Lens

5.1.2   Etafilcon-A (-3.5 Diopters)

To ensure that the software is not outputting similar profiles due to algorithm errors, a third lens

was tested of the same type as the previous two but with a different power and curvature. This lens had

a base curvature of 8.7mm and a power of -3.5 diopters. Due to the order of data processed, this lens

was tagged as E1.
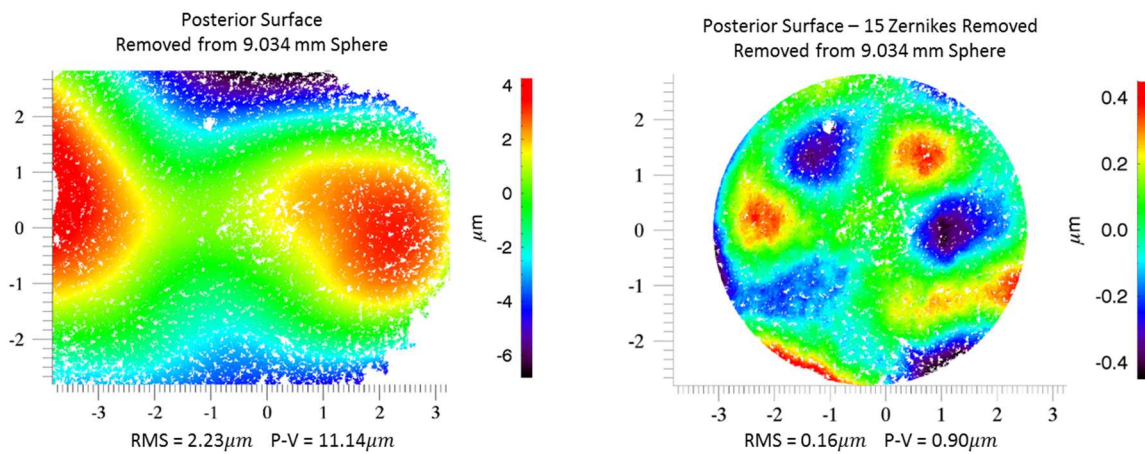
Figure 5.7) Posterior Surface of E1 Lens

49
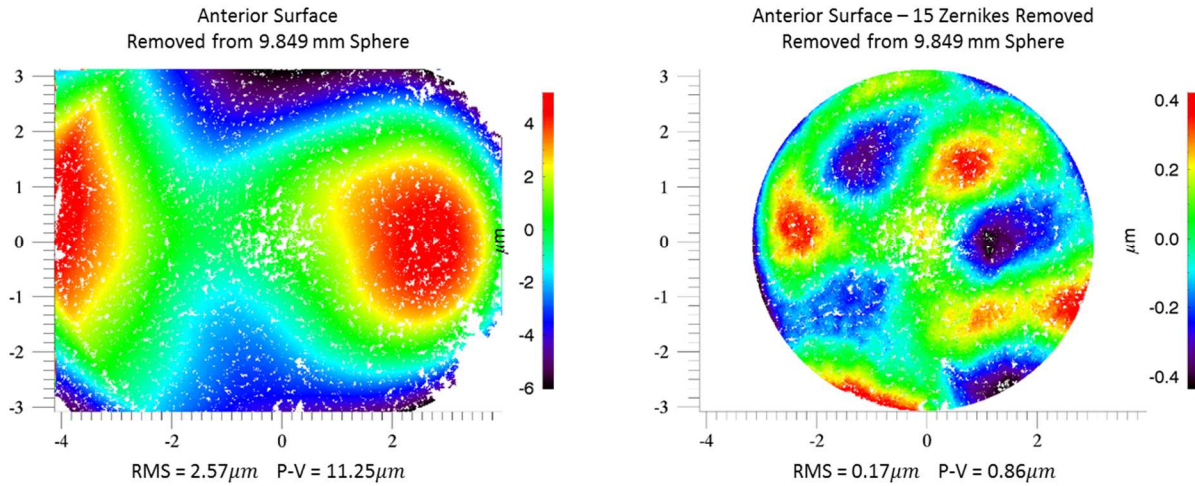
Figure 5.8) Anterior Surface of E1 Lens
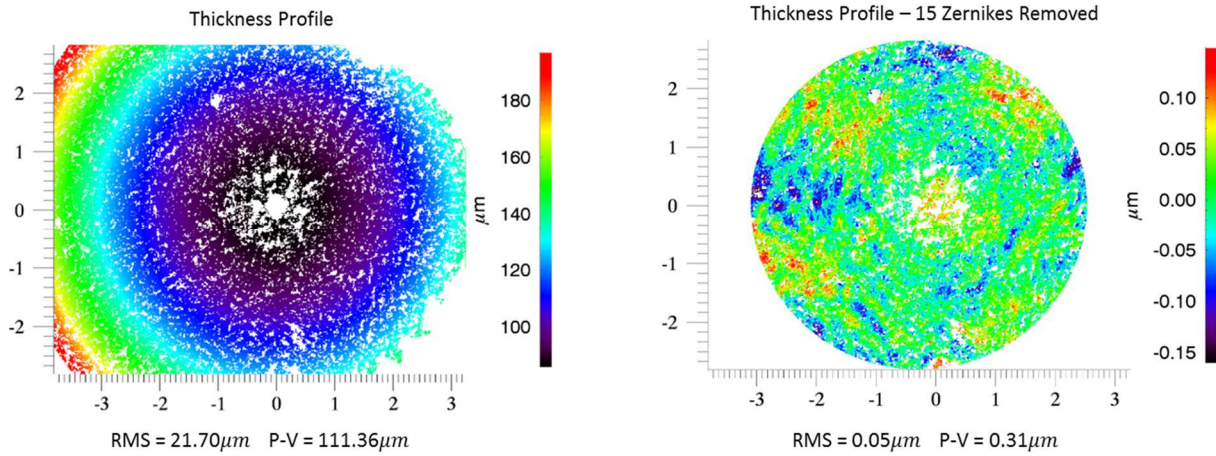
Figure 5.9) Thickness Profile of E1 Lens

As it can be seen, the images are grainier due to unwrapping errors induced either by noise, phase residues, or low visibility which causes lack of data. As expected, the surface profile of this lens is much different than the previous however, the peak to valley and RMS values are still on a similar scale as the previous 2 lenses. Also note that the thickness plot agrees with the general shape of a negative lens; thinner in the center and thicker at the edges.

5.1.3 Etafilcon-A Toric (-1 Diopters, -1.25 Diopters)

Figure 5.10, Figure 5.11, and Figure 5.12 show the measured profiles for a Toric Lens. The lens has spherical power of -1 Diopters, and a cylindrical power of -1.25 diopters. The base curvature of the lens in 8.7 mm.

It should be noted that the posterior surface measurement had a significant difference in edge height as compared to the center due to noise in the system or unwrapping errors. This would alter the display results, so the edge of the lens was removed from the analysis screen to allow for a better understanding of the profile shape near the center. This is why the 15 Zernike removed posterior profile is truncated along the y-axis of the plot.
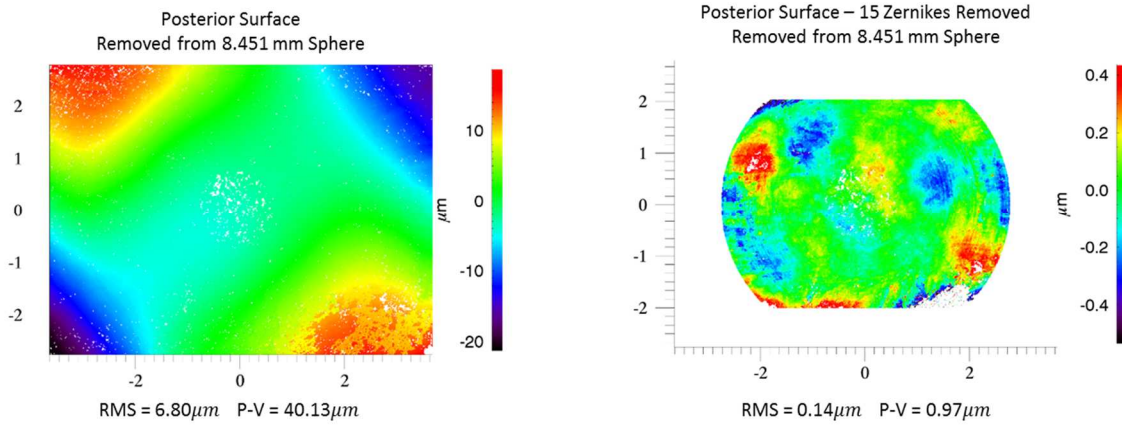
Figure 5.10) Posterior Surface of Toric Lens
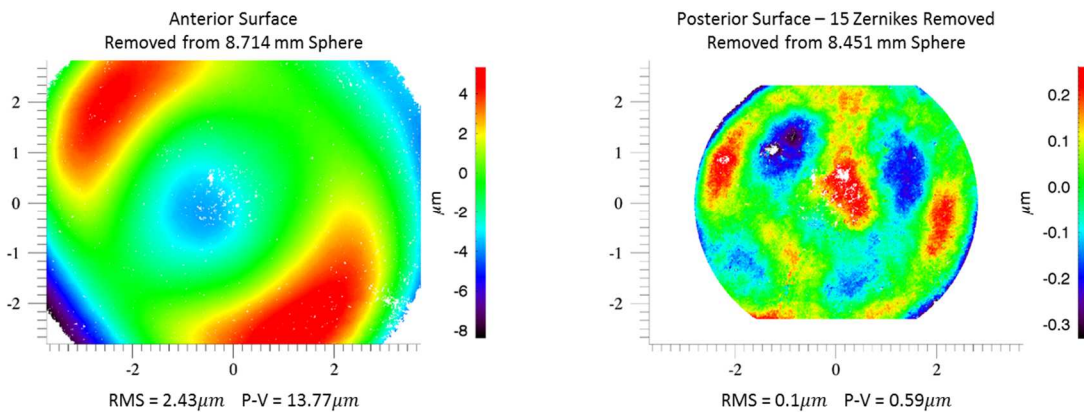
Figure 5.11) Anterior Surface of Toric Lens

51
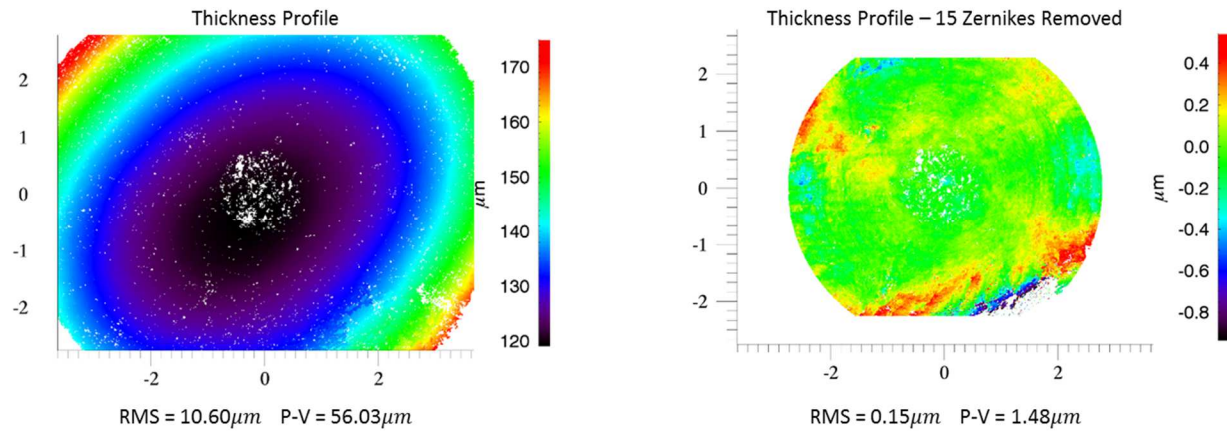
Figure 5.12) Thickness Profile of Toric Lens

Again, the high frequency surface errors are on a similar scale to the non-Toric lenses which demonstrates the precision of the machine to measure standard errors in the manufacturing of the contact lens. The surface profiles have much larger RMS and peak to valley errors but this is to be expected of a toric lens due to the nature of the shape.

5.2   Deformed Lenses

Several other lenses with known errors, either induced or previously measured, were also tested. Most lenses were folded or creased and the goal was to see how much of the surface profile could be measured with these lenses. The lenses were classified as either being distorted or wrinkled, and only their powers were provided.

5.2.1   Distorted lenses

Two sets of distorted lenses are presented in this report. The surface and thickness profiles are shown from Figure 5.13 through Figure 5.18 with the first set being from the lens tagged 07 and the other being tagged as 09. Both lenses are Toric with the same prescription; however, they demonstrate different surface profiles. The lenses have a spherical power of -1.5 diopters and a cylindrical power of -0.75 diopters.

Posterior Surface
Removed from 8.758 mm Sphere

RMS = 1.68μm P-V = 9.33μm

Posterior Surface – 15 Zernikes Removed
Removed from 8.758 mm Sphere

RMS = 0.80μm P-V = 4.19μm
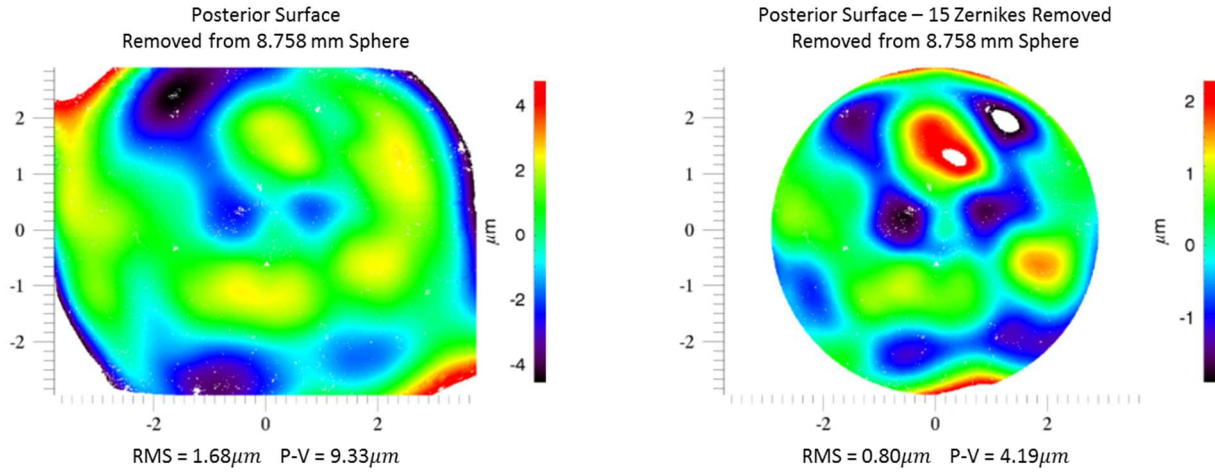
Figure 5.13) Posterior Surface of Distorted Lens -07

Anterior Surface
Removed from 9.118 mm Sphere

RMS = 3.13μm P-V = 15.03μm

Anterior Surface – 15 Zernikes Removed
Removed from 9.118 mm Sphere

RMS = 0.81μm P-V = 5.05μm
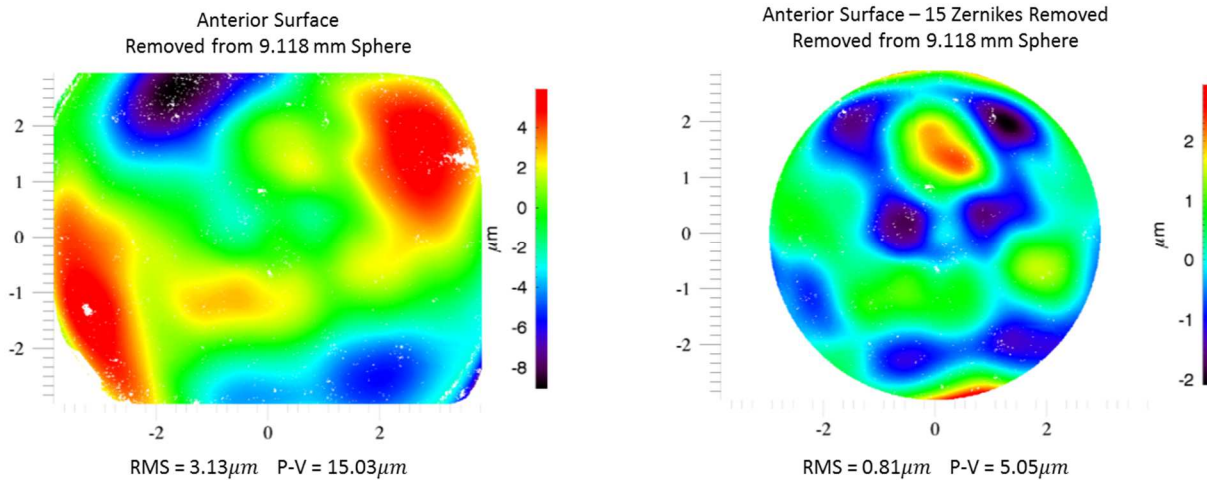
Figure 5.14) Anterior Surface of Distorted Lens -07

Thickness Profile

RMS = 12.33μm P-V = 65.33μm

Thickness Profile – 15 Zernikes Removed

RMS = 0.06μm P-V = 0.39μm
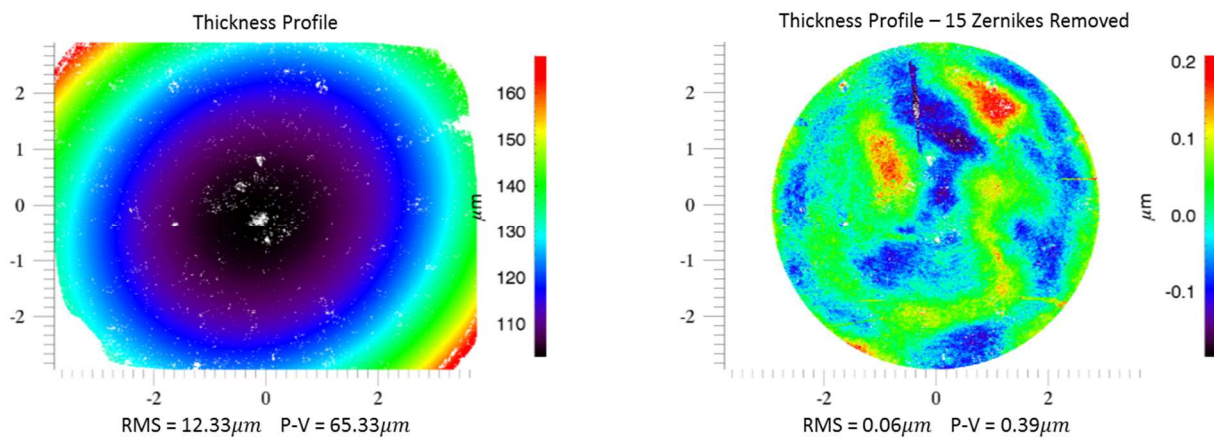
Figure 5.15) Thickness Profile of Distorted Lens – 07

53

Posterior Surface
Removed from 8.857 mm Sphere

RMS = 3.25μm P-V = 22.26μm

Posterior Surface – 15 Zernikes Removed
Removed from 8.857 mm Sphere

RMS = 0.69μm P-V = 3.30μm
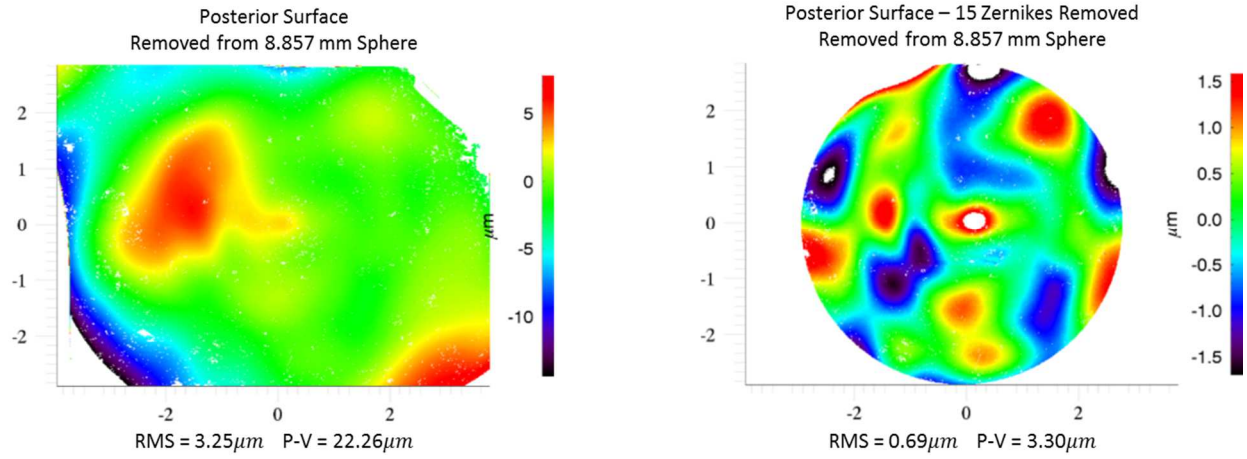
Figure 5.16) Posterior Surface of Distorted Lens -09

Anterior Surface
Removed from 9.289 mm Sphere

RMS = 2.74μm P-V = 12.94μm

Anterior Surface – 15 Zernikes Removed
Removed from 9.289 mm Sphere

RMS = 0.68μm P-V = 3.41μm
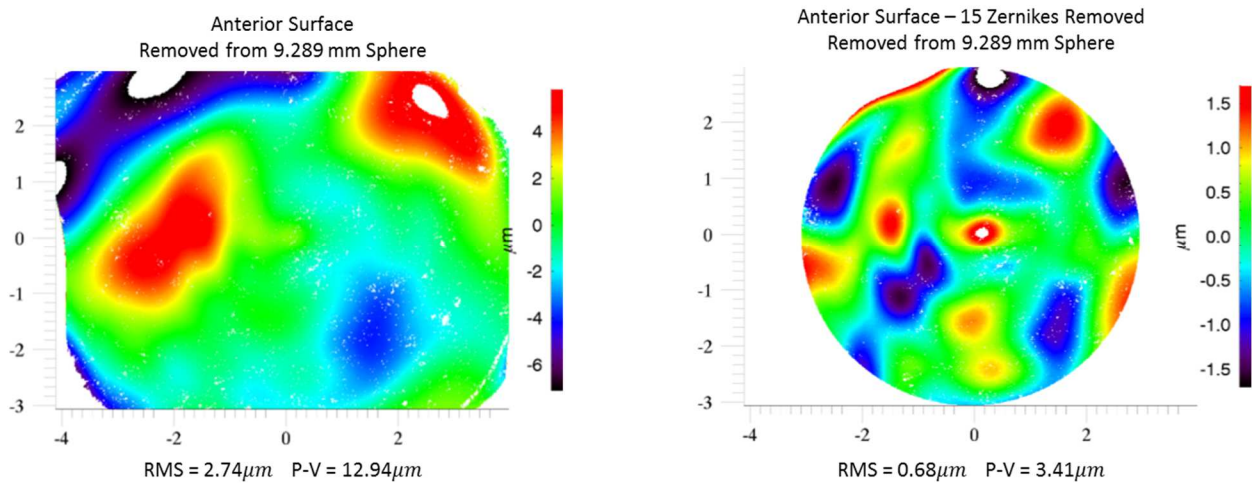
Figure 5.17) Anterior Surface of Distorted Lens -09

Thickness Profile

RMS = 13.94μm P-V = 71.69μm

Thickness Profile – 15 Zernikes Removed

RMS = 0.09μm P-V = 0.53μm
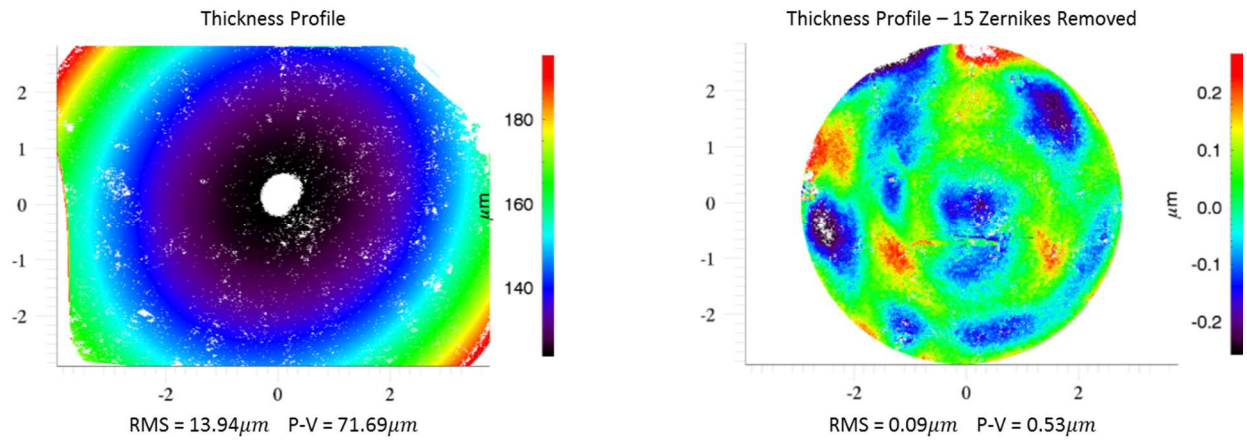
Figure 5.18) Thickness Profile of Distorted Lens – 09

As the results show, the distortions on the lenses profiles are easily seen, but what is interesting is that they give generally the same P-V measurement errors as the previously shown commercial lenses. With these measurements, it was found that the average peak to valley measurement agree to within about 23.45% with a standard deviation of 18.44%. Recall that for the first two commercial lenses shown, the peak to valley average error was 20.29% with a standard deviation of 22.65%.

The RMS and radial errors are higher than before, but this is to be expected if the surfaces are highly distorted. These small surface distortions should not affect the peak to valley values as much as they should effect the RMS values. The average RMS value was reported to be within 19.03% with a standard deviation of 14.7%. The radius measurement error is only slightly higher than the commercial lenses with an average error of 1.05% and a standard deviation of 0.37%. Overall, this indicates that the interferometer is capable of producing repeatable results even with large surface errors.

5.2.2 Wrinkled Lenses

The wrinkled lenses shown in Figure 5.19 through Figure 5.24 are from two separate manufacturing lots but were purposely creased to see how the interferometer would handle very high slope changes in the measured region. This slope change would induce very high fringe frequency and even possibly lack fringe frequency as the high variation left the coherence window.

The first lens, tagged 06, is toric with a spherical power of -1.5 diopters and a cylindrical power of -0.75 diopters like the previous distorted lenses. The second lens, tagged 19, only has a spherical power of -1.75 diopters with a known base curvature of 8.4 mm.

55

Posterior Surface
Removed from 8.674 mm Sphere

RMS = 5.80μm P-V = 23.12μm

Posterior Surface – 15 Zernikes Removed
Removed from 8.674 mm Sphere

RMS = 3.13μm P-V = 13.34μm
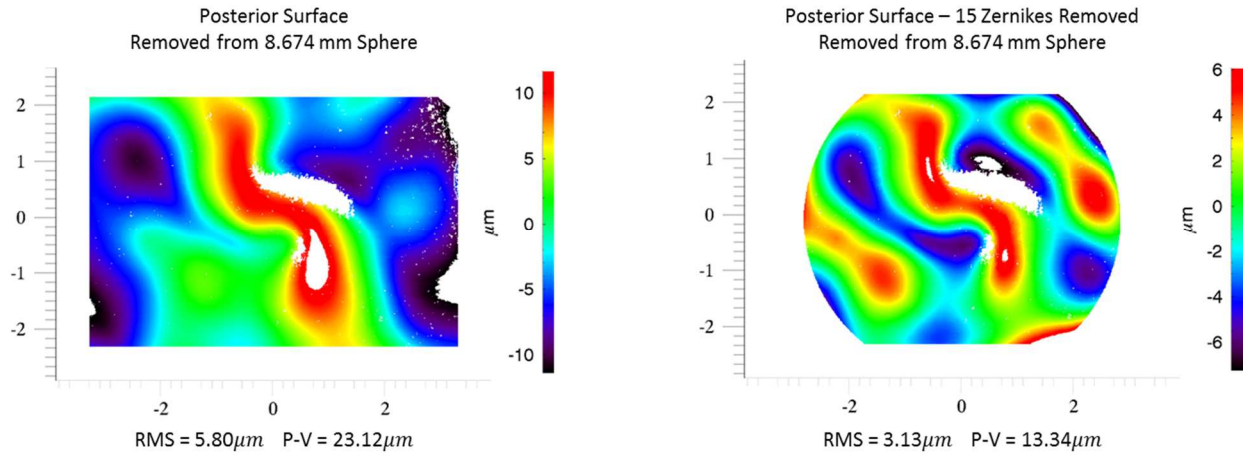
Figure 5.19) Posterior Surface of Wrinkled Lens -06

Anterior Surface
Removed from 9.470 mm Sphere

RMS = 5.69μm P-V = 34.97μm

Anterior Surface – 15 Zernikes Removed
Removed from 9.470 mm Sphere

RMS = 3.02μm P-V = 16.98μm
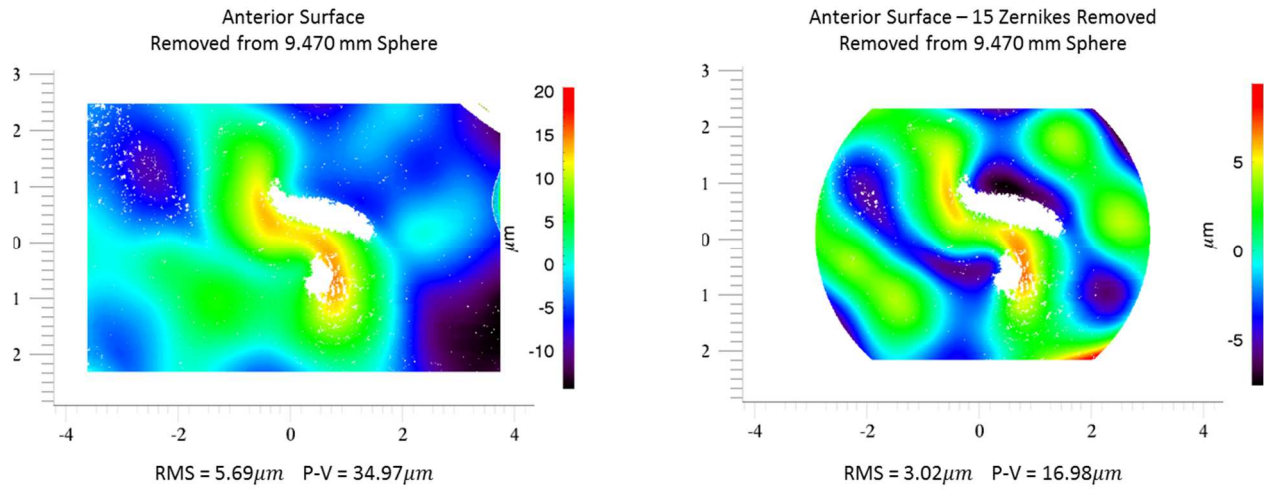
Figure 5.20) Anterior Surface of Wrinkled Lens -06

Thickness Profile

RMS = 20.66μm P-V = 112.61μm

Thickness Profile – 15 Zernikes Removed

RMS = 0.29μm P-V = 4.25μm
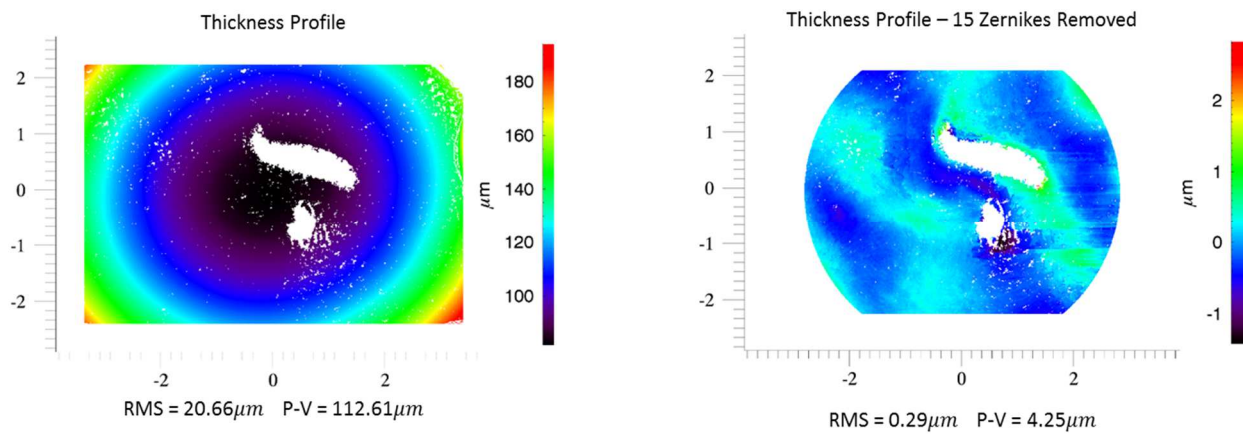
Figure 5.21) Thickness Profile of Wrinkled Lens -06

56

Posterior Surface
Removed from 8.662 mm Sphere

RMS = 6.13μm P-V = 28.28μm

Posterior Surface – 15 Zernikes Removed
Removed from 8.662 mm Sphere

RMS = 3.47μm P-V = 18.57μm
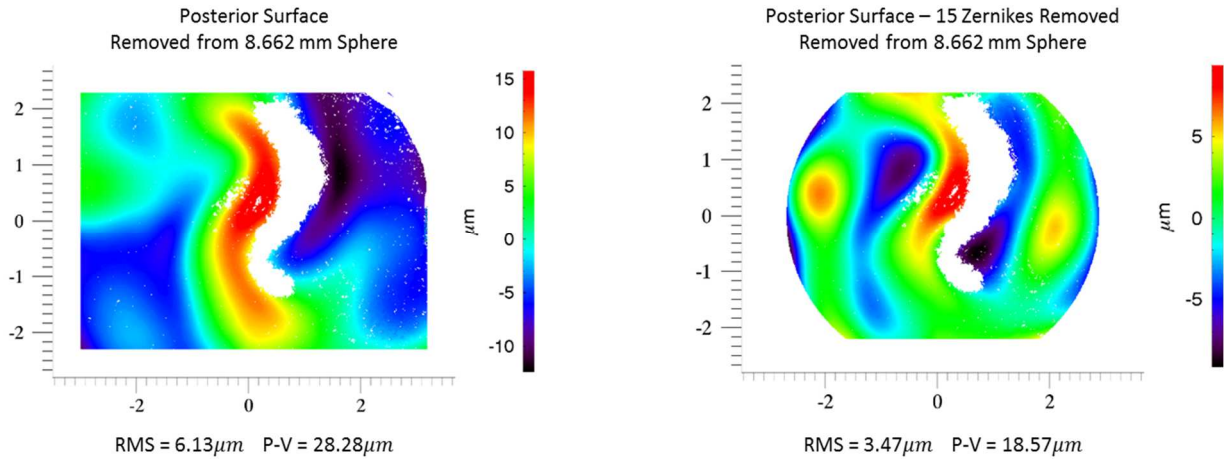
Figure 5.22) Posterior Surface of Wrinkled Lens -19

Anterior Surface
Removed from 9.069 mm Sphere

RMS = 5.56μm P-V = 27.14μm

Anterior Surface – 15 Zernikes Removed
Removed from 9.069 mm Sphere

RMS = 3.45μm P-V = 19.17μm
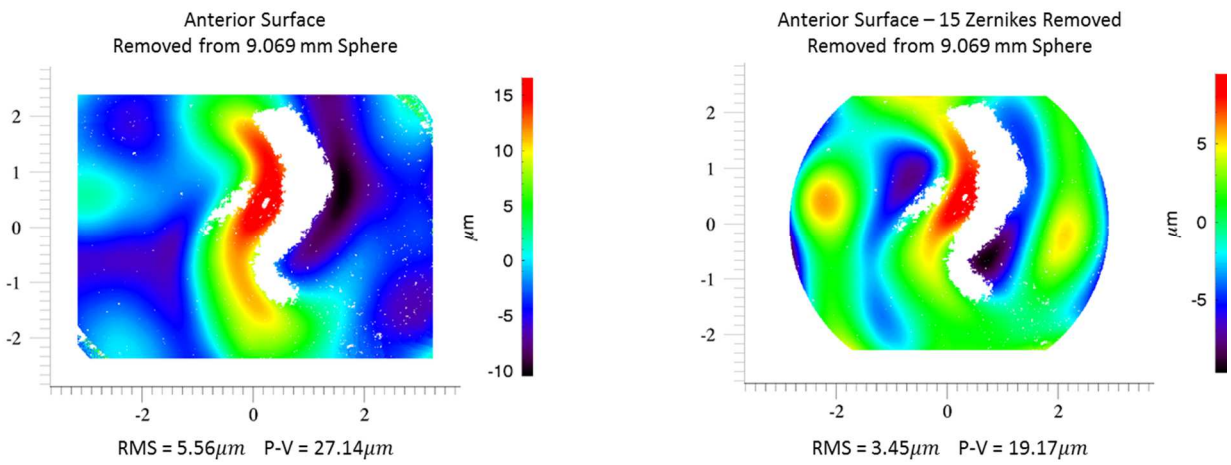
Figure 5.23) Anterior Surface of Wrinkled Lens -19

Thickness Profile

RMS = 9.36μm P-V = 53.65μm

Thickness Profile – 15 Zernikes Removed

RMS 0.19μm P-V = 3.31μm
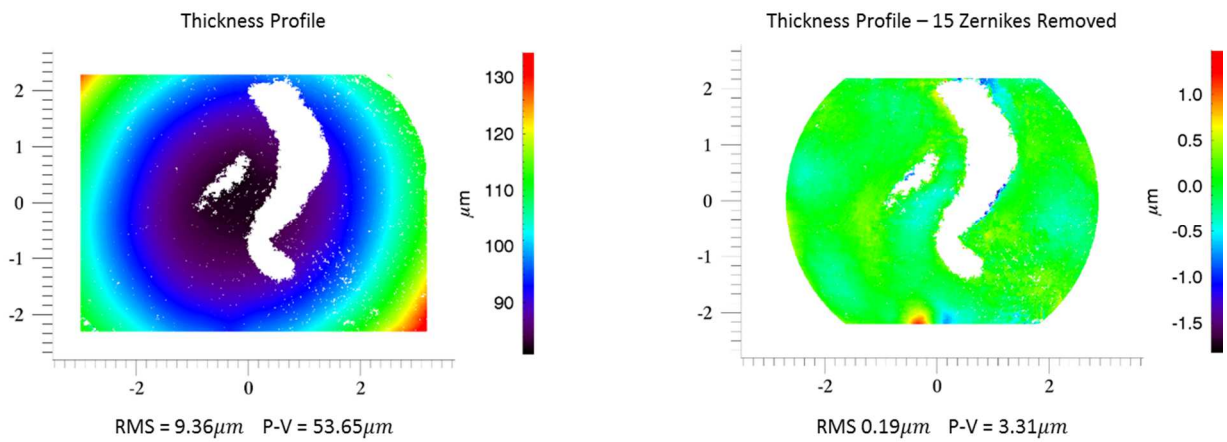
Figure 5.24) Thickness Profile of Wrinkled Lens -19

As shown, the interferometer could overcome the lack of data and still stitch the surface around the crease; however, it should be noted that the interferometer can only overcome the crease if there is an overlap between the fringe sets. Even though only two lenses are shown, seven creased lenses were tested in total. Only five were able to be reconstructed as the other two had no overlapping fringe data when the lens was analyzed in segments.

Also interesting from the results is that though the two contact lenses are of different types, one spherical and one toric, the surface profiles no longer have the same characteristics as the non-wrinkled lenses for those types. Both lenses show significant distortions which should be expected; however, the thickness profiles do still appear to be similar to the previous lenses, with the obvious lack of data. The average RMS value is on the order of 15 microns which is similar to the average RMS value of the previously shown thickness profiles. Note that this is for the profile without Zernikes removed.

5.3   Initial Repeatability

To ensure that the features seen in the previous surface profiles were indeed from the contact lens surfaces and not random, a repeatability test was done on several lenses. Though previous numbers were shown to demonstrate how well the measurements agree with one another, they cannot be used as a measure for repeatability since the lenses were always different.

The surface profiles shown in Figure 5.25 and Figure 5.26 are from three separate measurements of the distorted toric lens tagged 07. The first measurement was taken a month before the second two. For the second measurement, the contact lens was rotated 90 degrees in the system to see if the features would rotate, and the third measurement was returned to the original testing position to see if it would agree with the original as well.

As expected, the features were repeated and also rotated for the rotated measurement. For the posterior surface, the average RMS value was 743 nm with a standard deviation of 51 nm. The peak to valley mean was 3.98 microns with a standard deviation of 265 nm.

For the anterior surface measurement, the RMS difference mean was 740 nm with a standard deviation of 60.8 nm. The peak to valley mean was 4.37 microns with a standard deviation of 603 nm. Thus, the system could perform a repeatable measurement to within 56 nm RMS ($\approx \lambda/12$) and 435 nm peak to valley. The radius value had an error of about 57 microns which is about 0.6% considering a 9mm radius.
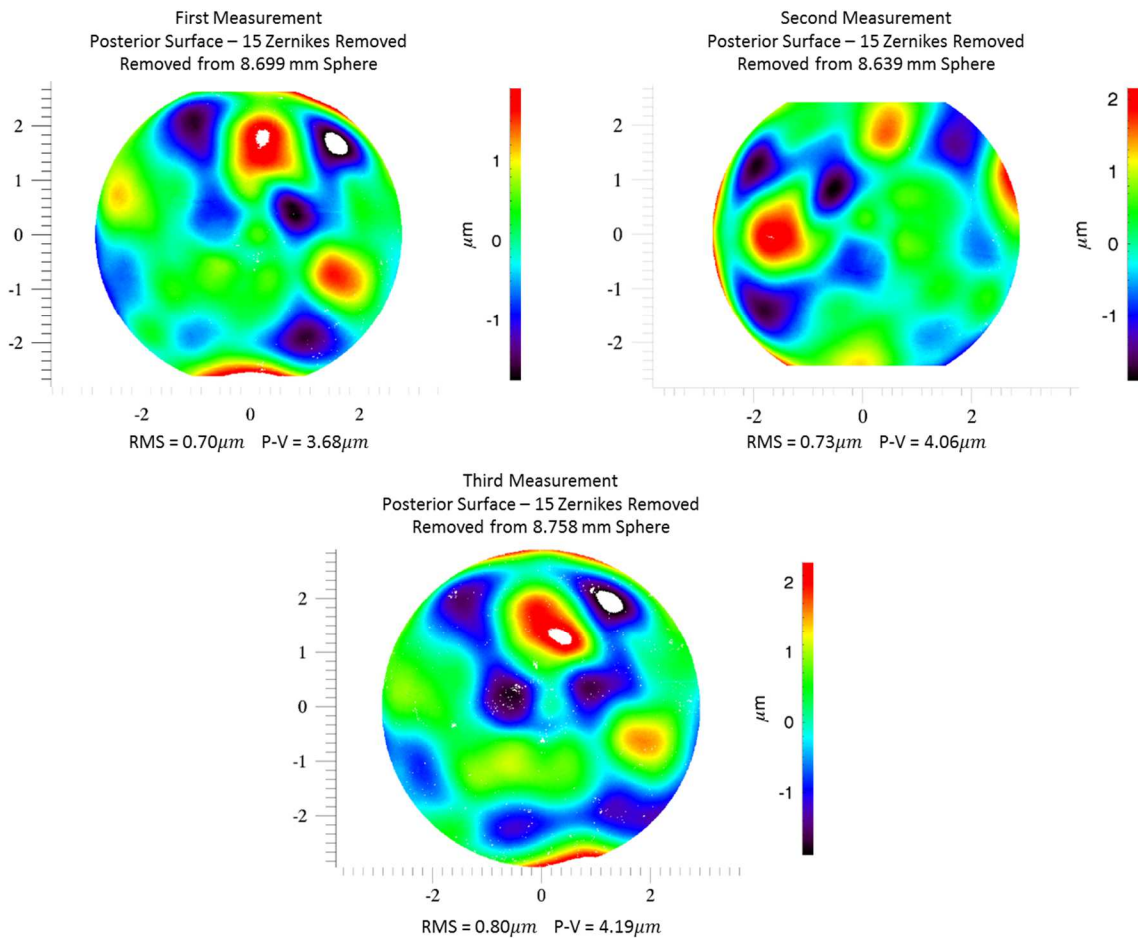
Figure 5.25) Posterior Surface Initial Repeatability Measurement
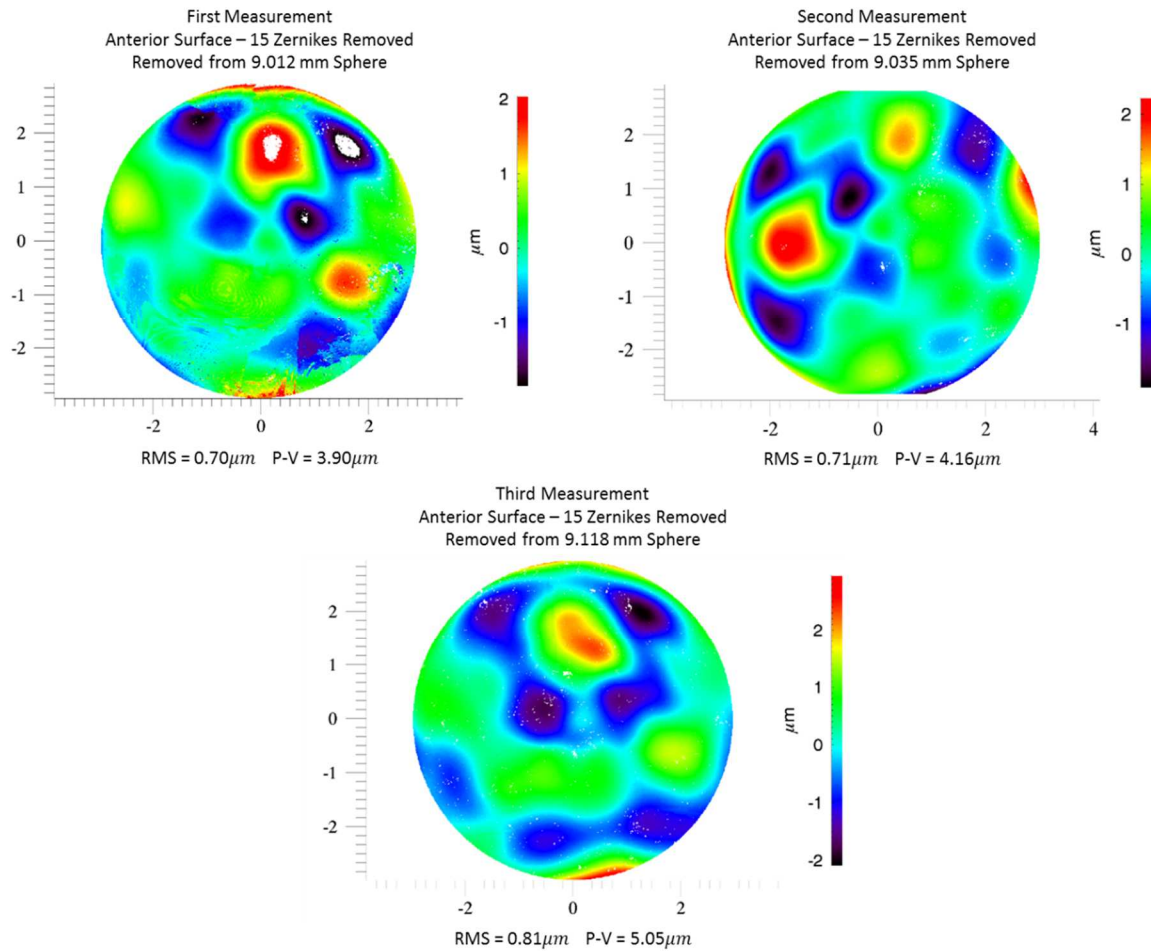
Figure 5.26) Anterior Surface Initial Repeatability Measurement

5.4 Base Curvature "Measurement"

In all of the measurements with known base curvature, it was seen that the reference sphere subtracted from the posterior surface profiles would be about 10% off from the prescribed base curvature. It should be clarified that the base curvature on a contact lens is the overall sag from the center of the lens relative to the entire 14mm diameter of the posterior surface. Since the interferometer only scans an area about 8mm in diameter, this best fit sphere is actually of a different sag value than the prescribed base curvature.

While the drawings of the contact lenses are confidential, looking at a select amount of the drawings and comparing with the results measured show that the base curvature is typically within 1% of the expected sag over the scanned area.

5.5   Limitations

This section will summarize some of the limitations briefly mentioned in sections 5.1 through 5.3 as well as discuss other limitations discovered in the initial use of the system.

5.5.1   Software Limitations

Starting with what was previously mentioned, it was found that the phase unwrapping algorithm struggles to overcome patches of noise or low visibility and tends to fall apart around the edges of the captured profile. As mentioned earlier, the unwrapping method utilizes a quality threshold raster scanning method which looks for the highest visibility point to start the unwrapping algorithm. This is efficient; however, it is not always the best method for some profiles. It seems necessary to develop a more robust unwrapping algorithm that can handle noise and low visibility better. Several measurements that were taken could not be unwrapped, even though the fringe modulation was clearly, but faintly, visible.

Also, in order to see some of the features away from the edges, the analysis algorithm would have to crop pixels; however it crops information in all three dimensions; therefore, viewing a reduced area profile eliminates surface height errors from the map. Often, these errors were substantial and at the edges, so cropping those edges still provided enough information over the desired area. However, as shown in the thickness profiles, data could be lost in the middle if it contained high points. This was seen in a few profiles not discussed above.

As mentioned in section 5.2.2, the stitching algorithm is unable to stitch a profile together if there are no overlapping regions. Ideally a profile should be generated, even with holes, if the data was captured since the area over the detector is known and each pixel can be mapped back to the surface.

5.5.2 Mechanical limitations

As mentioned in section 3.2, the contact lens sits on a glass plate with a hole in the middle to allow the light to only scan the contact lens. This setup has several setbacks but was not the focus of the initial build. First, the glass plate is actually a microscope slide and the hole was drilled using a grinding tool. The slides are mass produced out of thin glass and typically and are not ideally flat. The drilling with the grinding tool further distorts the flat surface, and this can translate back to the surface profiles of the contact lens. Since the contact lens is soft, the contact lens will distort under its own weight if the weight is not properly distributed. By having a non-flat surface support the rim of the contact lens, the contact lens will rest across a few points on the rim rather than the entire rim edge. This will provide a non-uniform weight distribution across the contact lens which will distort the actual surface. Luckily, this glass distortion is very minor; however, the contact lens weight distribution problem is a little more severe, due to the actual manufacturing of the contact lens.

The edge of the contact lens is the only feature that has a very loose tolerance. Basically, the lens is manufactured to meet strict requirements in the center but there is no requirement at the edge. This eliminates the ideal ring support for the contact lens in this mounting scheme. Instead, the contact lens will rest on three or more points and buckles under the stress of its own weight when supported in this fashion.

Also, by mounting the contact lens concave down as it is, there is no actual restriction of the lateral position of the contact lens. It was seen that if the positioning of the contact lens along the

optical axis was adjusted too fast, the contact lens would start to translate orthogonal to the beam path due to vibration from the linear stages. This would nullify the cat's eye measurement, and this obviously made repeatability more challenging as well.

Another limitation to the current mounting scheme is the placement of the test arm quarter wave plate. It is required to go in between the test surface and the diverger lens; however, resting directly on the last surface of the diverger lens assembly has caused lots of scattered light problems which reduce visibility. Since the wave plate has to be rotated to find the optimal return signal, it directly scratches the last surface of the diverger lens as it rotates. The scratches are typically minor since the both the last surface of the diverger lens and the waveplate are submerged in saline; however, if the tank is left alone for a few days, the water evaporates and the salt in the saline forms crystals which do not always dissolve. These crystals tend to form at edges of the tank and in between the waveplate and the lens surface. Thus if the waveplate is rotated again, the crystal now grinds against the lens surface which causes deeper scratches.

Obviously having contaminates in the optical path will reduce visibility by scattering light, and the same is true with the saline crystals; however, the crystals are usually easy to clean out and have not been a major scatter source for serious measurements. One major scatter source for the interferometer however is the interface of saline to air after the contact lens. Originally, a plastic screw was used as a baffle above the contact lens, but is not ideal. The screw still gives too much specular reflection back into the arm which lower the signal seen from the contact lens. This thesis aims to address both the software and hardware issues of the initial build of LOCOH.

6   Mechanical Design Improvement

Understanding the limitations discussed in section 5.5.2 led to many changes in the layout of

LOCOH with most focusing on the test arm. The primary concern was the mounting of the contact lens

and providing it with an adequate ring support. It was thought that the best solution would be to invert

the interferometer such that the contact lens sat concave up rather than concave down. This would

ideally have the contact lens settle in a more repeatable state with the aid of gravity. Figure 6.1 shows

the new layout of LOCOH (not to scale). Notice that the fold mirror in the input arm is now removed in

this design as the beam goes straight from the collimating lens to the beam splitter. This removes some

misalignment control; however, it is still easy enough to work with.
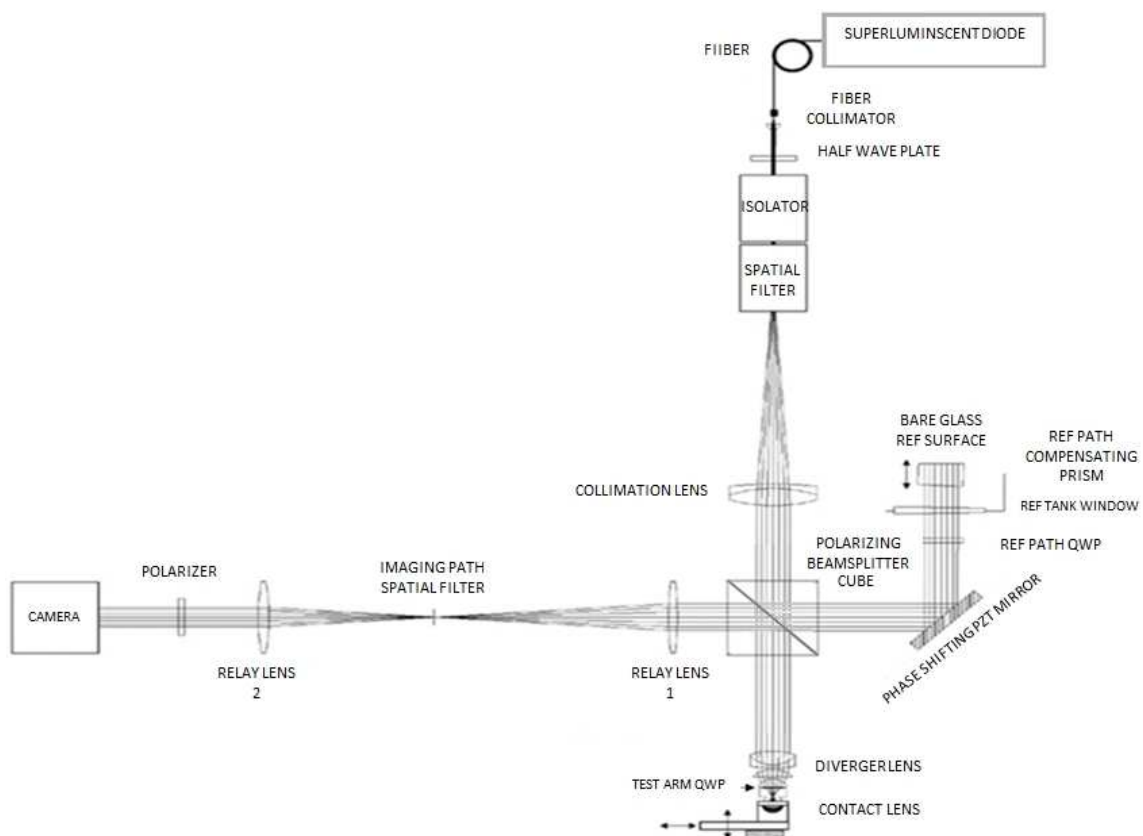
Figure 6.1) New layout concept of LOCOH

Implementing this concept however introduce new concerns such as air bubbles being trapped between the diverger lens and contact lens as well as having too much back scatter from the quarter wave plate. It was found from the previous configuration that as the test arm quarter waveplate scattered light which would lower visibility. This effect is small; however, as the waveplate got and closer and closer to the beam focus, the effect was more pronounced. Thus, it is ideal to have the waveplate as close to the last surface of the diverger lens to minimize this effect.

There was also a decision about choosing to move the contact lens vs. the diverger lens. If the contact lens mount within the tank was shifted along the optical axis, there could be a problem with the solution shifting the contact lens from the turbulence of the moving liquid. One idea was to move the diverger lens in place of the tank; however, this would void the reverse raytracing algorithm since the imaging system would change. Ideally, the entire interferometer would have to move relative to the contact lens, but this would require large motion control which would be costly and have a higher degree of difficulty for repeatability. Therefore, it was decided to again move only the contact lens during the measurements.

An initial 3D printed mount and tank was designed and used for testing the liquid turbulence. It was found that if there is proper ring support around the contact lens, the liquid would not displace the lens while the tank is motion; however, if the diameter of the ring support was less than 8 mm, the contact lens would shift under very sudden and fast movements.

6.1   Design Considerations

In regards to rebuilding the interferometer, it would be ideal to minimize the amount of components changed since the equipment had been used and the errors associated with using them were known. Because of this, some limitations were placed on the new components designed for the

test arm such as space and weight. For example, the Thorlabs (Newton, NJ) MTS50-Z8 linear stage has a specified maximum weight limit of 10 pounds with object's center of gravity being displaced about 0.5 inches from the base of the mount. Thus the torque limit is 5 in-lbs. With the beam height defined by the 3 inch PZT mirror due to limited mounting options, the optical axis would be defined 2 inches away from the stage forcing a weight limit of 2.5 pounds for the test arm tank with solution and contact lens mount combined.

It would also be ideal not to alter the amount of solution used during measurements. Thus, the test arm components would have to be designed such that both the confocal and cat's eye positions utilize the same amount of saline solution in the tank even though the path lengths are different. In the 3D printed prototype briefly mentioned earlier, there was no thorough consideration for the amount of solution needed. When switching from cat's eye to confocal or vice versa, solution would have to be added or removed which did alter the position of the contact lens if done fast enough due to liquid turbulence. It should be noted that this prototype testing was performed with an inadequate ring mount diameter making it more susceptible to fluid turbulence.

6.2   Diverger Lens Barrel and Barrel Protector

Due to the weight constraint placed on the tank, it would be desirable to reduce the amount of solution used; however, the amount needed would depend on the how much solution would be displaced when moving from cat's eye to the confocal measurement. A thorough analysis of the displacement was performed on the design and the results will be discussed in section 6.5, but it should be noted that the initial starting point was to redesign the diverger lens barrel such that it would minimally reduce liquid displacement.

The original lens barrel had a large flat face after the last surface of the diverger lens assembly that gave it a substantial surface area to interact with the solution. It was necessary since the barrel itself was the test arm tank previously, but in this new layout, that face was reduced in diameter and in height as well. The inside of the barrel remained the same as the previous design since there was no problems with its operations. Figure 6.2 shows the solid model drawings of the barrel. Note that the threads designed into the mount are not shown.
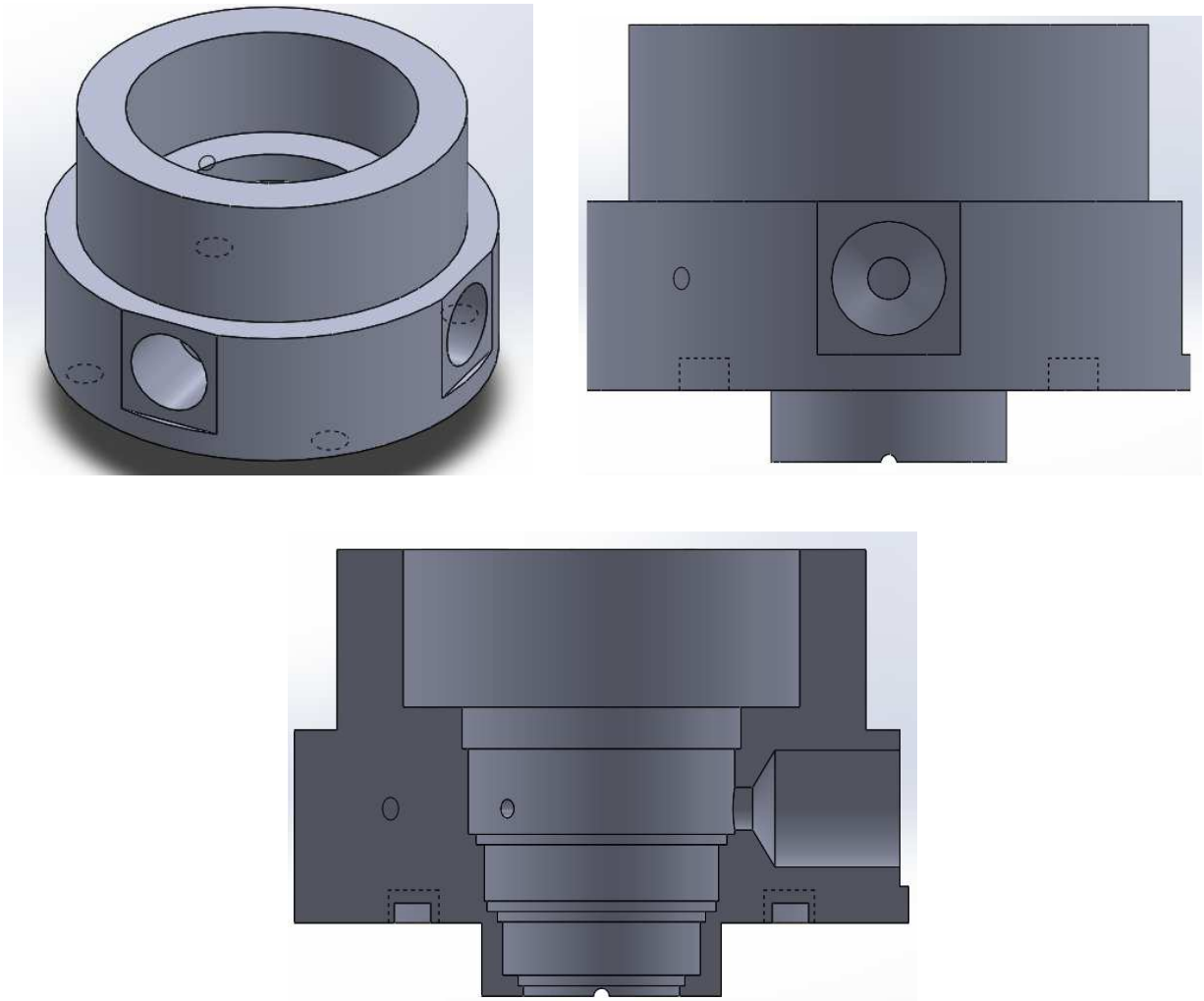
Figure 6.2) 3D Models of the Diverger Lens Barrel
Top left: Isometric view, Top right: front view, Bottom: Cross section

The barrel has a top diameter of 2 inches to allow it to be mounted and controlled using commercial optical mounts. The two large holes separated by 90 degrees on the side are threaded and mate with the Newport BHC17.04 hex adjuster to allow lateral control of the doublet in the assembly. The doublet is locked in placed using a 2-56 screw. At the base of the barrel is a tiny vent to allow air to be extracted, or displaced with solution, using a syringe. Figure 6.3 shows the entire assembly with retaining rings, adjusters, and lenses, but not the O-rings used. O-rings are placed between the lenses and retaining rings to prevent fluid from leaking through the barrel and provide a more uniform force across the surface of the lens.
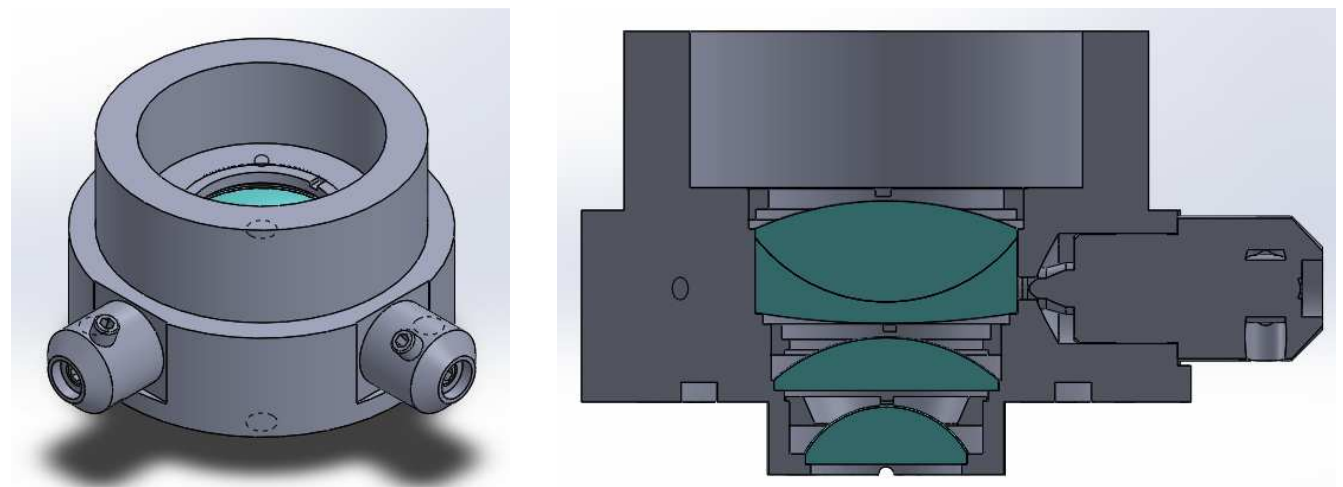
Figure 6.3) Diverger Lens Assembly

This assembly will remain stationary while the tank of solution (and contact lens) is brought towards it, though this raises a concern of saline getting into the groves of the hex adjuster and rusting the screws. To prevent this, a "barrel protector" was designed out of Delrin to prevent the fluid from reaching the adjusters. This does increase the liquid displacement, so it was also designed to reduce displacement where it could.

Figure 6.4 shows the 3D solid model of the barrel protector. There are 4 holes that allow four 10-32 screws through so that the protector can be screwed to the surface of the diverger lens barrel. There is also a grove carved into the middle of it to allow air to escape like the lens barrel, and an O-ring is sandwiched between the barrel and the protector to ensure no saline moves towards the adjusters.
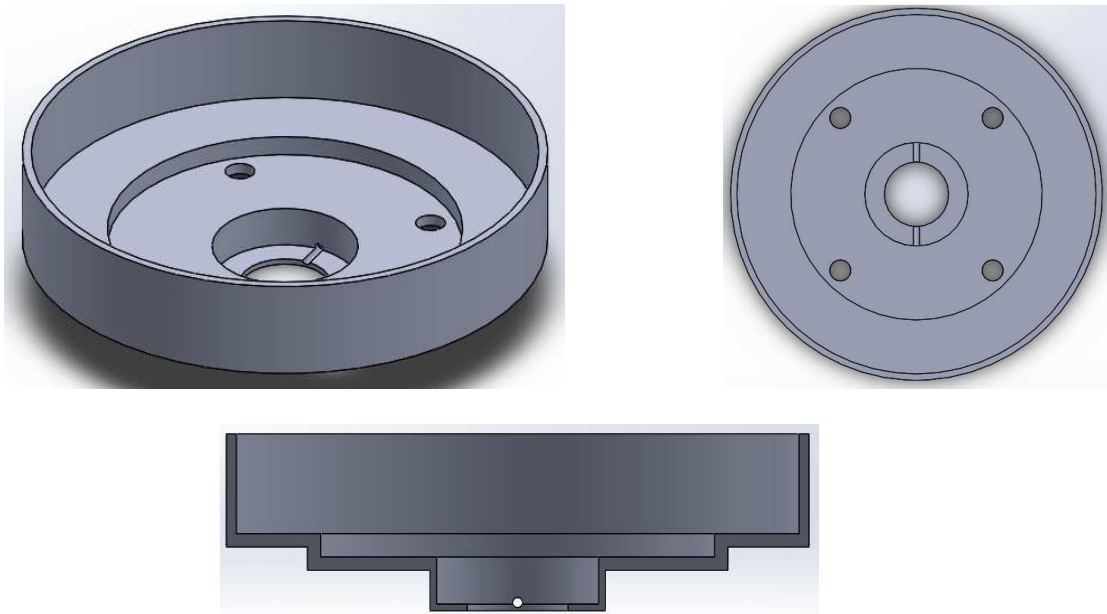
Figure 6.4) 3D model of Barrel Protector
Top left: Isometric view, Top right: top view, Bottom: Cross section

Lastly, the barrel protector also serves as a mounting surface for the test arm quarter wave plate. The wave plate is sandwiched between the protector and lens barrel so that the entire assembly can be rotated to optimize the signal. There is enough gap that solution will have no problem filling in the region between the waveplate and the last lens, but is still close enough to the lens that it will not cause signal degradation as discussed at the beginning of this chapter. Figure 6.5 shows the entire diverger lens assembly without the waveplate and O-rings.
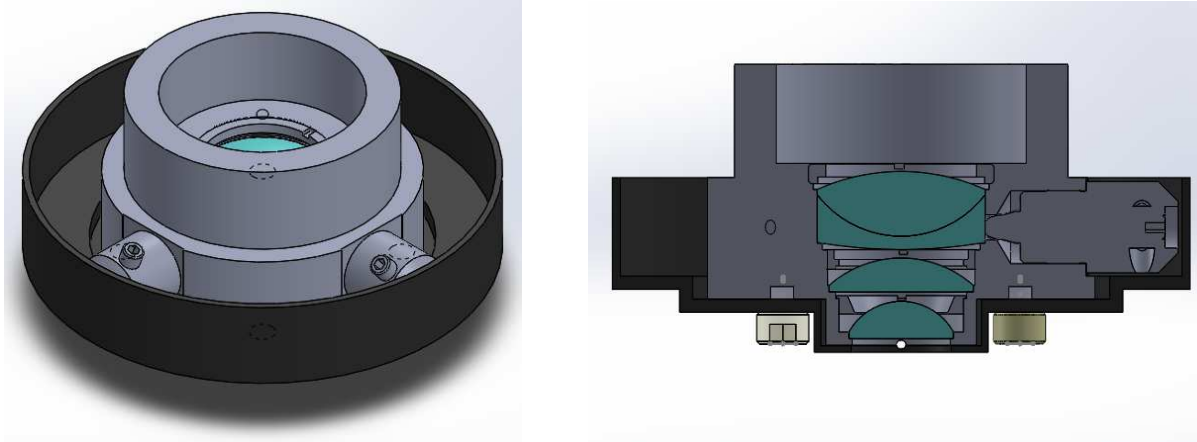
Figure 6.5) Barrel and Protector Assembly

6.3 Test Arm Tank

The test arm tank was designed to be lightweight and volume optimized such that the liquid displacement would not overflow from the tank. It has a 1 inch base that allows it to be used with standard 1 inch optical mounts for support and control. The mount chosen to hold the tank along with the two Newport AG-LS25 piezo linear stages take up 0.86 lbs of the 2.5 lbs weight limit. To ensure that the tank would not be too heavy and compatible with saline, the tank was designed out of Delrin giving it a total weight of 0.293 lbs. Figure 6.6 shows a solid model tank.
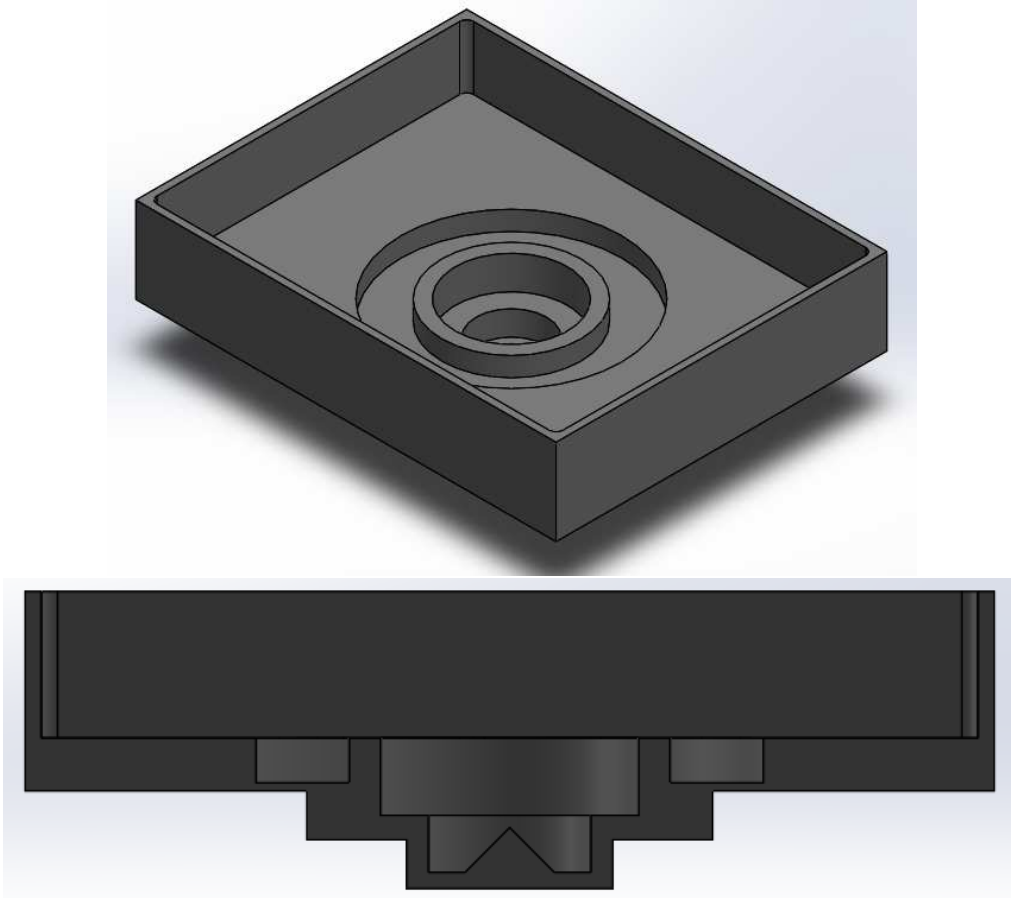
Figure 6.6) Test Arm Tank

As it can be seen from the isometric view of the tank, there is an annular recess around the central portion of the tank. This is to prevent the four 10-32 socket head screws from colliding with the tank when the main reservoir base (the large open area) approaches the barrel protector. The cut is annular to allow the lens barrel to freely rotate to optimize the quarter wave plate's fast axis position.

The central features are easily viewable in the cross section image. There is a cone built into the tank to scatter the light transmitted through the contact lens and reduce the background noise on the detector. With the lack of saline to air reflectance in the optical path and this cone baffle, the signal from the contact lens should be much easier to detect than in the previous iteration of LOCOH.

The last feature to notice about the tank is the small circular cut just above the cone baffle. This region holds the contact lens mount which will be discussed in the next section.

6.4   Contact Lens Mount

The contact lens mount is a relatively simple design and can basically be thought of as a washer. It is made out of anodized aluminum like the tank to ensure the tight tolerance could be met for the surface profile. Unlike the microscope slide from before, the metal could be fabricated to a particular flatness with very little surface error. Figure 6.7 shows a solid model of the contact lens mount.
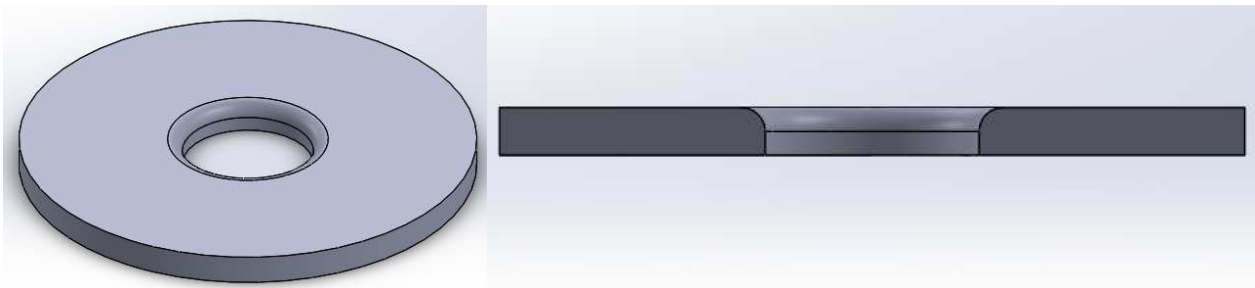
Figure 6.7) Solid model of a Contact Lens mount

The outer diameter is designed such that the mount can be slip fitted into the central region of the tank. The height of that central region and the washer account for the typical sag of the contact lenses so that the baffle will not directly touch the contact lens.

Three different inner diameters were designed to test mounting difference. The three diameters were chosen to be 9mm, 10.5mm, and 13 mm to avoid any reinforcement rings or zone changes in the contact lens. A 1mm radial chamfer was placed on edge of the inner diameter so that no sharp edge would cut the contact lens. This would provide a more ideal ring support as well since there is only a single line along the spherical surface that will mate with the contact lens. Figure 6.8 shows a cross section view of the tank and contact lens mount with an arbitrarily generated contact lens. Figure 6.9 shows all components discussed as a complete assembly.

72
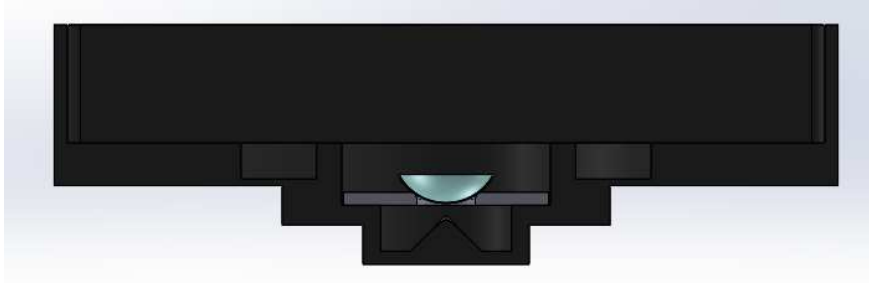
Figure 6.8) Cross Section View of the Tank with the Contact Lens Mount
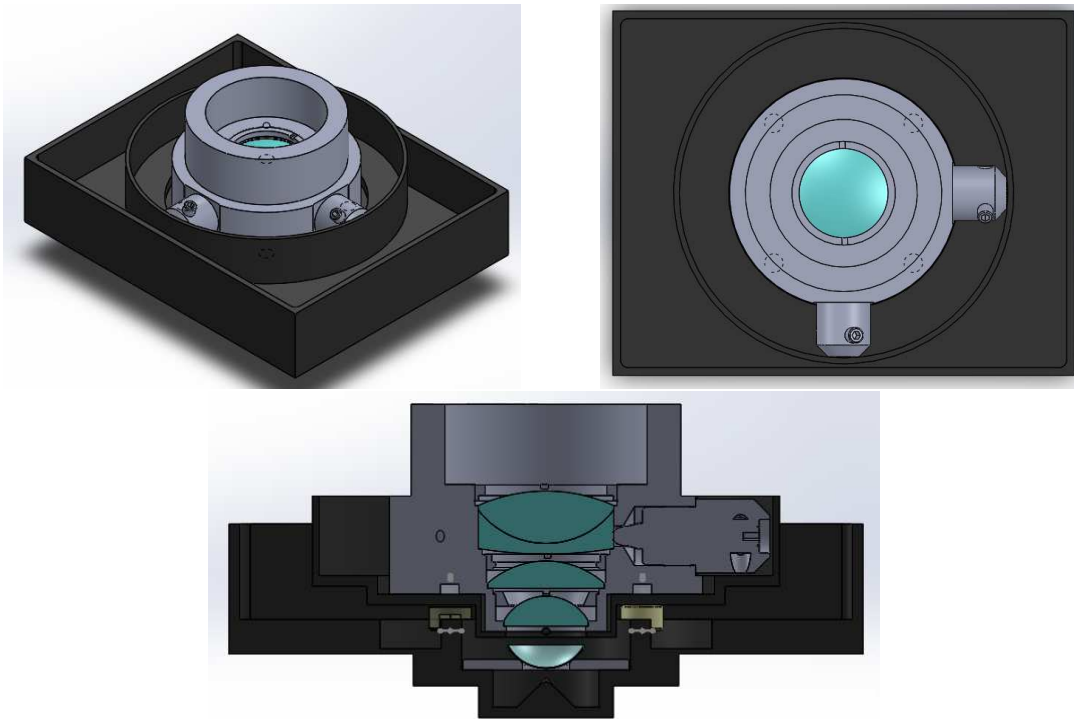
Figure 6.9) The Complete Test Arm Assembly with a Contact Lens

6.5 Volume Displacement

To determine the amount of solution necessary for the measurement, the components were spaced in Solidworks, while accounting for the sag of the contact lens with the 9mm mount, so that system would be in a confocal measurement for the posterior surface. In order to ensure that the solution reaches the back surface of the null assembly, a solution height of 5.65 mm from the main reservoir floor was required. To allow some room for error, it was assumed that solution height would actually be 6.15 mm. Considering the regions below that height, this corresponds to a volume of 74.03

mL. The horizontal yellow lines in Figure 6.10 show the height of the saline solution. For reference, 74.03

mL of water has a weight of about 0.163 lbs; therefore, the entire assembly supported by the linear

stage weighs about 1.337 lbs which is within the weight restriction.
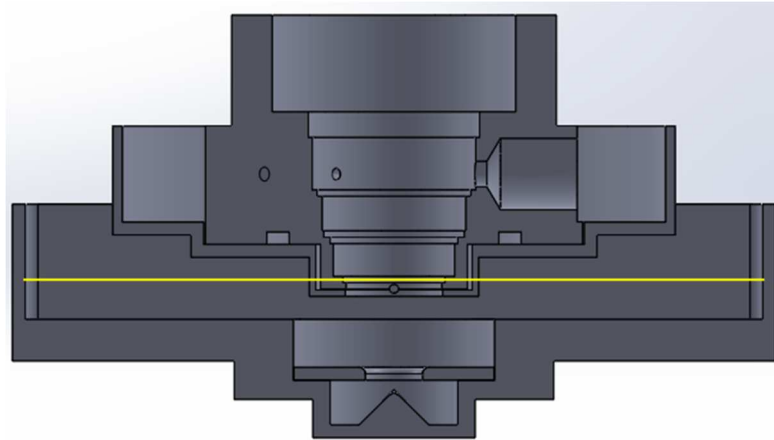
Figure 6.10) Assembly in confocal position
The yellow line represent the solution height needed

In the cat's eye position for the 74.03 mL volume, the solution height will be displaced such that it

rises to 14.44 mm from the main reservoir floor. The tank was designed to overshoot the requirement

and have a main reservoir height of 18mm which corresponds to a solution height at confocal of 7.6 mm

or an overall volume of 89.08 mL. At this volume, the weight of the liquid will now be 0.196 lbs which

still satisfies the weight restriction. Figure 6.11 shows the assembly in the confocal position with the

solution height marked.
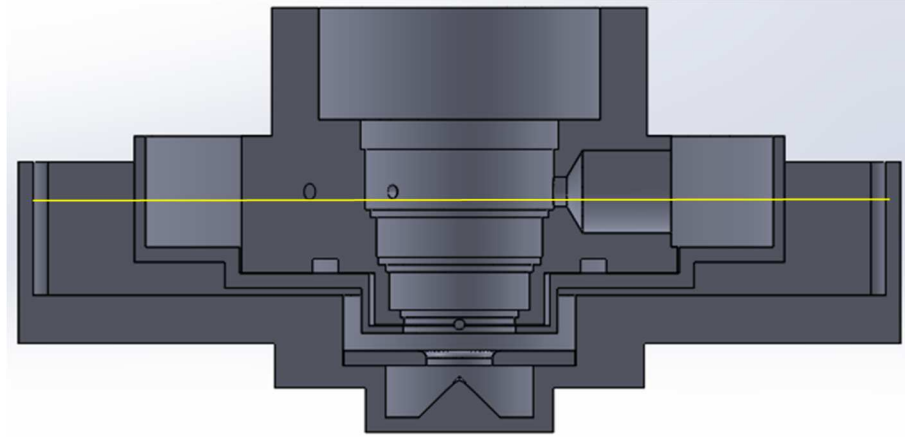
Figure 6.11) Assembly at the cat's eye position

It should be noted that for the liquid displacement analysis, small grooves like the gap between the barrel protector and diverger lens barrel, were neglected. The volume of these small areas have insignificant impact on the overall liquid displacement; however, there effect actually reduces the required liquid height. Since this design and analysis was performed with a solution amount larger than required, there is plenty of room for user error in filling the tank.

6.6   Collision Analysis

With the previous design, the contact lens mount could be lowered to a point where the arms holding the glass plate would collide with the diverger lens barrel/ tank. Before this could occur, however, the glass plate would be caught by a wall on the tank 2.5 mm away from the last optical surface in the diverger lens. The user could visually tell that the collision would occur through the software since the image magnification of the surface would stop increasing on the camera. This was a nice feature, but it also prevented an accurate cat's eye measurement for the anterior surface due to the 2.5 mm limit, the thickness of the glass plate, and the sag of the contact lens.

For this build, the mount thickness, tank depth, and diverger lens assembly extrusion length were designed such that the second surface cat's eye could be measured, but the contact lens would not

collide the diverger lens assembly. This cat's eye measurement will occur before the collision point of the diverger lens and tank, but there should be concern if the tank was raised beyond the cat's eye measurement position or an overshoot occurred in getting to that position. There will be no visual cue on the camera like before if the components are about to collide. So, it is up to the user to watch the actual components prior to collision; however, there will be a greater surface area overlap if the collision occurs which should be fairly obvious.

The new concern is that if the collision does occur, will the contact lens be damaged or crushed between the mount and the diverger lens assembly? Figure 6.12 shows the components at the point of collision. The yellow line in the figure shows the distance between the surface of the waveplate and the lowest ring contact point of the chamfered edge of the contact lens mount. Looking at the drawings specifications for several contact lenses, it was found that from the highest ring contact point (the top of the mount) to the waveplate surface, the minimum separation limit (the yellow line) had to be 2.293 mm. For this design, the separation achieved is 3.59 mm.
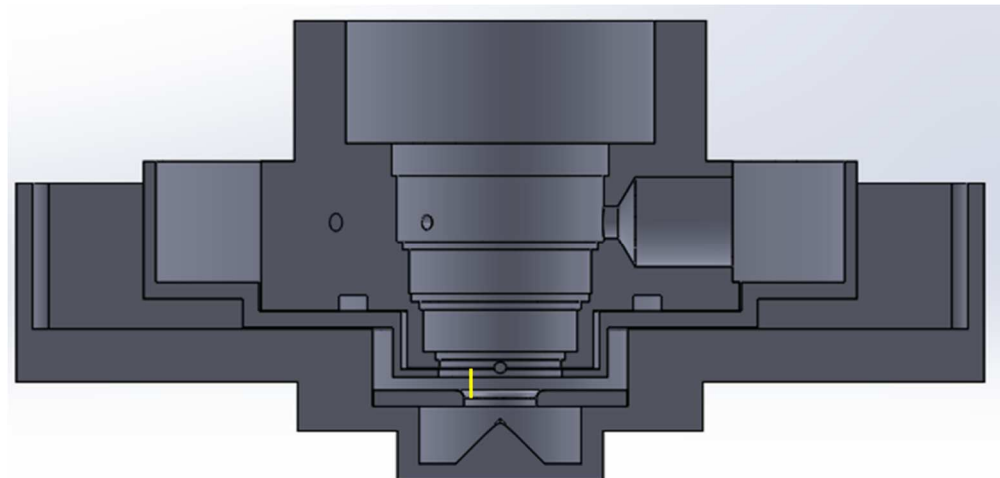
Figure 6.12) Tank and Diverger Lens at Collision
At the point of collision, the main reservoir floor of the tank will collide with the barrel protector of the diverger lens

7   Software Improvement

The mechanical design changes shown in the previous chapter greatly improve the fringe visibility performance of the interferometer as well as the contact lens stability; however, further performance improvements can be achieved if some of the software issues are addressed. In particular, although the phase unwrapping algorithm works well enough, many recovered phase profiles contained streaks in the profile or patches of data loss as shown in Figure 7.1. This will in turn effect the Zernike fitting and ultimately the accuracy of the surface profile.
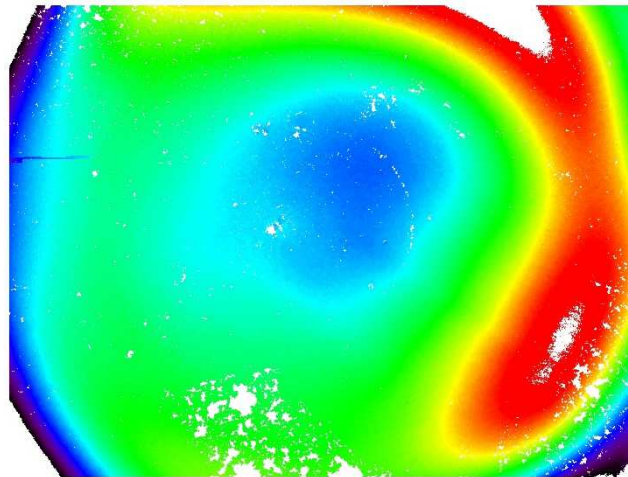
Figure 7.1) Unwrapping errors
A streak due to error propagation can be seen on the left edge of the profile. Lack of data from poor masking can be seen at the bottom of the profile. The missing regions within the red portion of the phase is simply due to a plotting error, and not an unwrapping error.

As mentioned previously, the initial build of LOCOH utilizes a quality guided raster method for phase unwrapping. In other words, starting from a seed point, pixels are unwrapped along a column while accounting for bad quality. When the whole column has been processed, the next pixel along a row is selected as the next starting point and the next column is processed. As a measure of quality, pixels are only unwrapped if their visibility exceed 10%. This is troublesome since the average visibility for LOCOH measurements is around 15%. Many pixels are not actually unwrapped, and a mask is applied

after the unwrapping process to null out those data points. These appear as the patches of data-less

pixels shown in Figure 7.1.

Though this unwrapping procedure has yielded results, a new method has been proposed and

demonstrated which yields significantly better results. The method itself is common to phase

unwrapping, and is known as a quality guided flood fill method. This chapter will discuss the parameters

necessary in the method as well as address issues with the previous method.

7.1   Phase Residues

7.1.1   Residue Definition

The first step in the new method is to understand the existence of phase residues from a

recovered phase profile. For phase unwrapping to work, it is generally assumed that the surface being

measured is smooth and continuous. That is, there are no discrete pockets of sudden data shift or there

are no poles in a complex equation to describe that surface. Unfortunately, due to measurement errors

such as noise or pixel errors, this is often not the case with LOCOH.

Since phase is always a complex value, phase residues are analogous to complex function

residues. Consider a function of a complex variable z where

$$z = x + iy$$

<div align="right">(7.1.1)</div>

The Laurent Series expansion of the function $f(z)$ will include terms that contain $(z - z_i)^{-1}$, and the

coefficients of these terms are complex residues. Therefore, $f(z)$ is analytic in the region everywhere

around z_i but not at the location of z_i. Similarly, a profile can be appropriately unwrapped everywhere

except at the point of a phase residue. Consider the example provided by (Ghiglia & Pritt, 1998) of a

complex signal $s(x, y)$ as shown below where the magnitude $|s(x, y)|$ contains no poles.

$$s(x, y) = |s(x, y)| \exp\{j\varphi(x, y)\} \tag{7.1.2}$$

To be complete, $s(x, y)$ can be expressed a function of both a complex value and its complex conjugate $\bar{z}$. That is,

$$s(x, y) = f(z, \bar{z}) \tag{7.1.3}$$

$$where \; \bar{z} = x - iy$$

Performing the Laurent series expansion of $s(x, y) = f(z, \bar{z})$, we will see that

$$f(z, \bar{z}) = \sum_{n=0}^{\infty} \sum_{m=0}^{\infty} a_{mn}(z - z_0)^m (\bar{z} - z_0)^n \tag{7.1.4}$$

Note that there are no negative powers in the expansion since $s(x, y)$ contains no poles. It is likely that at some point $z = z_0$, $f(z_0)$ will equal 0 which leads to

$$f(z, \bar{z}) \approx a_{1,0}(z - z_0) + a_{0,1}(\bar{z} - z_0) \tag{7.1.5}$$

where $a_{1,0}$ & $a_{0,1}$ are the appropriate expansion coefficients for equation (7.1.4). The phase can now be analyzed in the vicinity of this point if equation (7.1.5) is rewritten as

$$f(z, \bar{z}) \approx (a_{1,0} + a_{0,1})r\cos\theta + j(a_{1,0} + a_{0,1})r\sin\theta$$
$$\tag{7.1.6}$$

$$\theta = \angle(z - z_0) \quad and \quad r = |z - z_o|$$

By normalization, the sum of $|a_{1,0}| + |a_{0,1}|$ can be set to 1 which will generally lead to

$$a_{1,0} = \alpha \exp(j\gamma_1)$$
$$\tag{7.1.7}$$

$$a_{0,1} = (1 - \alpha)\exp(j\gamma_2)$$

Where α is in the range of [0,1] and γ_1, γ_2 are arbitrary angles. This will change equation (7.1.7) to

$$f(z, \bar{z}) = f(r, \vartheta) = r \exp(j\beta)[\alpha \exp(j\vartheta) + (1 - \alpha) \exp(j\vartheta)]$$

$$\vartheta = \theta + \frac{\gamma_1 - \gamma_2}{2} \quad and \quad \beta = \frac{(\gamma_1 + \gamma_2)}{2} \qquad (7.1.8)$$

Now, the term inside the brackets can be expressed as

$$g(\alpha, \vartheta) = [\alpha \exp(j\vartheta) + (1 - \alpha) \exp(j\vartheta)] \qquad (7.1.9)$$

Than the wrapped phase can be expressed as

$$\varphi = \angle f(r, \vartheta) = \beta + \angle g(\alpha, \vartheta) \qquad (7.1.10)$$

Since β is a constant phase, it can be ignored and we can say that

$$\varphi = \angle g(\alpha, \vartheta) = \arctan\{(2\alpha - 1)tan\vartheta\} \qquad (7.1.11)$$

Due to the $tan\vartheta$ in equation (7.1.11), the phase will always have a π ambiguity that cannot be resolved.

Consider a 2x2 array of wrapped pixels. In the existence of a phase residue, starting at the lower left pixel will show that the lower right pixel is off by a factor of 2π. The second pixel is than corrected for the error by unwrapping; however, now the top right pixel is off from this second pixel by a factor of 2π. Again, the unwrapping is done which propagates the error to the top left pixel. After this pixel is unwrapped, in the existence of a phase residue, it will now be off by a factor of 2π from the first pixel and the loop could run indefinitely in an attempt to smooth out all four pixels. This is shown in Figure 7.2.
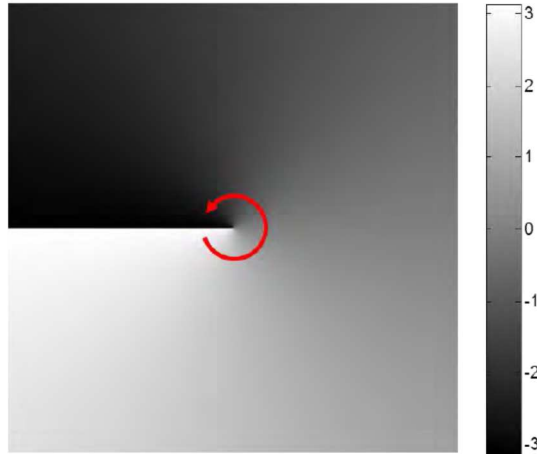
Figure 7.2) Phase Residue
(Jason Daniel Micali, 2015)

To avoid this error, typical unwrapping routines mask out these residues so that they do not propagate errors. Since routines often only visit a pixel once when unwrapping, if this ambiguity is attempted to be unwrapped, the pixels following the unwrapped ambiguity propagate a 2π error which leads to the streaks shown in the profile in Figure 7.1.

7.1.2 Residue Detection

With residues now understood, residue detection is actually rather simple. Simply stated, residues occur whenever the integral around a closed path is not equal to zero. That is

$$\oint f(z)dz \neq 0 \qquad\qquad (7.1.12)$$

For phase measurements, this integral can be represented as the summation of the difference between pixels. Consider another example given by (Ghiglia & Pritt, 1998) which is an array of pixel values as shown in Figure 7.3. It should be noted that these values are actually the wrapped phase, $\psi =$

$tan\ \varphi$, and represent cycles of 2π; therefore, each value should be multiplied by 2π to obtain ψ at those pixels. If the top quadrant of pixels is considered, the closed path integral can be found from

$$q = \sum_{i=1}^{4} \Delta_i = -0.2 - 0.1 + 0.4 - 0.1 = 0 \qquad (7.1.13)$$
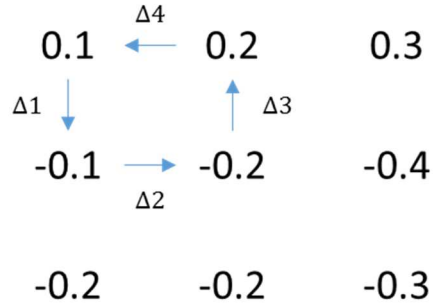
Figure 7.3) Closed path of 4 pixels with no residue

Since this summation results in a zero, this portion of the phase is continuous and does not contain any phase residues. Now, if a different path is consider, as shown in Figure 7.4, the new path integral results in a value other than 0 indicating a phase residue.

$$q = \sum_{i=1}^{4} \Delta_i = -0.4 - 0.2 - \mathbf{0.3} - 0.1 = -1 \qquad (7.1.14)$$
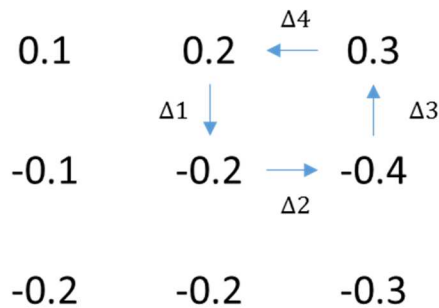
Figure 7.4) Closed path of 4 pixels containing a residue

To clarify the values in equation (7.1.14), it should be noted that the wrapped values are bounded between $[-\pi, \pi]$, so

$$\Delta 3 = \mathcal{W}\{2\pi[0.3 - -0.4)]\} = -0.3$$

$$\text{Since} \quad \tan(2\pi * 0.7) = \tan(2\pi * -0.3)$$

For a visual example, Figure 7.5 show the tangent of x from $[-2\pi, 2\pi]$. As mentioned earlier, wrapped values are restricted to the region of $[-\pi, \pi]$ so any value beyond π such as $0.7*(2\pi)$ is mapped back to the equal value within $[-\pi, \pi]$.
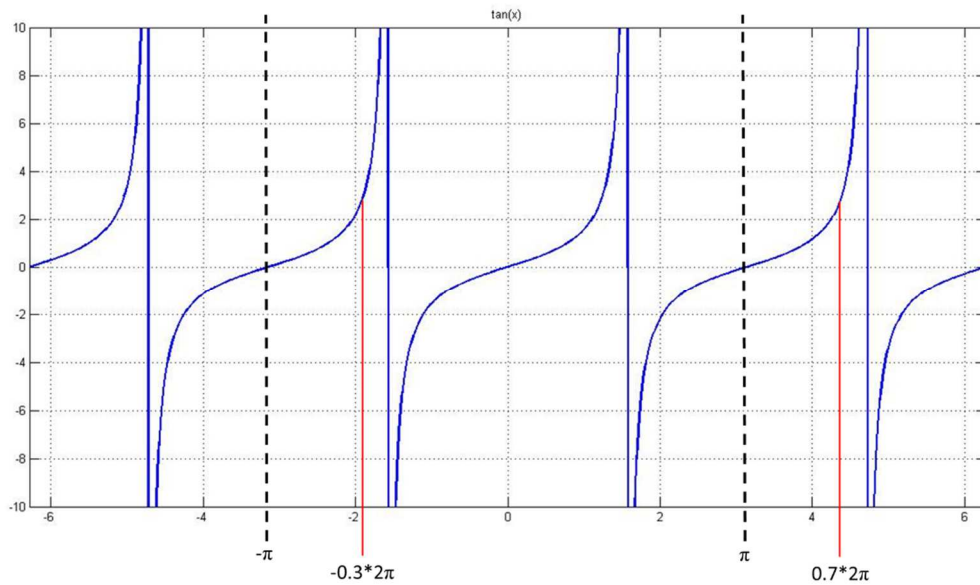
Figure 7.5) tan(x) from -2π to 2π
Note that the wrapping result is bounded between $-\pi$ and π so 0.7 must be represented as -0.3

7.2   Quality Guidance

As mentioned previously, the process of phase unwrapping is done on a pixel by pixel case, and there is not necessarily a correct order to unwrapping. Assuming the surface is continuous and smooth, the starting pixel can be located anywhere in the profile. The only requirement is that the next pixel to be unwrapped should follow from an already unwrapped pixel since all unwrapping will be relative to the starting point. Unfortunately, it is often not safe to assume the data captured by a camera is completely continuous and smooth, and there may be noise errors which lead to phase residues.

Generally, it is ideal to have a quality map define which pixel should be unwrapped and in what order. The quality map will assign each pixel a quality value which can aid in determining a good starting pixel, which pixels to avoid, and which to address last so that errors do not propagate. Generally, the location of a phase residue often returns a bad quality; however, this is not always true.

7.2.1   Visibility

The quality map that the first build of LOCOH utilizes is a map generated from visibility. As mentioned in section 2.3, visibility is a measure of fringe modulation at the detector plane. The equation to define visibility is given in equation (2.3.1), and the values are restricted between 0 and 1 (0-100%). Since the camera captures 5 frames of phase shifted data, visibility for each pixel can be determined by using the equation

$$Visiblity = \frac{2\sqrt{(I_4 - I_2)^2 + (I_1 - I_3)^2}}{I_1 + I_2 + I_3 + I_4} \qquad (7.2.1)$$

Where I_1, I_2, I_3, and I_4 are the different intensity from frames 1-4 of each pixel.

This is a rather simple and informative map to generate regarding the pixels where the highest quality is 1, and the lowest is 0. Figure 7.6 shows a single frame of data, the extracted wrapped phase of data, the visibility map corresponding to the data, and a histogram of that visibility pixel values. This particular data was captured with a small air bubble between the waveplate and the contact lens which lowers the return intensity from regions of the measured contact lens. Though, this data would not be accepted as a sufficient measurement, it does well to demonstrate how visibility can be used as quality map.
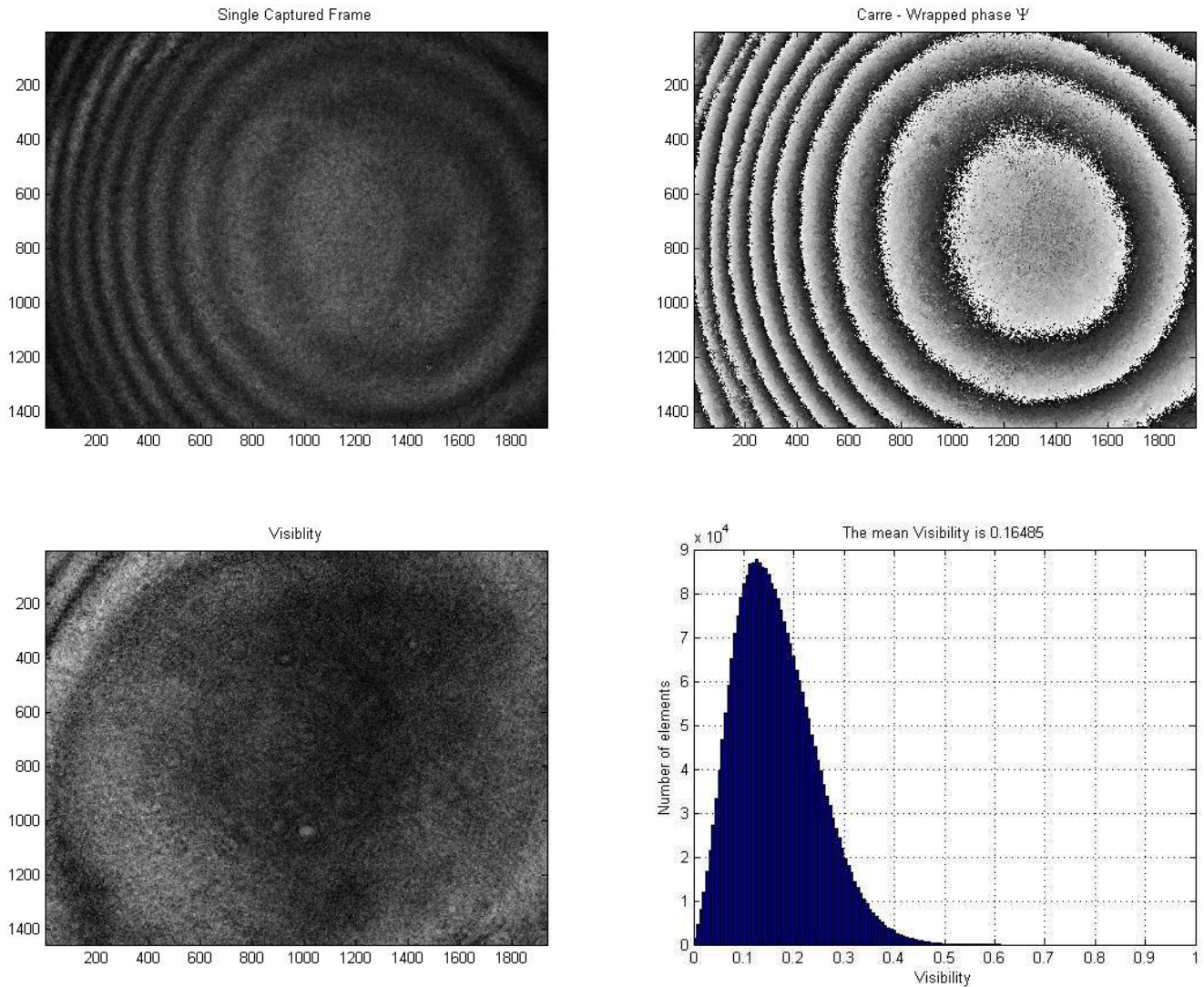
Figure 7.6) Visibility of a near cat's eye measurement

Note that there is a bright region in the center of the single frame capture which is common to all LOCOH measurements. It appears a circular spot that is about half of the frame size. This is the light reflected from the second surface of the contact lens. Because it is outside of the coherence length of the source, it does generate or add to the fringe pattern; however, it does lower visibility for those pixel as shown by the darker region in the visibility map.

7.2.2 Phase Derivative Variance

Since it was demonstrated that the initial build of LOCOH lost patches of data while using a visibility guided method, another quality metric was investigated which utilized the derivative of the phase profile or phase slopes.

Phase derivative variance (PDV) is actually a quality map technique often used in Synthetic Aperture Radar (Ghiglia & Pritt, 1998); however, the technique can also be applied to optical interferometry captured phase profiles. PDV is often chosen for synthetic aperture radar because it does a superior job at isolating shear planes compared to that of correlation and pseudo correlation maps. The method is also easily corrupted by noise, therefore, areas of noise will easily appear which can be masked out.

As the name implies, the algorithm determines the variance of the slope data in smaller windows. In more detail, the equation is actually a root-mean square measure of the variance and it is given by

$$
z_{m,n} = \frac{\sqrt{\sum\left(\Delta_{i,j}^x - \overline{\Delta_{m,n}^x}\right)^2} + \sqrt{\sum\left(\Delta_{i,j}^y - \overline{\Delta_{m,n}^y}\right)^2}}{k^2}
\tag{7.2.2}
$$

The equation works by operating within a $k\,x\,k$ window and the subscripts i, j represent pixels within that $k\,x\,k$ window. The subscripts m, n represent the unwrapped pixel being assigned the PDV value

and Δ^x, Δ^y are the partial derivatives (in x and y) of the wrapped phase. The symbols $\overline{\Delta^x}, \overline{\Delta^y}$ are the average partial derivative values within the $k \: x \: k$ window.

Ideally, good quality data is data that has low phase slopes which would mean that bad data has high phase slopes. To make use of PDV as a quality map, the map is often inverted such that low slope data corresponds to values of 1, and bad slope data corresponds to values of 0. To invert the data, the PDV values are normalized, and then the absolute value of the normalized PDV minus one is recorded. This is shown below for clarification were i, j represent the pixel being assigned the quality map value.

$$Inverse \: PDV_{i,j} = \left| \frac{PDV_{i,j}}{Max(PDV)} - 1 \right| \qquad (7.2.3)$$

Using the same single frame data and phase extraction method as shown in the previous section, Figure 7.7 shows the PDV quality map generated for a surface and the histogram of the PDV values per pixel. Note that PDV quality map is shown in grayscale where 100% is white, and 0% is black.
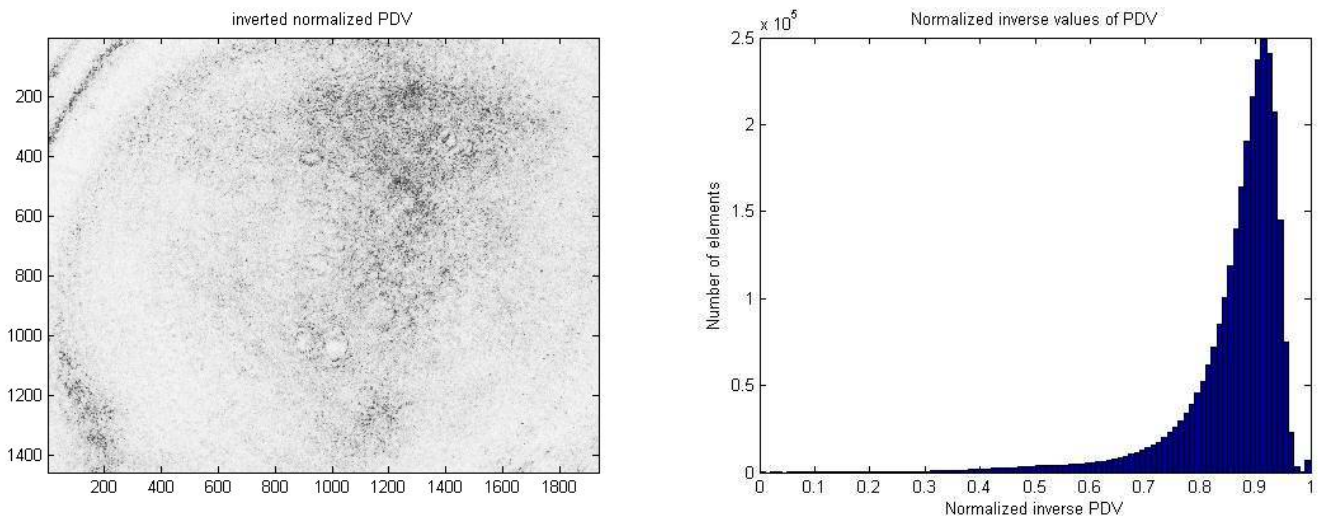
Figure 7.7) PDV of a near cat's eye measurement

As shown, PDV provides a clearer resolution of data than that of visibility; however it is slightly more intensive to calculate.

7.3   Masks

Masks serve an important role in phase unwrapping by telling the algorithm which pixels should

not be unwrapped. These are often noisy pixels which are likely to corrupt the unwrapping and

propagate errors. In the original algorithm for LOCOH, a visibility threshold was used that prevented any

pixel with a visibility value lower than 10% from being unwrapped. This was mostly sufficient in

removing residues; however, there was a significant cost of data that may have not been necessary to

throw away. To get an ideal of the visibility mask, Figure 7.8 shows which pixels violate the 10%

threshold, represented as black points, for the same profile shown in the previous sections.

Visiblity-mask with threshold = 0.1
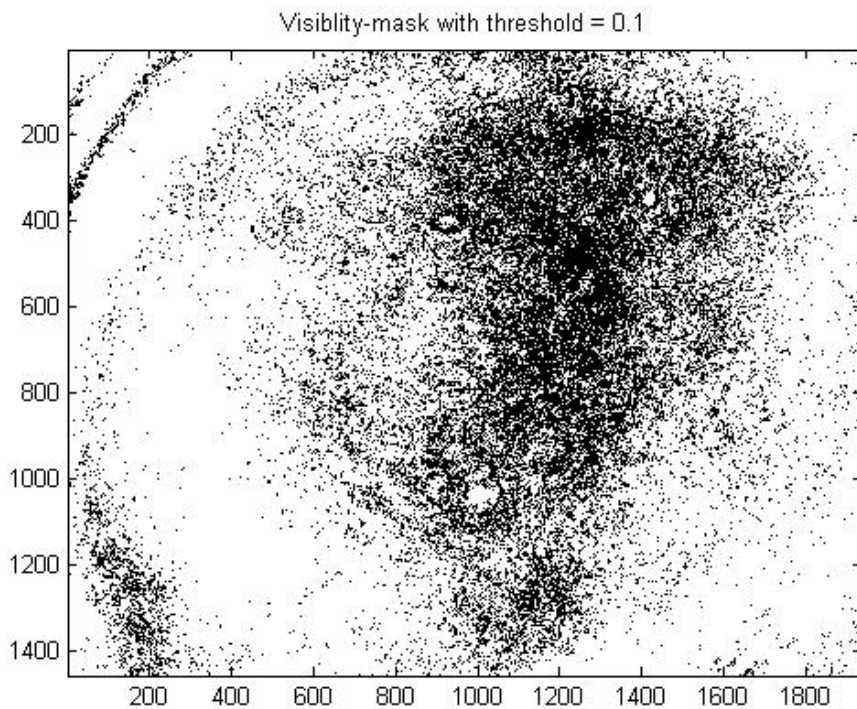
Figure 7.8) Visibility Mask

Obviously there is significant data loss in the profile using this threshold map. PDV was shown to

have better selectivity; however, a threshold for PDV is not as easily decided as visibility. In the case of

visibility, it is often common practice to assume 10% visibility is noisy, but there are no common PDV

thresholds. Rather, Pritt and Ghiglia suggests finding the local minimum of the histogram curve for PDV; however, viewing the previously shown histogram curve in Figure 7.7 would indicate that there is no local minimum. In order to get around this problem, an algorithm was written which removed the top and bottom 5% of data from the histogram. Afterwards, a check was done by comparing the number of elements in each bin and finding the lowest bin value where the following bin had at least a 5% increase in pixels compared to all the previous bins. This value was chosen since Pritt and Ghiglia stated a 5% increase in pixels should eliminate false noise (Ghiglia & Pritt, 1998). Figure 7.9 shows the PDV mask generated using this threshold method for the same phase profile.
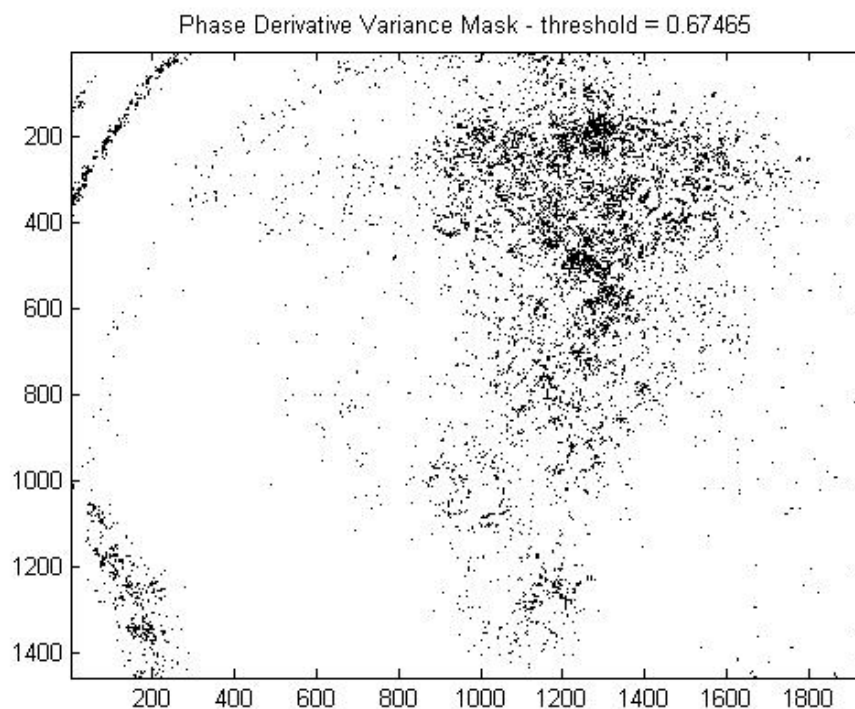
Figure 7.9) PDV Mask

This is mask has better performance as expected; however, both the visibility mask and PDV mask make the assumption that phase residues are contained within the masked out pixels. Rather than running the unwrapping algorithm with this assumption, a phase reside mask should also be applied to

89

ensure that residues are avoided. The problem however is that a residue exist from the combination of 4

pixels. To keep things simple, all 4 pixels containing a residue should be masked out, and this is shown in

Figure 7.10.
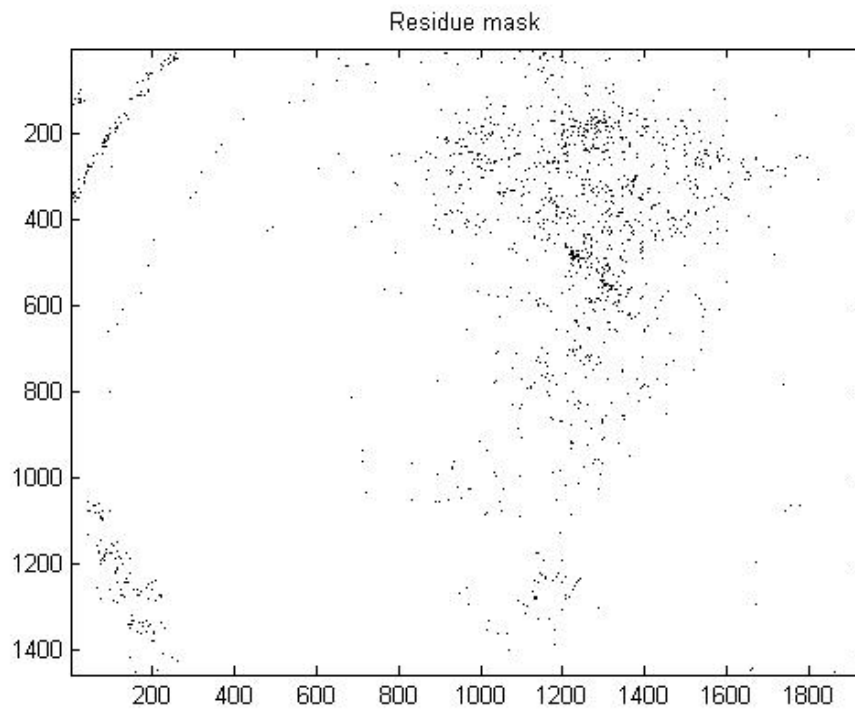
Figure 7.10) Residue Mask

As it can be seen, this mask blocks out the least amount of pixels and it shows that that the

previous threshold masks do seem to account for the residues; however, using the PDV mask of this

profile as the only quality mask will lead to corrupted unwrapping. Therefore, it is ideal to take

whichever quality mask used to determine noisy data, and multiply that mask by the residue mask to

ensure appropriate unwrapping. Since the mask are binary, multiplication of the mask is equivalent to

stacking the masks.

7.4   Quality Guided Flood Fill Algorithm

Now that all base parameters have been understood, the quality guided phase unwrapping

algorithm can be discussed. Note that there are many other methods for unwrapping that can be found

in the references (Jason Daniel Micali, 2015) and (Ghiglia & Pritt, 1998), but with the static fringes

generated by LOCOH, quality guided flood fill is more than sufficient in returning a clean unwrapped

profile.

Like the raster scanning method, a starting pixel is chosen by finding a pixel with a high quality

value in the central region of the wrapped phase image. Afterwards, a queue is built up of the 4

neighboring pixels to indicate that they should be unwrapped. If the mask defines a neighbor pixel as

bad, it will not be added to the queue. Afterwards, the queued pixels will be sorted from highest to

lowest quality based off the quality map chosen. The highest quality pixel will then be unwrapped

relative to the starting pixel, and the seed point will be updated to be at the unwrapped pixel's location.

This algorithm will continue to repeat; however, if a neighbor pixel has already been unwrapped, it will

be removed from the queue. The algorithm will end when there are no pixels left in the queue to be

unwrapped. To help clarify, a list of the steps is shown below outlining the quality guided unwrapping

method. Figure 7.11 also shows the method to help clarify. Note that the black pixels indicate pixels

which have been masked out.

1. Decide the seed pixel location (i, j)
2. Queue the 4 pixel neighbors $(i + 1, j),\ (i - 1, j),\ (i, j + 1),\ (i, j - 1)$
3. Remove any pixel where the mask indicates a bad pixel or the pixel has been previously
   unwrapped
4. Sort the pixels from highest quality to lowest

5. Perform the unwrapping algorithm on the highest ranked pixel relative to an unwrapped neighbor which is given by the two equations shown below

$$\Delta = round\left(\frac{\left(\varphi(i_{new}, j_{new}) - \phi(i,j)\right)}{2\pi}\right)$$

$$\phi(i_{new}, j_{new}) = \varphi(i_{new}, j_{new}) - 2\pi\Delta$$

6. Mark that unwrapped pixel location as the new seed position (i,j)

7. Remove the newly unwrapped pixel from the queue and mark it as processed

8. Repeat steps 1-7 until all pixels are unwrapped
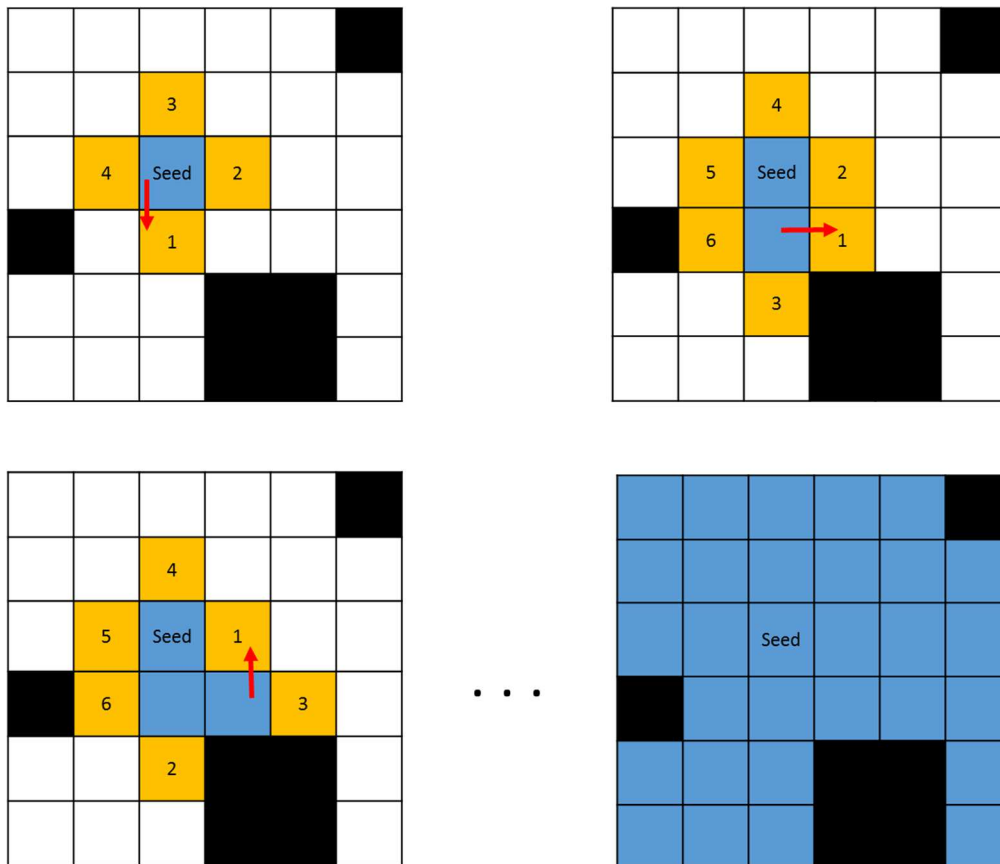
Figure 7.11) Quality Guided Flood Fill Unwrap
Blue pixels are unwrapped, yellow pixels are queued and ranked, black pixels are masked out

7.5   Comparison of Unwrapped Profiles

This chapter has shown various quality guides and masks to help with the unwrapping; however, the question should be asked which combination of masks and quality map provide the best results for unwrapping? For this discussion, the same extracted phase used in the quality maps and masks examples will be used which is shown in Figure 7.12. Recall that this captured data contained a bubble between the waveplate and the contact lens.
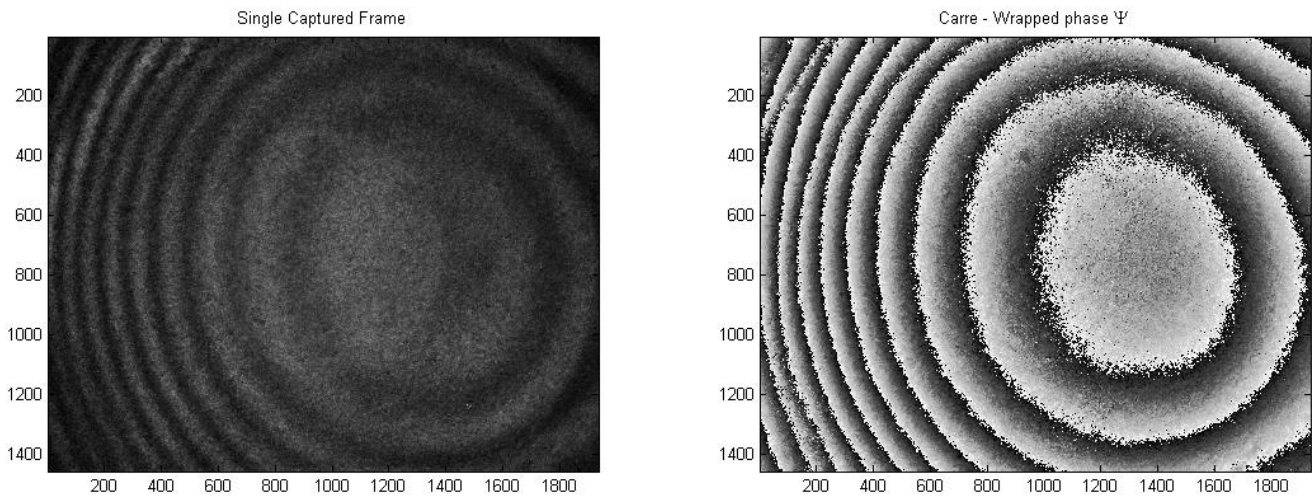
Figure 7.12) Single frame and extracted phase of "Bubbled" near cat's eye measurement

The original unwrapping method of LOCOH did not use quality guidance, but it did define a visibility threshold of 10% as an indicator to remove noisy pixels. Running the original unwrapping algorithm yields the unwrapped phase profile shown in Figure 7.13. As it can be seen, there is significant loss of data in the center.
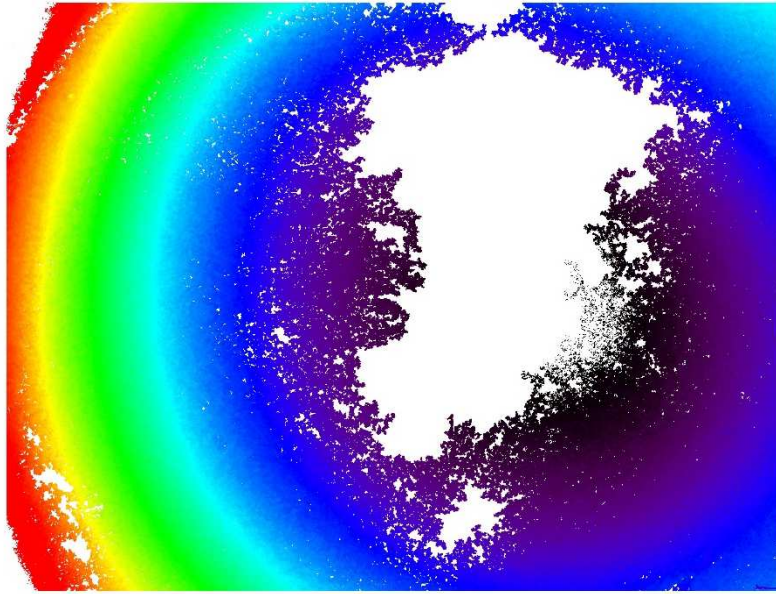
Figure 7.13) Original LOCOH Unwrapping Routine

7.5.1 *Visibility Quality Guidance - Visibility threshold Mask*

If the same 10% visibility mask is applied, but visibility is also applied as a quality map, the

quality guided flood fill method provides the unwrapped profile shown in Figure 7.14. The profile is

generally the same; however, there are a several pixels selected within the void region which were

allowed to be unwrapped. Note however, that they all have values equal to the edge of the profile and

are highly inaccurate. Using only this map and quality guide will not solve the unwrapping problem. Also

note that the original LOCOH unwrap was not done in IDL (Exelis Visual Information Solutions, 2013），

whereas the remaining profiles were done in Matlab (Mathworks, 2013).
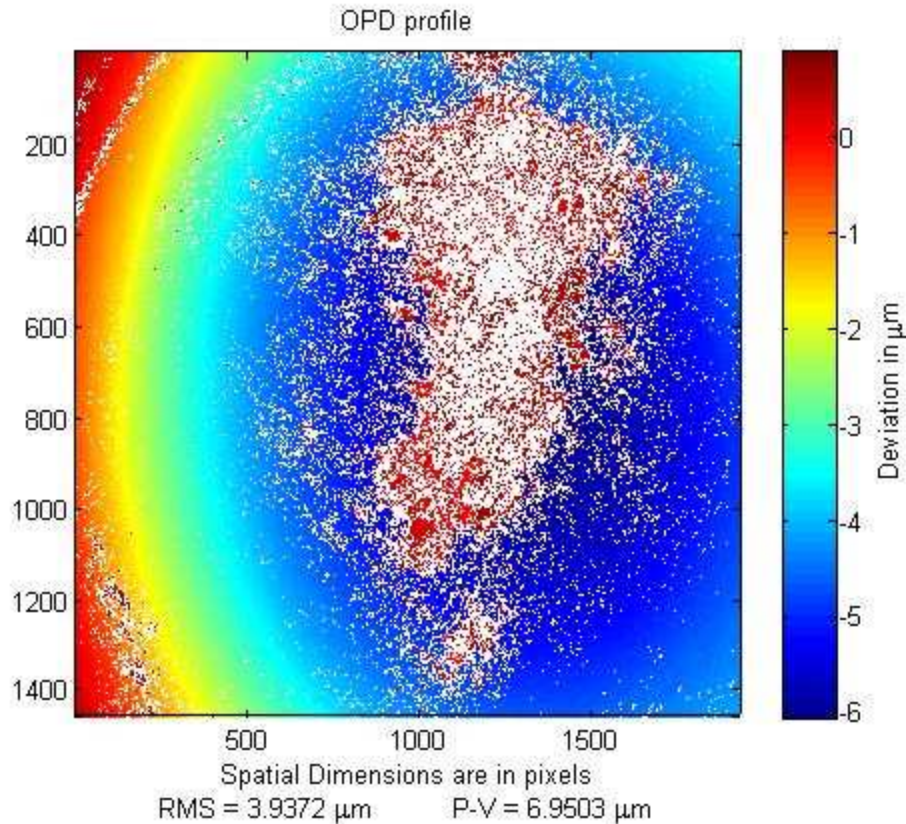
Figure 7.14) Visibility Guided Flood Fill Using 10% Visibility Map

7.5.2 *Visibility Quality Guidance – Visibility threshold and Residue Mask*

As mentioned previously, the IDL unwrapping software did not look for phase residues, if phase residue detection is applied to the previous unwrapping routine, the results are not that much better unfortunately. The 10% visibility threshold of this profile does seem to capture the residues which makes sense since the original unwrapped profile shown in Figure 7.13 does not contain streaks of error propagations. The quality guided flood fill method using a visibility guidance, visibility threshold mask, and phase residue mask is shown in Figure 7.15.
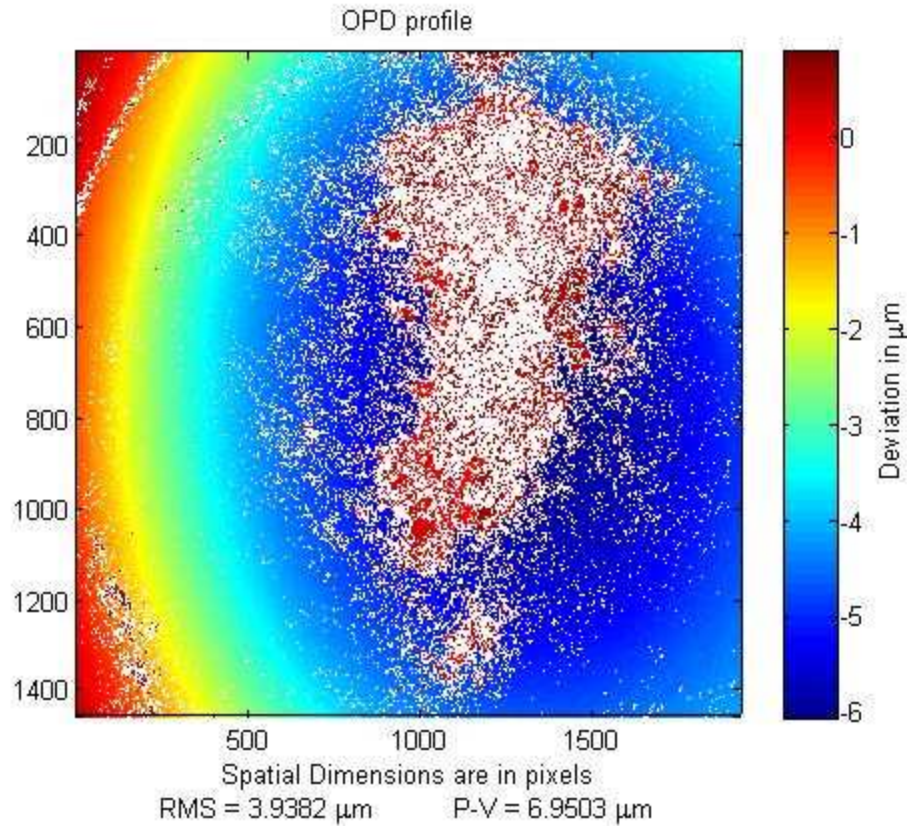
Figure 7.15) Visibility Guided Flood Fill using 10% Visibility Mask and Residue Mask

7.5.3   PDV Quality Guidance – PDV threshold Mask

PDV was shown to have a better separation between high quality and low quality data than the

visibility threshold concept. If the quality guidance is changed from visibility to PDV and only a PDV

threshold is applied, than the resulting unwrapped profile shown in Figure 7.16 is received.
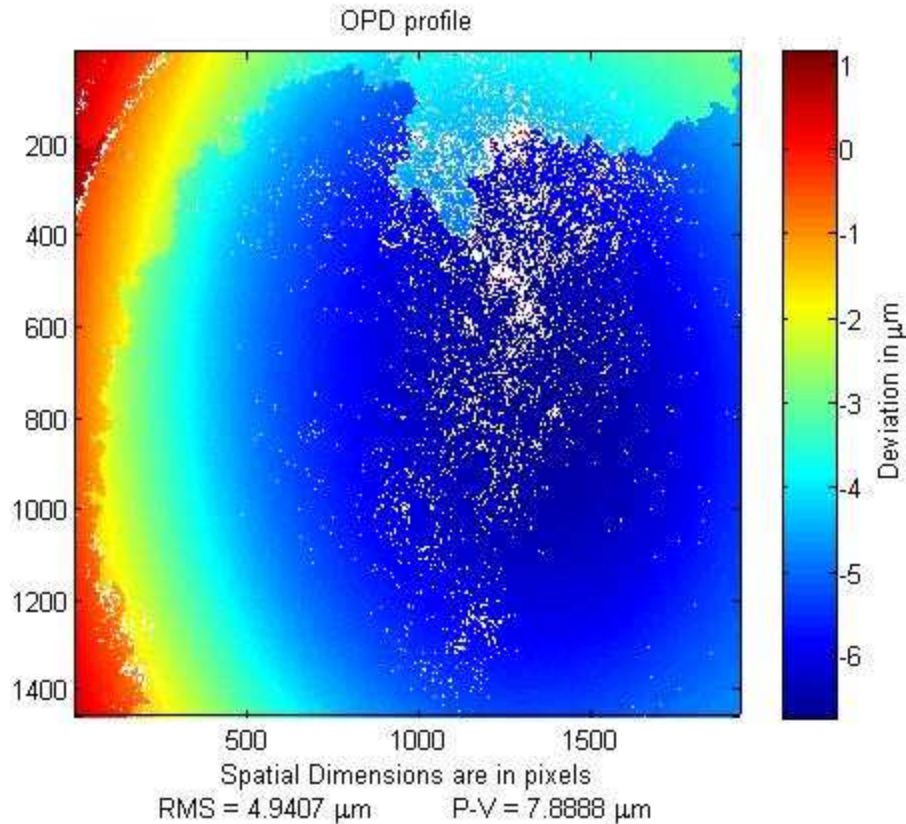
Figure 7.16) PDV Guided Flood Fill Using PDV Mask

As expected, the central region is recovered much better in comparison to visibility; however, the PDV threshold was not sufficient in determining phase residues. This is obvious from the discontinuous look of the phase profile at the top of the profile.

7.5.4 PDV Quality Guidance – PDV threshold and Residue Mask

The obvious next solution is to apply the phase residue mask to the previously unwrapping routine. This is shown in Figure 7.17.
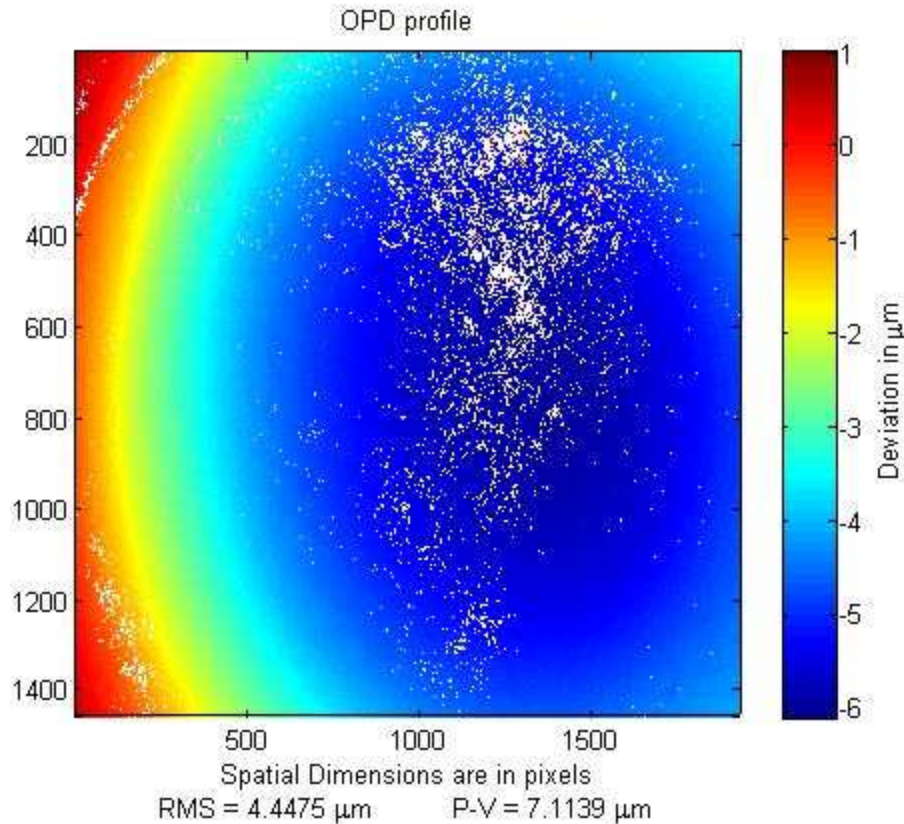
Figure 7.17) PDV Guided Flood Fill Using PDV Mask and Residue Mask

As expected, with residue detection on and the use of the PDV guidance and PDV thresholding, the unwrapped profile provides a significantly cleaner profile than that of visibility. Much of the central region is recovered and the profile is nearly continuous.

7.5.5   Residue Detection Only

Since the routine written was robust enough to handle variable inputs, i.e the type of mask and guidance, a test was performed to see how the unwrapping would handle if only a residue mask was applied and not a thresholding map. The ideal behind the thresholding was to eliminate false data or noise, but perhaps the residues already accounted for false data and noise. Using visibility quality guidance, the unwrapping routine was performed and the result is shown in Figure 7.18.
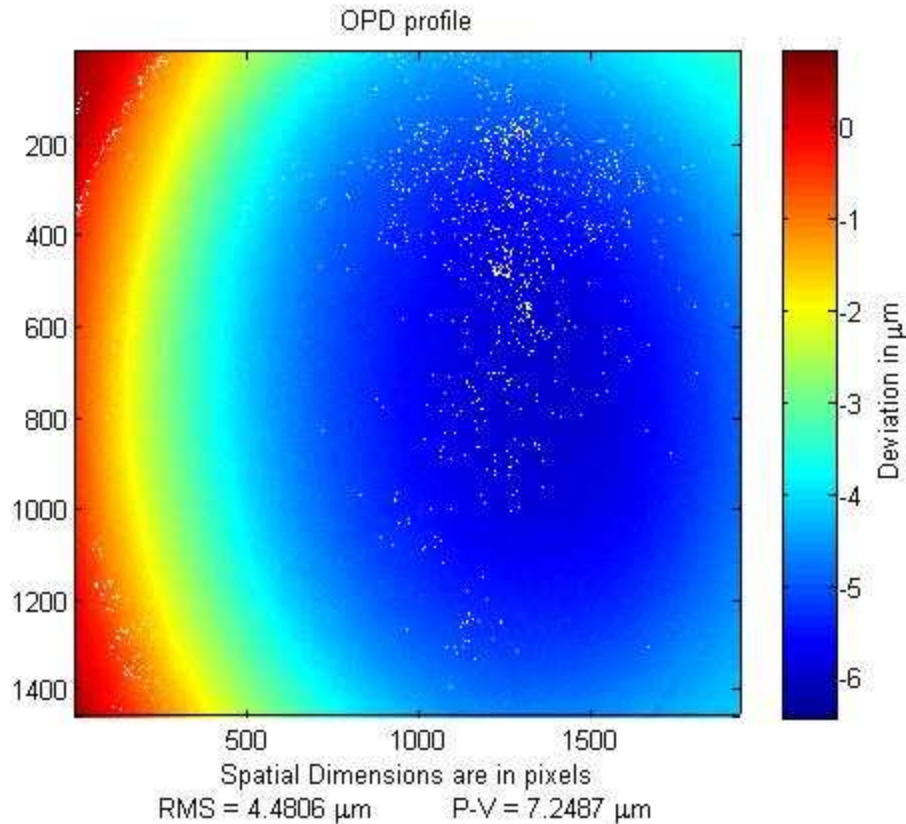
Figure 7.18) Visibility guided Flood Fill Using a Residue Mask

This obviously looks significantly cleaner than all other profiles shown previously, and most of

the data in the central region is still properly procured. This could also be performed using a PDV

guidance rather than visibility guidance, and that result is shown in Figure 7.19. This PDV profile is also

very similar to the visibility guided profile which makes sense. All pixels should be unwrapped except for

where the residue indicates it should not. The only difference is that some pixels may be visited at

different times in the unwrapping process than when using the visibility guidance. The new question is

how to determine if this masking method is sufficient for unwrapping. Visually it is, but to determine if it

is quantitatively, a comparison of the Zernikes profiles will be made of the residue only method to the

PDV threshold and residue detection.
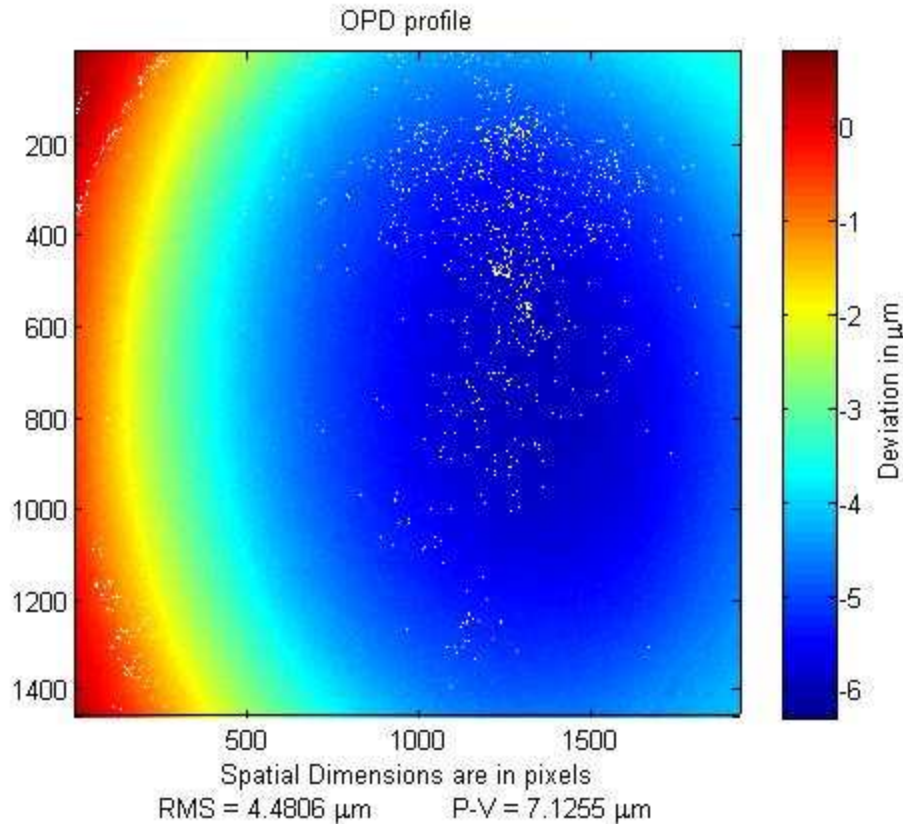
Figure 7.19) PDV Guided Flood Fill Using a Residue Mask

7.6   Comparison of Quality Guided Flood Fill Routines

The ideal way to determine if the unwrapping is done correctly is to measure a known surface,

perform the different unwrapping algorithms, and compare the result to the known data. The

comparison that is about to be shown was done to convince the user that only residue detection, rather

than thresholding and detecting, was necessary in order to simplify the code that needed to be added to

the previous LOCOH GUI. As described at the end of the last section, a Zernike fit of each unwrapping

routine was taken and the simulated surface between the Zernikes were compared. As a reference, it

was assumed that using a PDV guidance, PDV threshold masking, and Residue detection unwrapping

method would produce an accurate surface measurement.

With only a residue mask, the profile was unwrapped two different times where the first

unwrapping used a visibility guidance, and the second used a PDV quality guidance. Afterwards a Zernike

fit using the first 30 Zernikes was performed and the fitted profiles are shown in Figure 7.20.
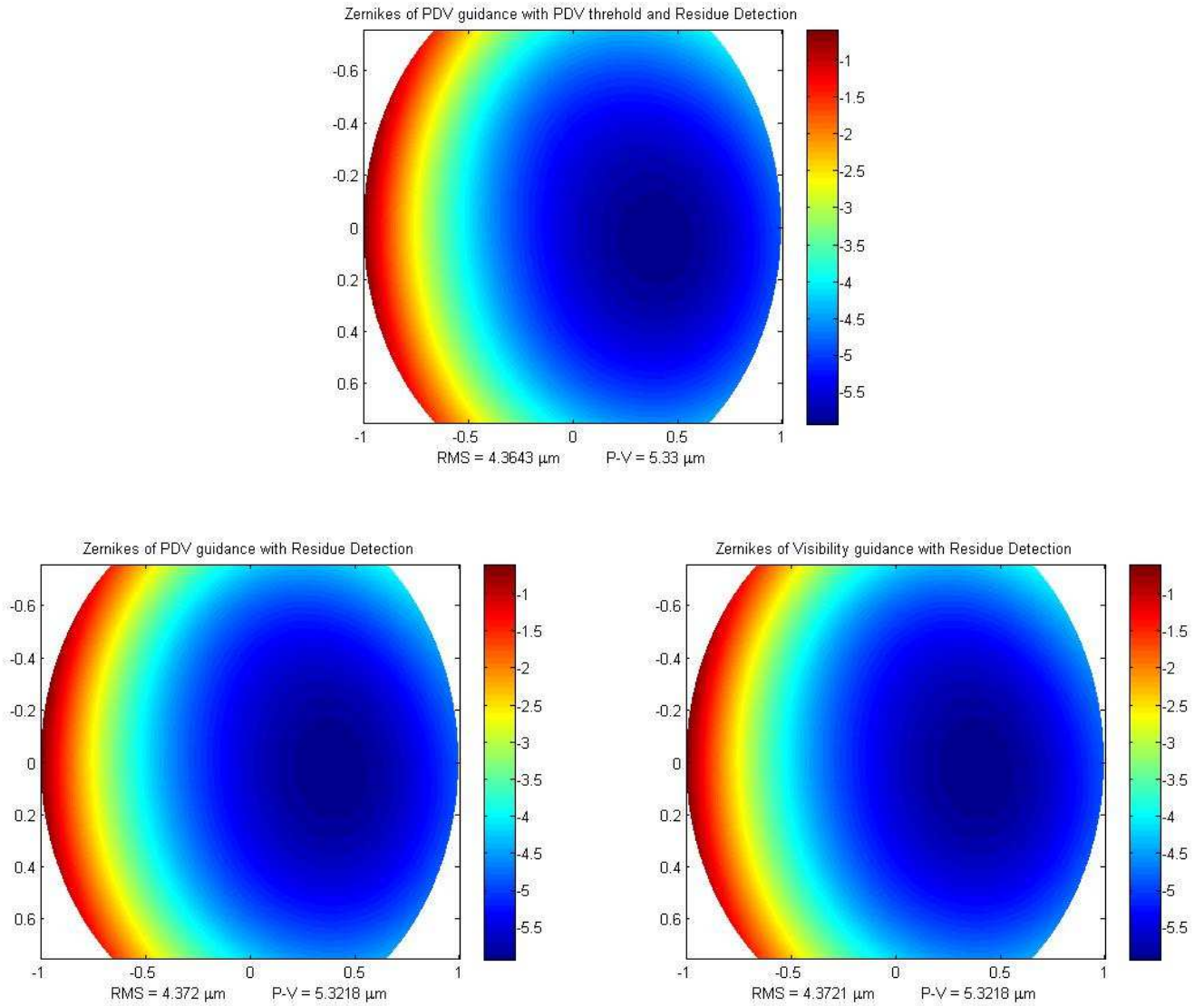
Figure 7.20) Comparison of Zernike Profiles of different unwrapping configurations
Top: PDV guided, PDV threshold and residue masking;
Bottom Left: PDV Guided, residue masking; Bottom Right: Visibility guided, residue masking

As it can be seen, the Zernike fit of the profiles are nearly identical between the three unwrapping configurations. To get a better understanding of the differences between the profiles, the two residue detection only fits were subtracted from the PDV guided, PDV threshold and residue detection profile. These difference maps are shown in Figure 7.21. These profiles are agree to within 1nm peak to valley indicating that there is no optimal quality guidance method. Either PDV or visibility are sufficient though PDV has a slightly better performance by 1nm in the peak to valley error.
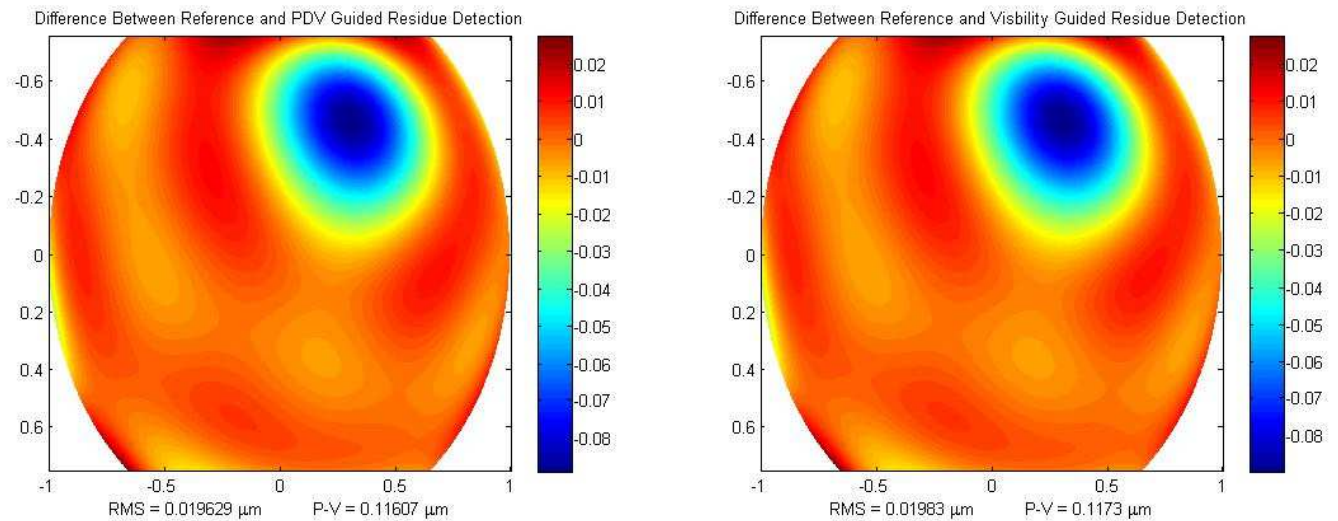
Figure 7.21) Difference between Residue Only Detection and Thresholding with Residue Detection

Detecting only residues, rather than thresholding and detecting residues, does produce a different Zernike representation of the surface profile; however, the RMS error between the residue only detection and thresholding is on the order of 20 nm. The peak to valley error between the two is around 115 nm. Thus, for quick captures, it would seem that only residue detection is sufficient for unwrapping. Again, the only way to know for sure is to measure a calibration surface and compare the measured results to the known profile.

8   New System Results

With both mechanical and software improvements implemented on the initial system, a new set of

verification data was necessary to ensure that the interferometer was performing as desired and that an

improvement was made from the initial design. The verification data taken include multiple repeatability

measurements, a comparison of the different mounting ring performances, a comparison of measured

data to a known surface, a transmissive wave front comparison with CLOVER, and last, a comparison to

previously measured contact lenses. Each of these processes will be discussed in detail in the following

sections.

8.1   Repeatability –Vibration Analysis

The first major test performed on the system was to ensure that the contact does not shift greatly

while be translated due to vibrations from the translation stage. As discussed in section 5.5.2, the

previous mounting scheme did not rigidly hold the contact lens in place during the measurements. One

of the ideas behind inverting the optical layout was to correct this problem by keeping the contact lens

more stable. If the contact lens is indeed more stable, multiple measurements of the surfaces without

removing the contact lens should yield the same result. To test this, a commercial Etafilicon-A lens was

chosen with a reported optical power of 3.5 Diopters. The contact lens had a base curvature of 8.5mm.

Four complete measurements were taken where one complete measurement includes both

cat's eye measurements and both confocal measurements. After one complete measurement was

taken, the lens would be returned to the starting cat's eye position for the next complete measurement

to be taken. No translation was performed on the surfaces to account for decenter errors, so ideally, all

results should be the same. The first set of comparison data is on the posterior surface. Figure 8.1 shows

the measured profiles and Table 8-1 shows the statistics of the four measured profiles. The %

repeatability value reported is given as

$$\% \; Repeatability = 100 \left(1 - \frac{Standard \; Deviation}{mean} \right) \qquad (8.1.1)$$

Table 8-1) Statistics of Posterior Surface - 3 Zernikes Removed, Not Removed from the Mount

	Mean	Standard Deviation	% Repeatability
Radius (mm)	8.4195	0.0064	99.9239
RMS (μm)	0.6615	0.0175	97.3572
Peak to Valley (μm)	4.7202	0.4529	90.4059
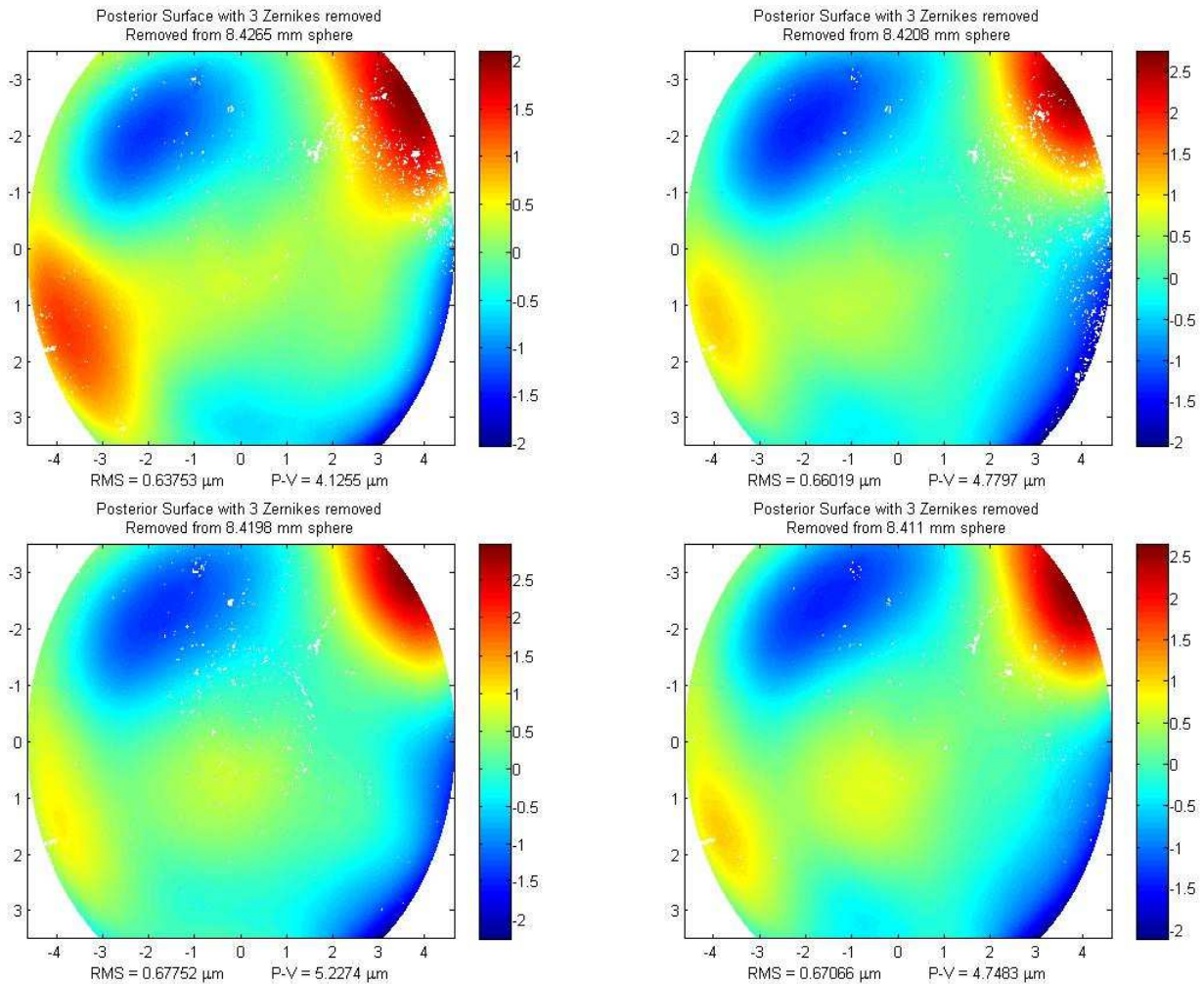
Figure 8.1) Comparison of Posterior Surface - 3 Zernikes Removed, Not Removed from the Mount

To see the high frequency errors, the data also had 15 Zernikes removed. These results are shown

in Table 8-2 and Figure 8.2.

Table 8-2) Statistics of Posterior Surface - 15 Zernikes Removed, Not Removed from the Mount

	Mean	Standard Deviation	% Repeatability
RMS (μm)	0.1825	0.0006	99.6742
Peak to Valley (μm)	2.0503	0.0645	96.8545
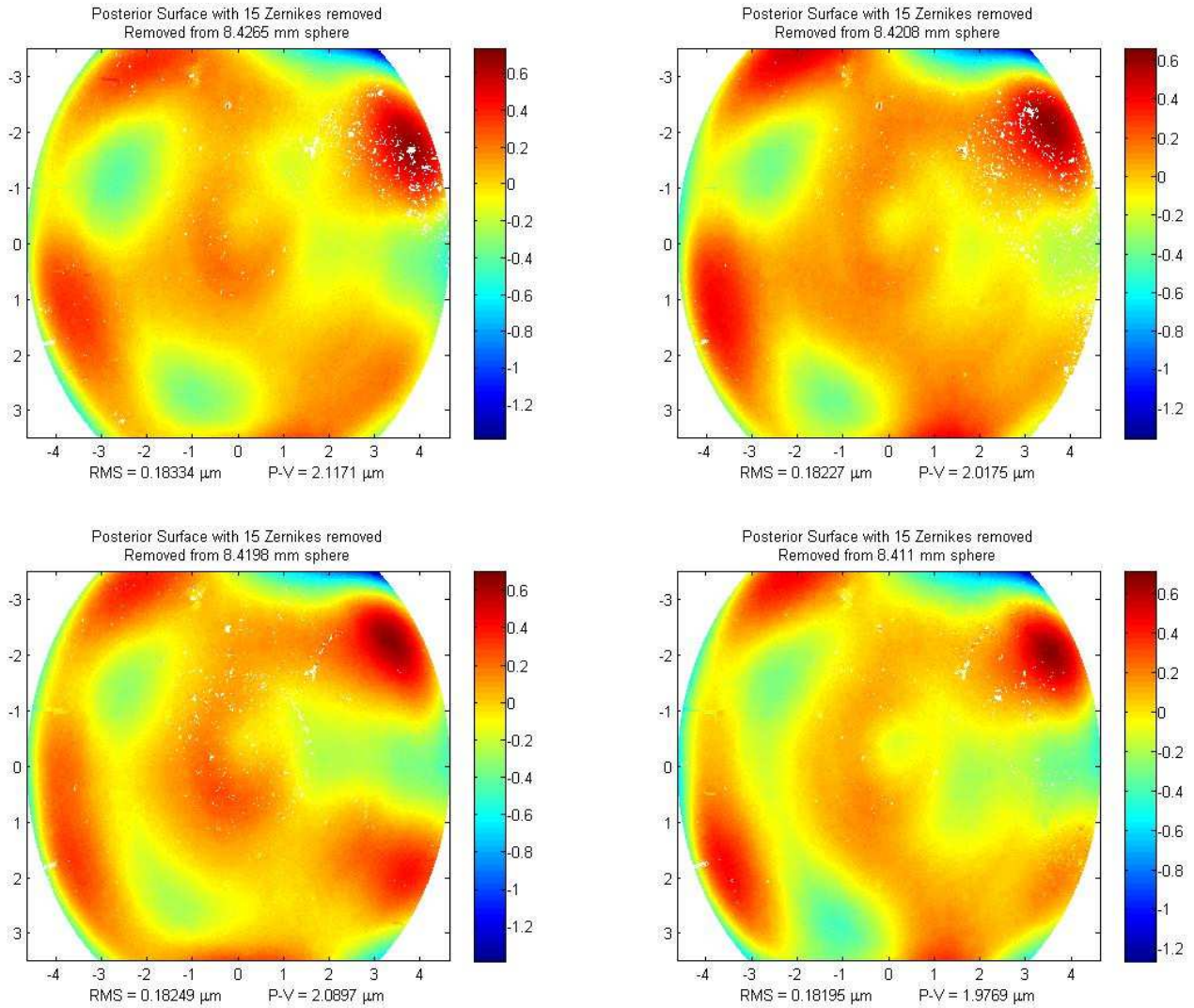
Figure 8.2) Comparison of Posterior Surface - 15 Zernikes Removed, Not Removed from the Mount

Continuing, the anterior surface data with 3 Zernikes removed is shown in Figure 8.3 with the statistical data shown in Table 8-3.

	Mean	Standard Deviation	% Repeatability
Radius (mm)	7.9098	0.0137	99.8273
RMS (μm)	0.5146	0.0285	94.4543
Peak to Valley (μm)	3.0818	0.1233	95.9999
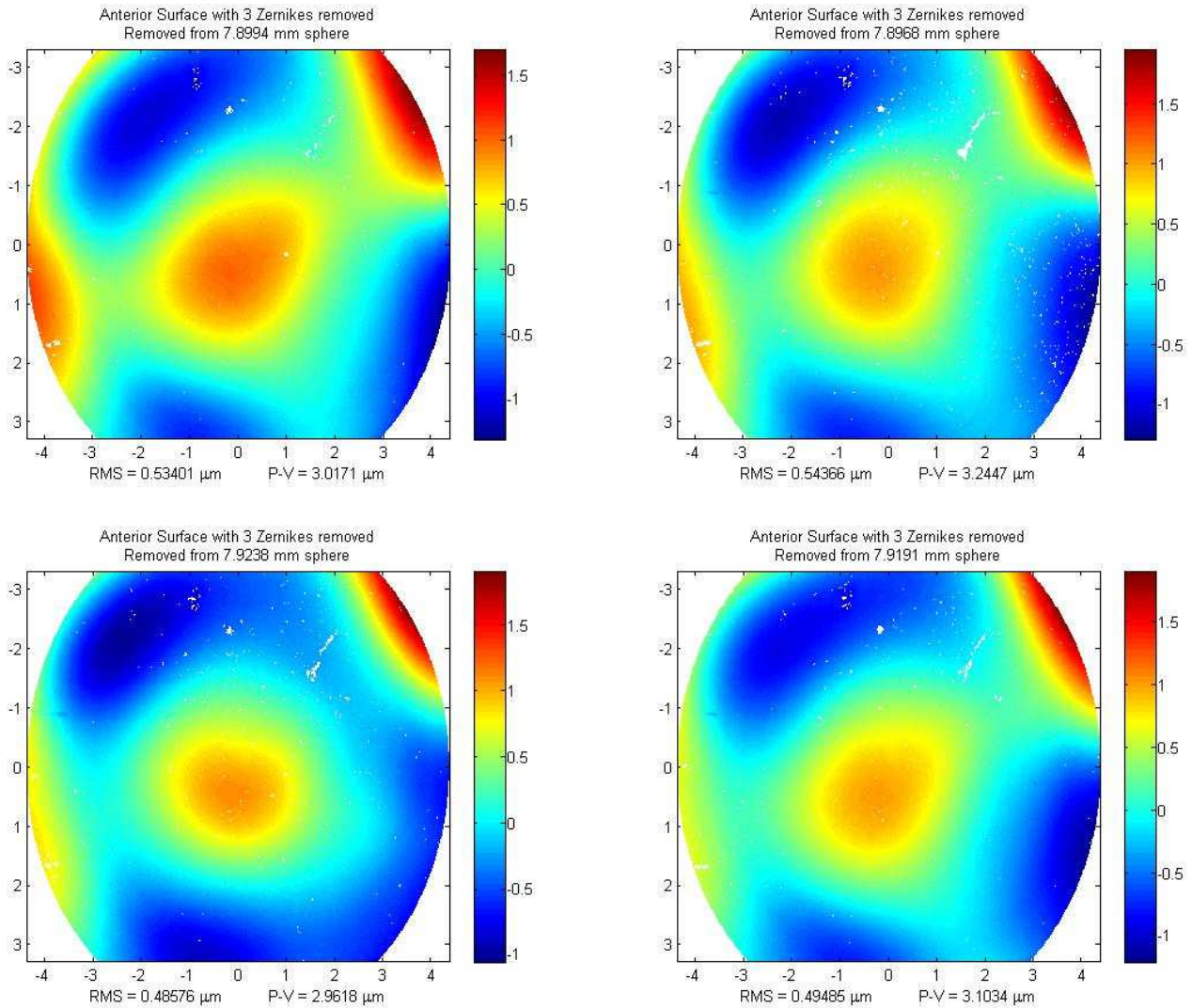
Figure 8.3) Comparison of Anterior Surface - 3 Zernikes Removed, Not Removed from the Mount

As with the previous results, the high frequency error of the anterior surface is shown in Figure 8.4 and Table 8-4.

Table 8-4) Statistics of Anterior Surface - 15 Zernikes Removed, Not Removed from the Mount

	Mean	Standard Deviation	% Repeatability
RMS (μm)	0.1555	0.0262	83.1428
Peak to Valley (μm)	1.5960	0.2032	87.2698
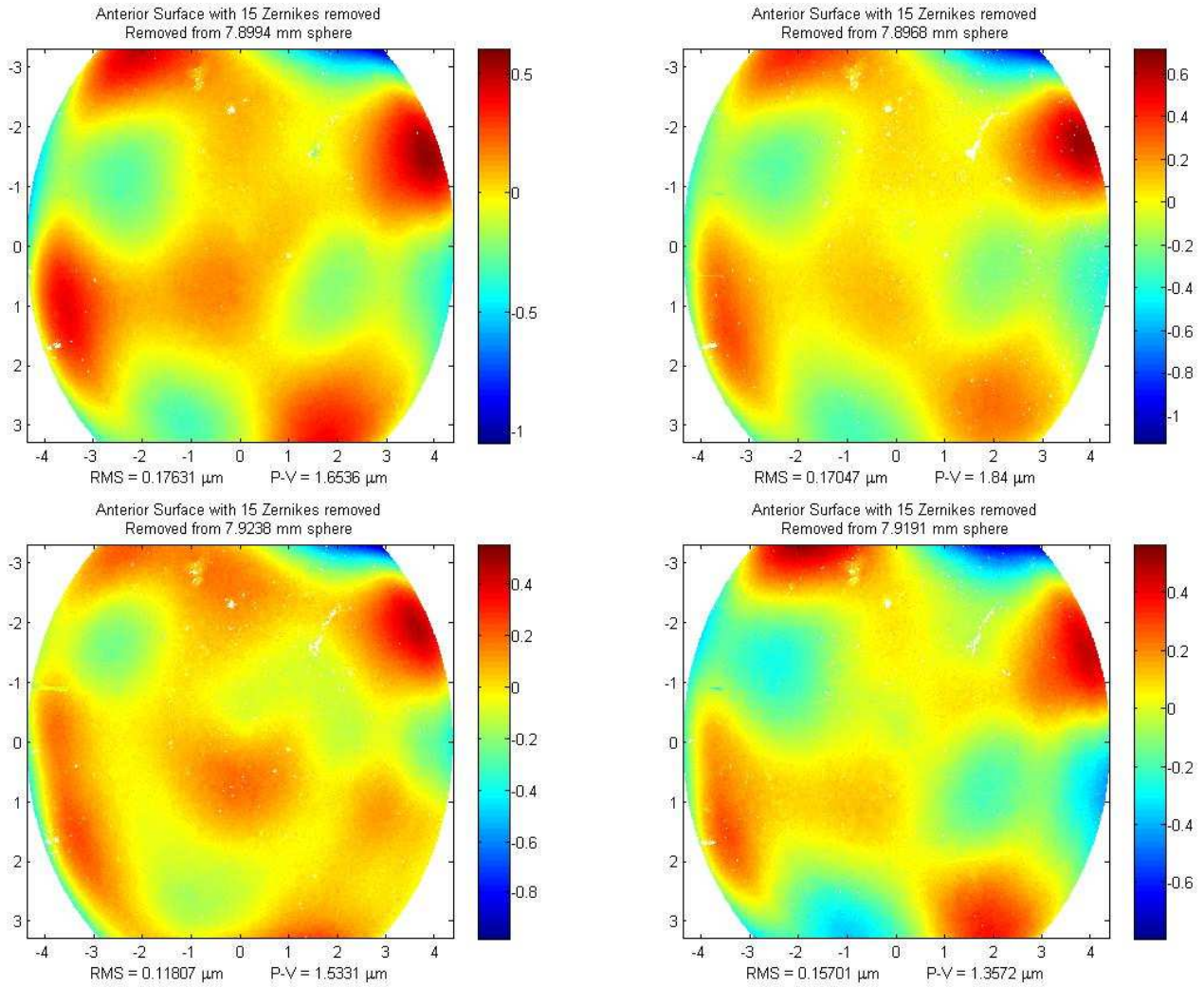
Figure 8.4) Comparison of Anterior Surface - 15 Zernikes Removed, Not shifted

The last data to consider is the thickness profile determined. The profiles and data are shown in Figure 8.5 and Table 8-5.

Table 8-5) Statistics of Thickness Profile - Not Removed from the Mount

	Mean	Standard Deviation	% Repeatability
Center Thickness (μm)	193.0439	15.6537	91.8911
Peak to Valley (μm)	0.1125	0.0066	94.0919
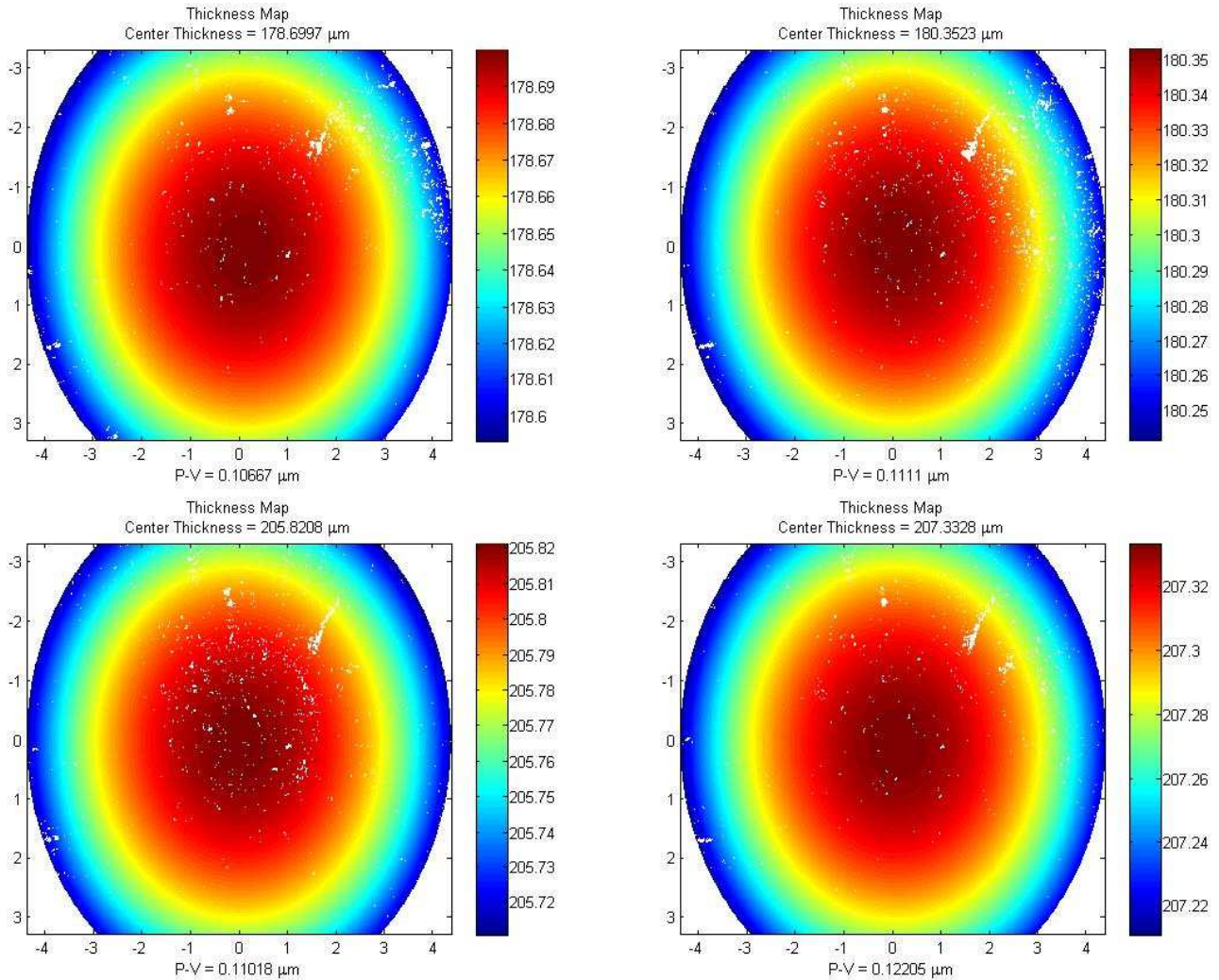
Figure 8.5) Comparison of Thickness Profile - Not shifted

The end results show that RMS data of the surface can be accepted to within 30nm, the peak to valley data can be accepted to within 450nm, and the radius and central thickness measurements to within 15 microns. It should be noted that these particular measurements were taken on the 9mm ring mount.

8.2 Repeatability – Mount Comparison

The next analysis necessary was to understand how repeatable the contact lens measurements were when they were taken in and out of the interferometer. The performance/ experience in this test would also decide which of the ring mounts described in section 6.4 would be optimal to use. All measurements were taken with the same contact lens used from the previous test. After the presentation of the results for each mount, a comparison will be shown which will decide the resolution limit of the parameters measured.

8.2.1 9mm Mount Repeatability

Four complete measurements were taken using the 9mm Contact lens mount; however, the difference between these measurements and the previous was that the contact lens would be completely removed from the interferometer system between the measurements. Also, each measurement was adjusted for decentering errors when the confocal measurements were taken. It should be noted that no consideration was done for ensuring that contact lens orientation remained the same; however, it should be expected that the results RMS and peak to valley errors should be the same since it is over the same area of the surfaces. Just as in the previous section, Figure 8.6 through Figure 8.10 show the 3 Zernike removed, 15 Zernike removed, and thickness profile of the contact lens with Table 8-6 through Table 8-10 showing the statistical data.

Table 8-6) Statistics of Posterior Surface - 3 Zernikes Removed, Removed between Measurements

	Mean	Standard Deviation	% Repeatability
Radius (mm)	8.4370	0.0083	99.9014
RMS (μm)	0.6037	0.0322	94.6733
Peak to Valley (μm)	4.2278	0.2812	93.3479
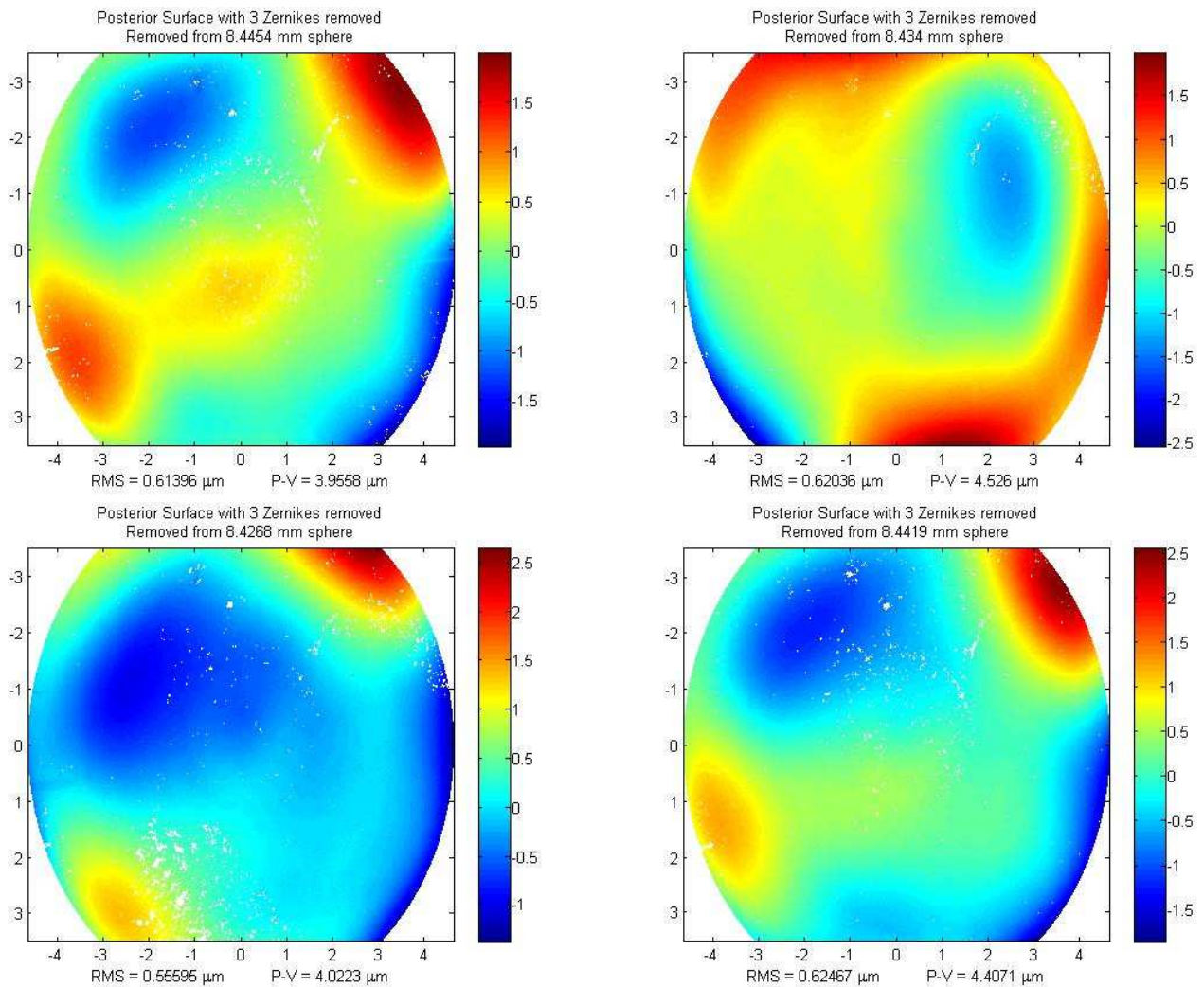
Figure 8.6) Comparison of Posterior Surface - 3 Zernikes Removed, Removed between Measurements

Table 8-7) Statistics of Posterior Surface - 15 Zernikes Removed, Removed between Measurements

	Mean	Standard Deviation	% Repeatability
RMS (μm)	0.1692	0.0141	91.6898
Peak to Valley (μm)	1.7345	0.2872	83.4428
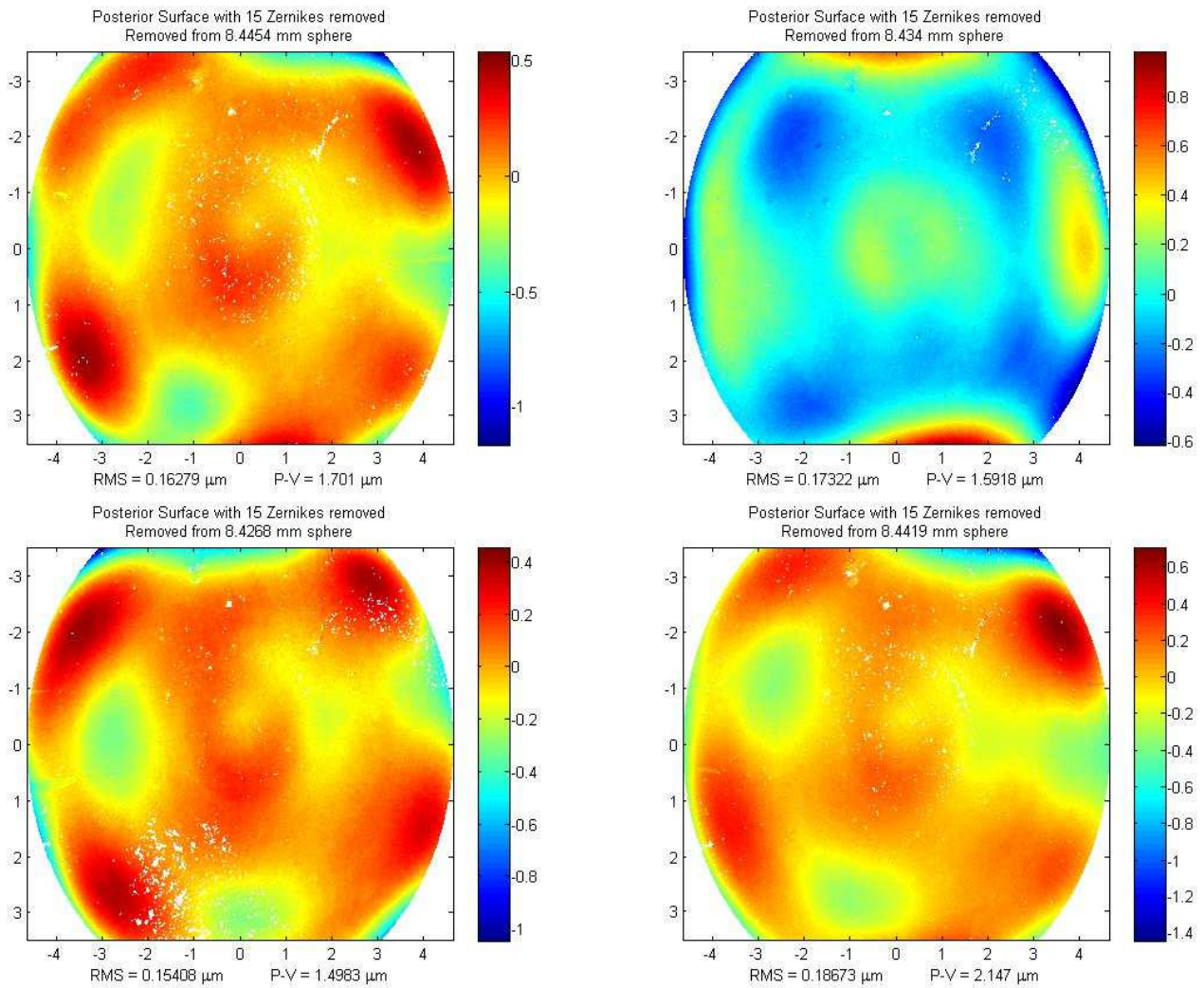
Figure 8.7) Comparison of Posterior Surface - 15 Zernikes Removed, Removed between Measurements

Table 8-8) Statistics of Anterior Surface - 3 Zernikes Removed, Removed between Measurements

	Mean	Standard Deviation	% Repeatability
Radius (mm)	7.9151	0.0135	99.8296
RMS (μm)	0.4709	0.0603	87.1943
Peak to Valley (μm)	3.1527	0.2818	91.0612
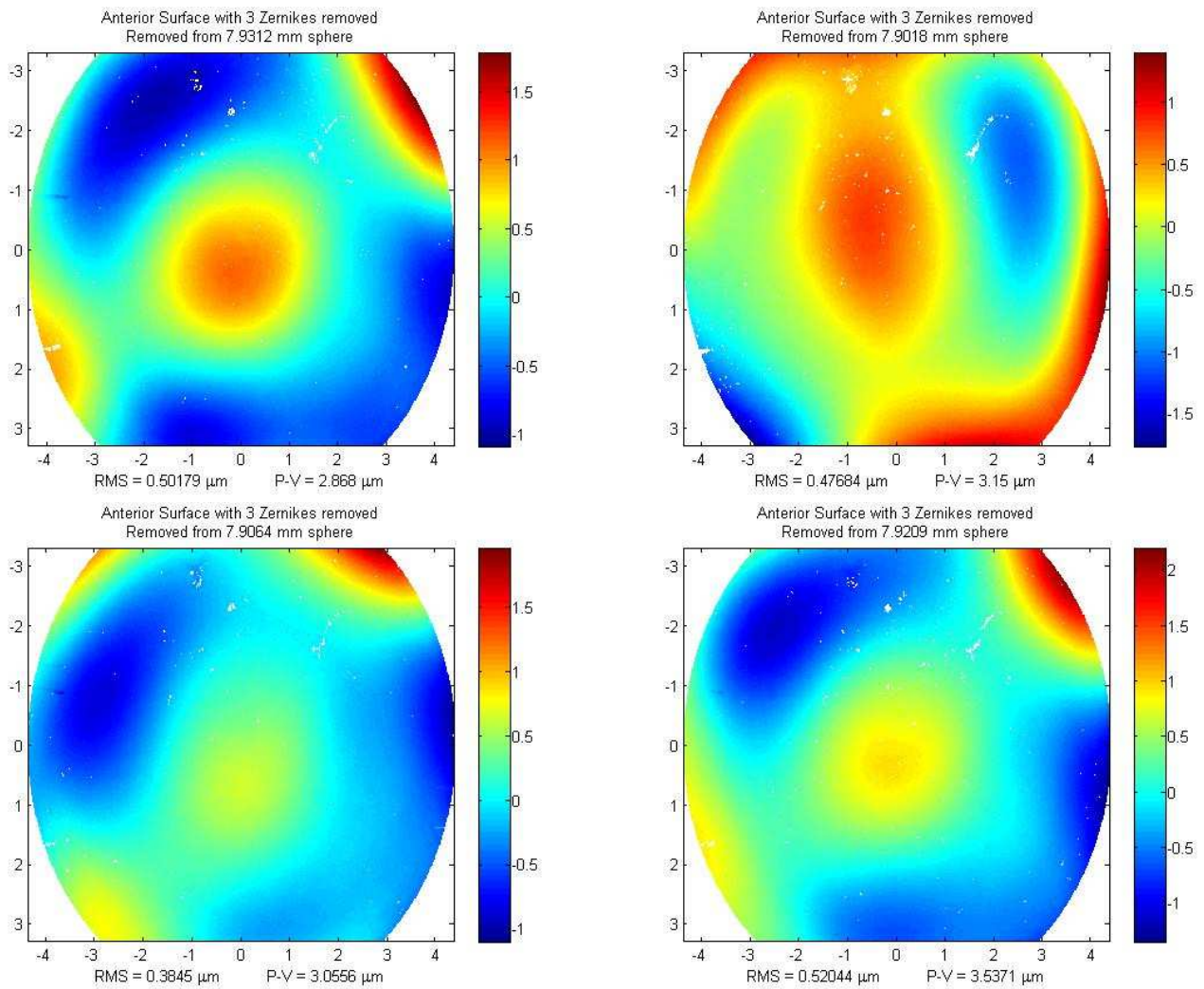
Figure 8.8) Comparison of Anterior Surface - 3 Zernikes Removed, Removed between Measurements

Table 8-9) Statistics of Anterior Surface - 15 Zernikes Removed, Removed between Measurements

	Mean	Standard Deviation	% Repeatability
RMS (μm)	0.1323	0.0108	91.8610
Peak to Valley (μm)	1.4660	0.2280	84.4483
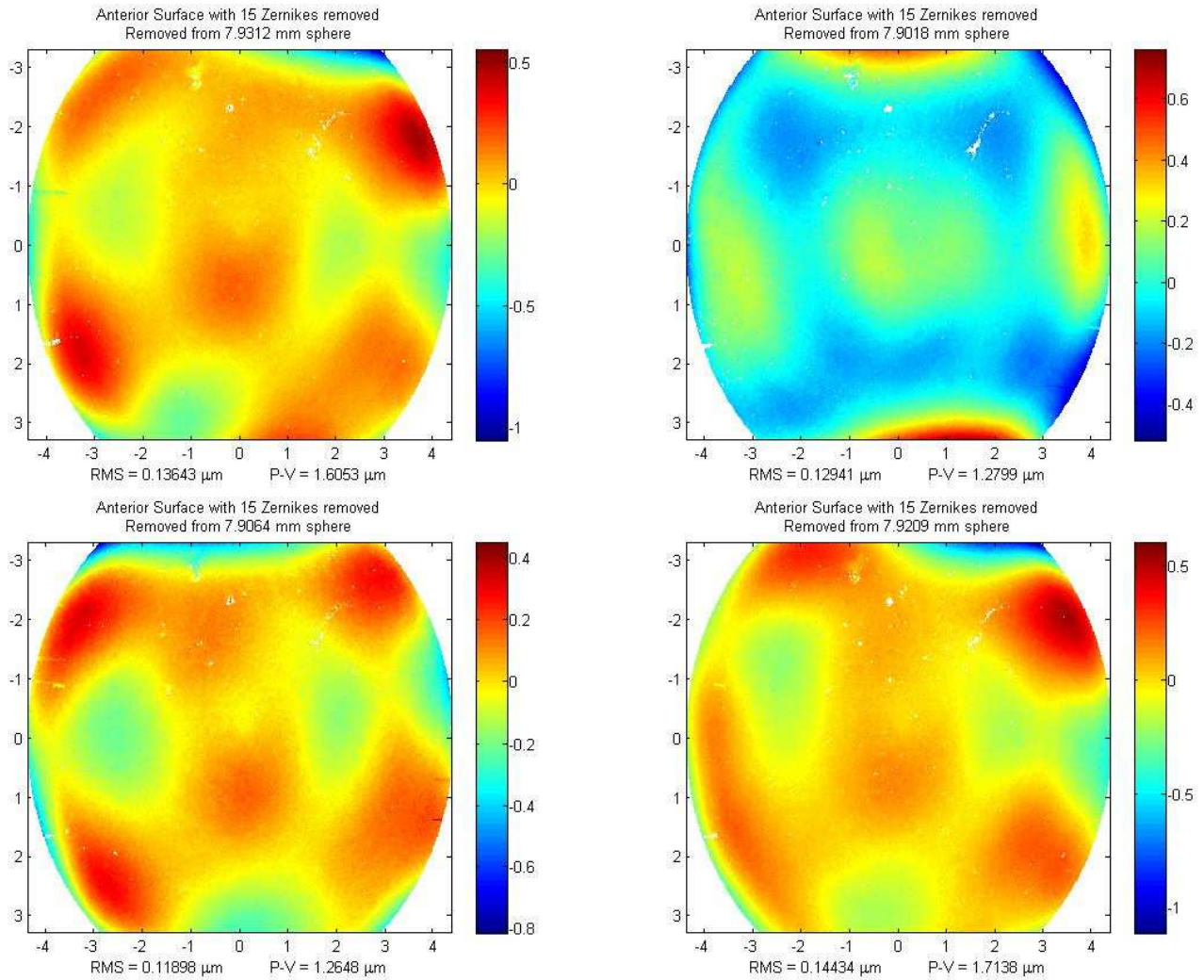
Figure 8.9) Comparison of Anterior Surface - 15 Zernikes Removed, Removed between Measurements

Table 8-10) Statistics of Thickness Profile - Removed between Measurements

	Mean	**Standard Deviation**	**% Repeatability**
Central Thickness (μm)	183.2430	5.4364	97.0332
Peak to Valley (μm)	0.1082	0.0075	93.0868
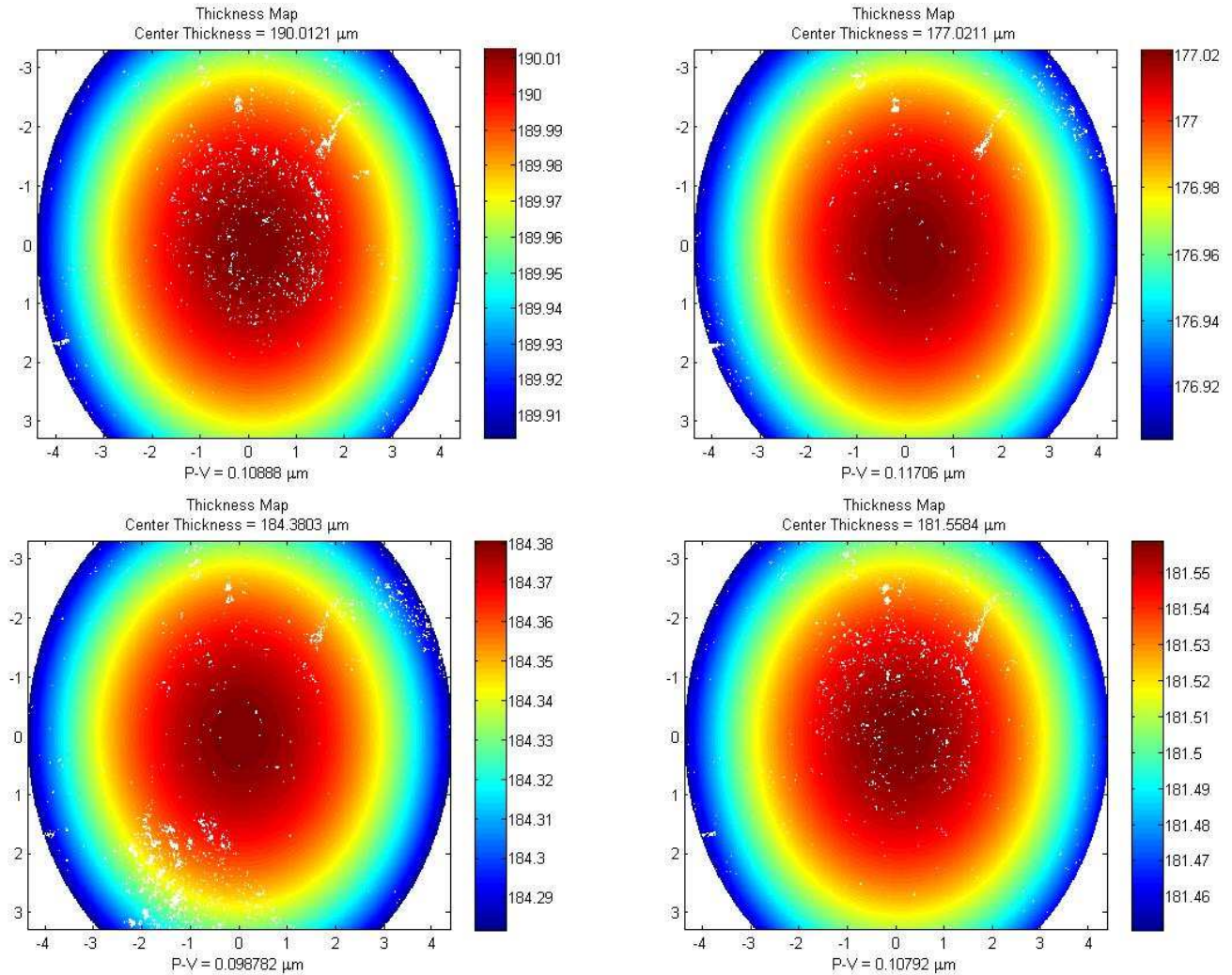
Figure 8.10) Comparison of Thickness Profile - Removed between Measurements

The end result of the 9mm contact lens mount test showed that the RMS surface measurements could be taken to within 20nm, the peak to valley measurements could be accepted to within 300 microns, the radius measurements to within 15 microns, and the central thickness measurement to within 10 microns.

8.2.2 10.5 mm Mount Repeatability

Running the same type of tests on the 10.5 mm contact lens mount yields the profiles and statistics shown in Figure 8.11 through Figure 8.15 and Table 8-11 through Table 8-15.

Table 8-11) Statistics of Posterior Surface - 3 Zernikes Removed, Removed between Measurements, 10.5 mm mount

	Mean	Standard Deviation	% Repeatability
Radius (mm)	8.3812	0.0335	99.6005
RMS (μm)	0.6259	0.1574	74.8580
Peak to Valley (μm)	4.0068	1.5734	60.7331

Figure 8.11) Comparison of Posterior Surface - 3 Zernikes Removed, Removed between Measurements, 10.5mm Mount

Table 8-12) Statistics of Posterior Surface - 15 Zernikes Removed, Removed between Measurements, 10.5 mm mount

	Mean	Standard Deviation	% Repeatability
RMS (μm)	0.1819	0.0252	86.1518
Peak to Valley (μm)	1.6206	0.1586	90.2144

Figure 8.12) Comparison of Posterior Surface - 15 Zernikes Removed, Removed between Measurements, 10.5 mm mount

Table 8-13) Statistics of Anterior Surface - 3 Zernikes Removed, Removed between Measurements, 10.5mm mount

	Mean	Standard Deviation	% Repeatability
Radius (mm)	7.8554	0.0406	99.4834
RMS (μm)	0.3989	0.1319	66.9330
Peak to Valley (μm)	2.6648	1.3057	51.0018

Figure 8.13) Comparison of Anterior Surface - 3 Zernikes Removed, Removed between Measurements, 10.5 mm mount

Table 8-14) Statistics of Anterior Surface - 15 Zernikes Removed, Removed between Measurements, 10.5 mm mount

	Mean	Standard Deviation	% Repeatability
RMS (μm)	0.1386	0.0123	91.1039
Peak to Valley (μm)	1.2925	0.0929	92.8091

Figure 8.14) Comparison of Anterior Surface - 15 Zernikes Removed, Removed between Measurements, 10.5 mm mount

Table 8-15) Statistics of Thickness Profile - Removed between Measurements, 10.5 mm mount

	Mean	Standard Deviation	% Repeatability
Central Thickness (μm)	183.0930	21.3891	88.3179
Peak to Valley (μm)	0.1128	0.0060	94.6688
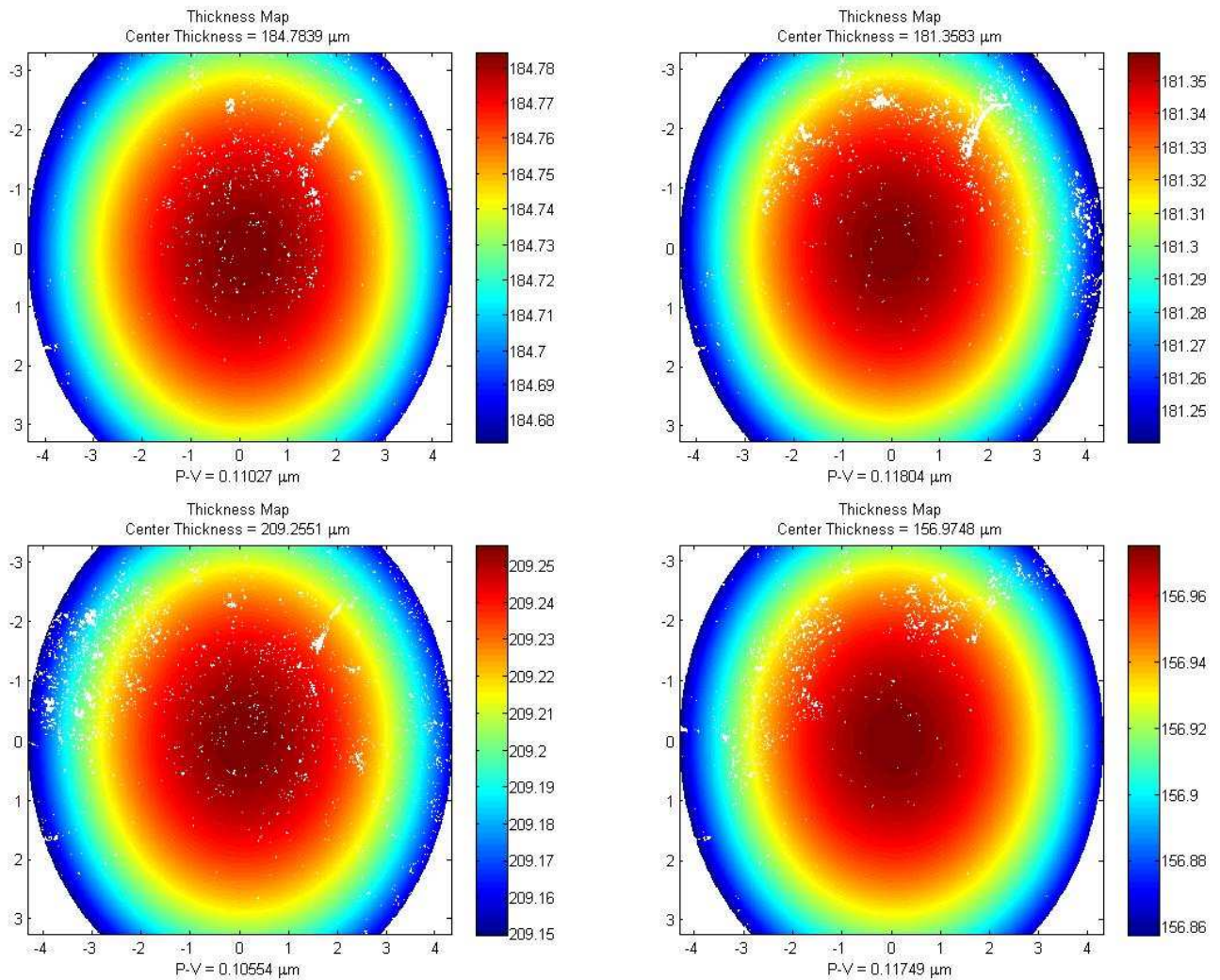
Figure 8.15) Comparison of Thickness Profile - Removed between Measurements, 10.5 mm mount

Thus the resolution limits found for the 10.5 mm mount were around 130 nm RMS, 1.5 microns peak to valley, 40 microns on the radius, and around 21 microns on the central thickness. Of the data set, one measurement seemed to skew the data dramatically, and if that particular set was not included in the analysis, the new values would be 41 nm RMS, 140 nm peak to valley, 45 microns on the radius, and 26 microns on the central thickness. Though the RMS and peak to valley results are better when throwing away one of the measurements, they still have a lower performance than the 9 mm mount.

8.2.3   13mm Mount Repeatability

For the 13mm mount test, it was found that it was much harder to get the contact lens in place on the mount. Often it would slip through the mount which could possibly damage it if it would snag on the beam dump below. Also, the contact lens was very unstable during the translation between cat's eye and confocal positions which is also not ideal for industrialization. The shifting seen was very similar to when the contact lens was mounted concave down in the initial build of LOCOH. Because it took more care and time in setting up the contact lens measurements, only 3 measurements were taken since it was decided early on that this mount would not be ideal for typical use.

As with the previous mounting tests, the data collected is shown in Figure 8.16 through Figure 8.20 with the statistics in Table 8-16 through Table 8-20.

Table 8-16) Statistics of Posterior Surface - 3 Zernikes Removed, Removed between Measurements, 13 mm mount

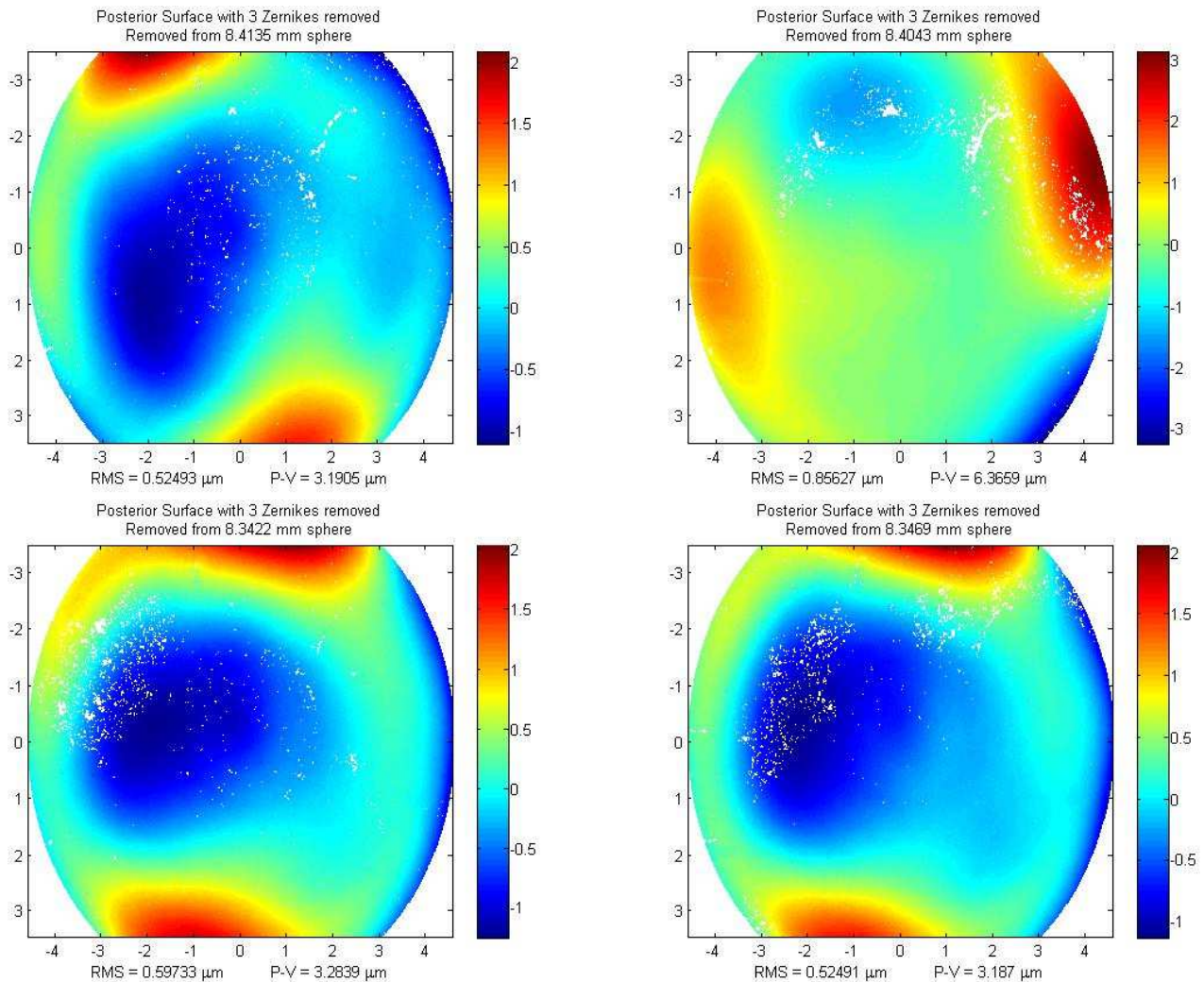|	Mean	Standard Deviation	% Repeatability
Radius (mm)	8.2993	0.0060	99.9277
RMS (μm)	0.7485	0.1291	82.7469
Peak to Valley (μm)	4.4496	0.5614	87.3837
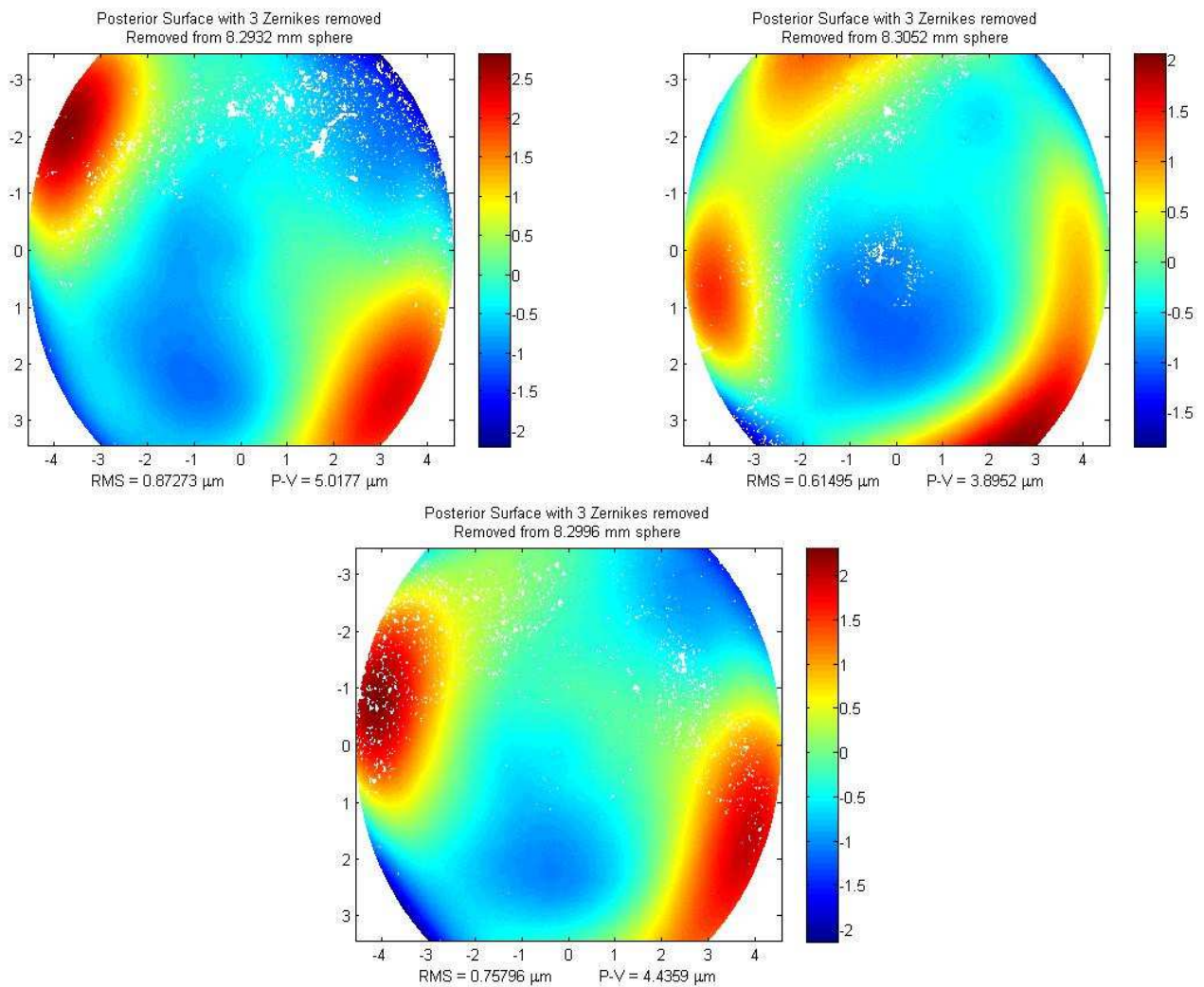
Figure 8.16) Comparison of Posterior Surface - 3 Zernikes Removed, Removed between Measurements, 13 mm Mount

Table 8-17) Statistics of Posterior Surface - 15 Zernikes Removed, Removed between Measurements, 13 mm mount

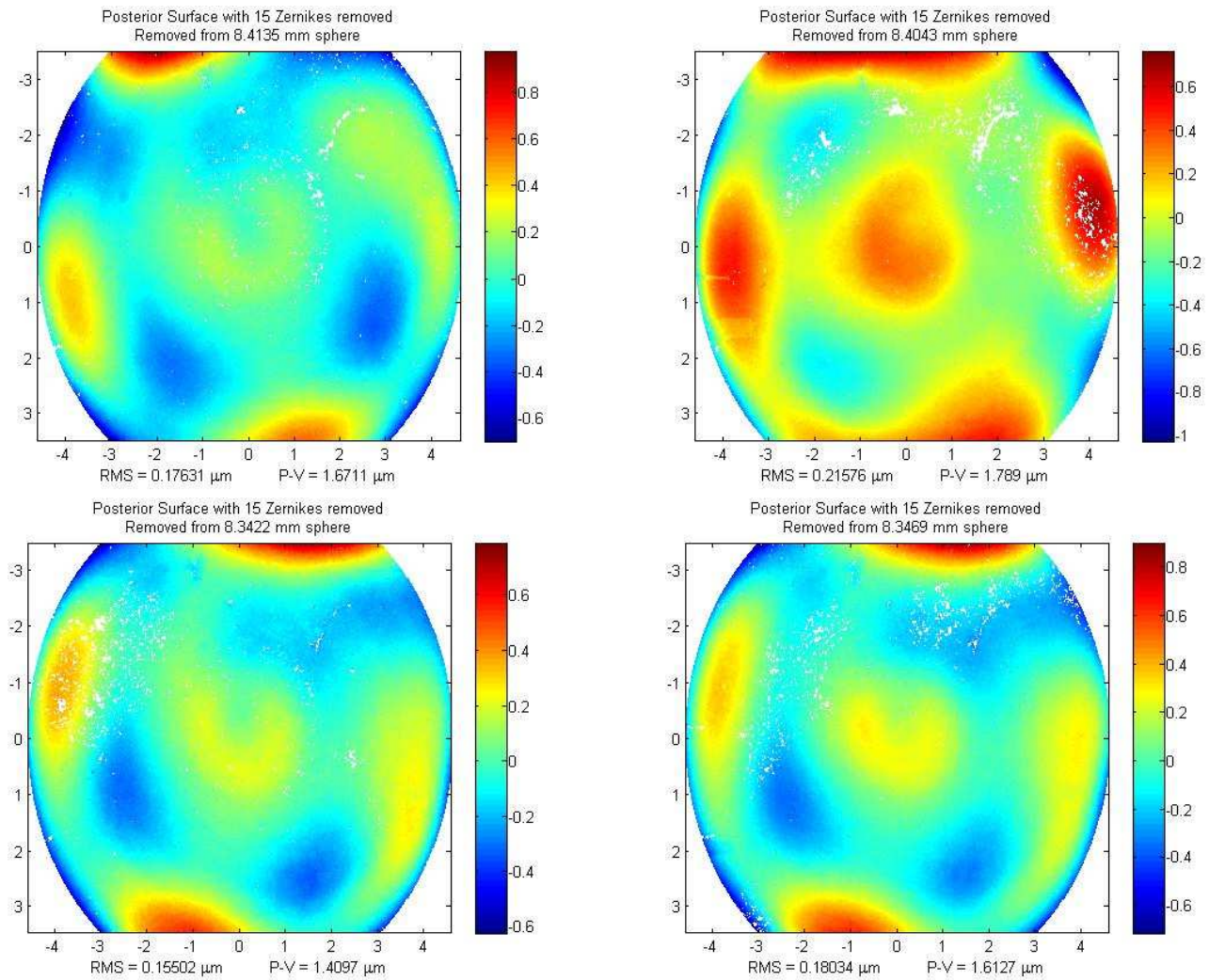|	Mean	Standard Deviation	% Repeatability
RMS (μm)	0.2253	0.0194	91.3966
Peak to Valley (μm)	1.8514	0.0662	96.4265
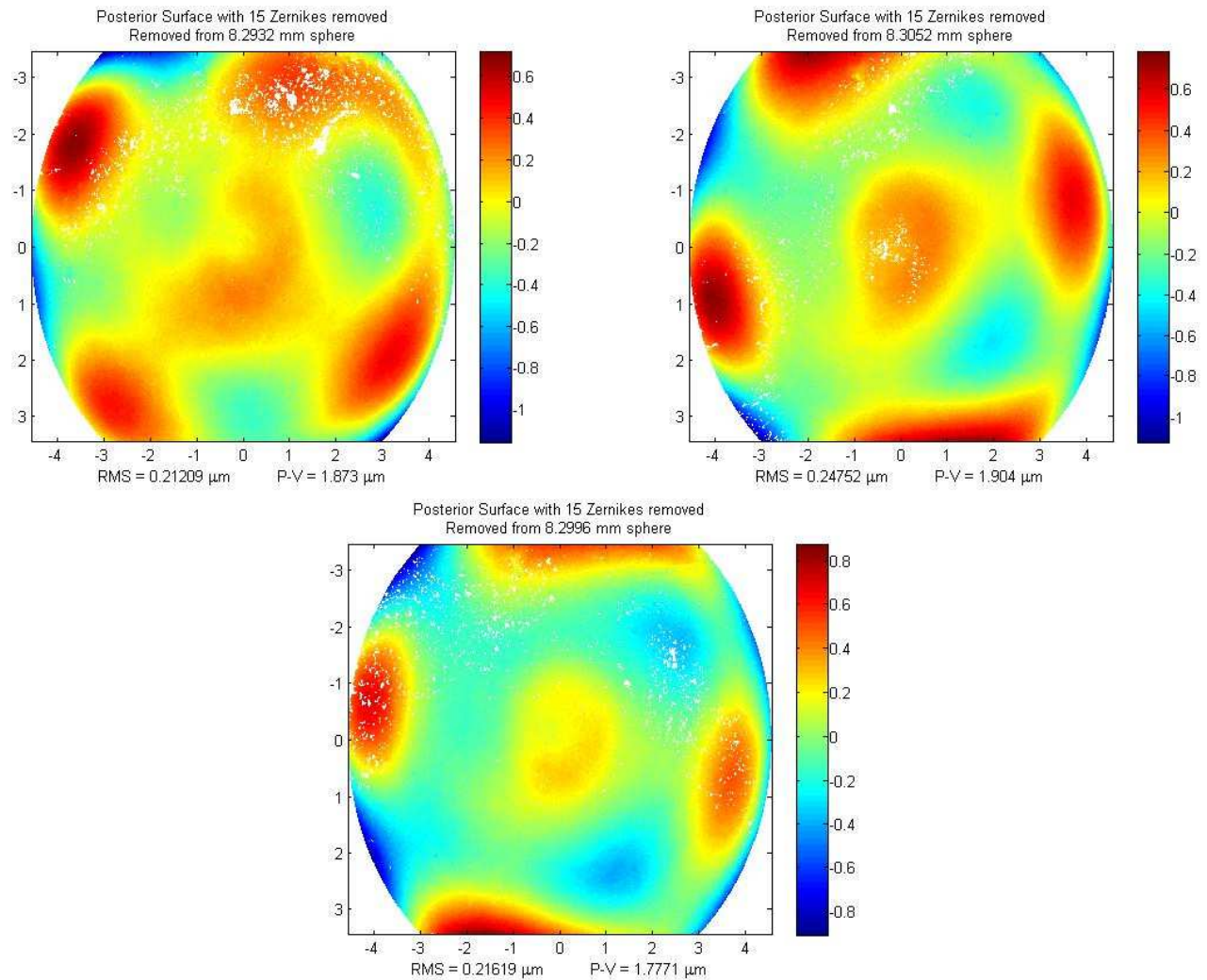
Figure 8.17) Comparison of Posterior Surface - 15 Zernikes Removed, Removed between Measurements, 13 mm mount

Table 8-18) Statistics of Anterior Surface - 3 Zernikes Removed, Removed between Measurements, 13 mm mount

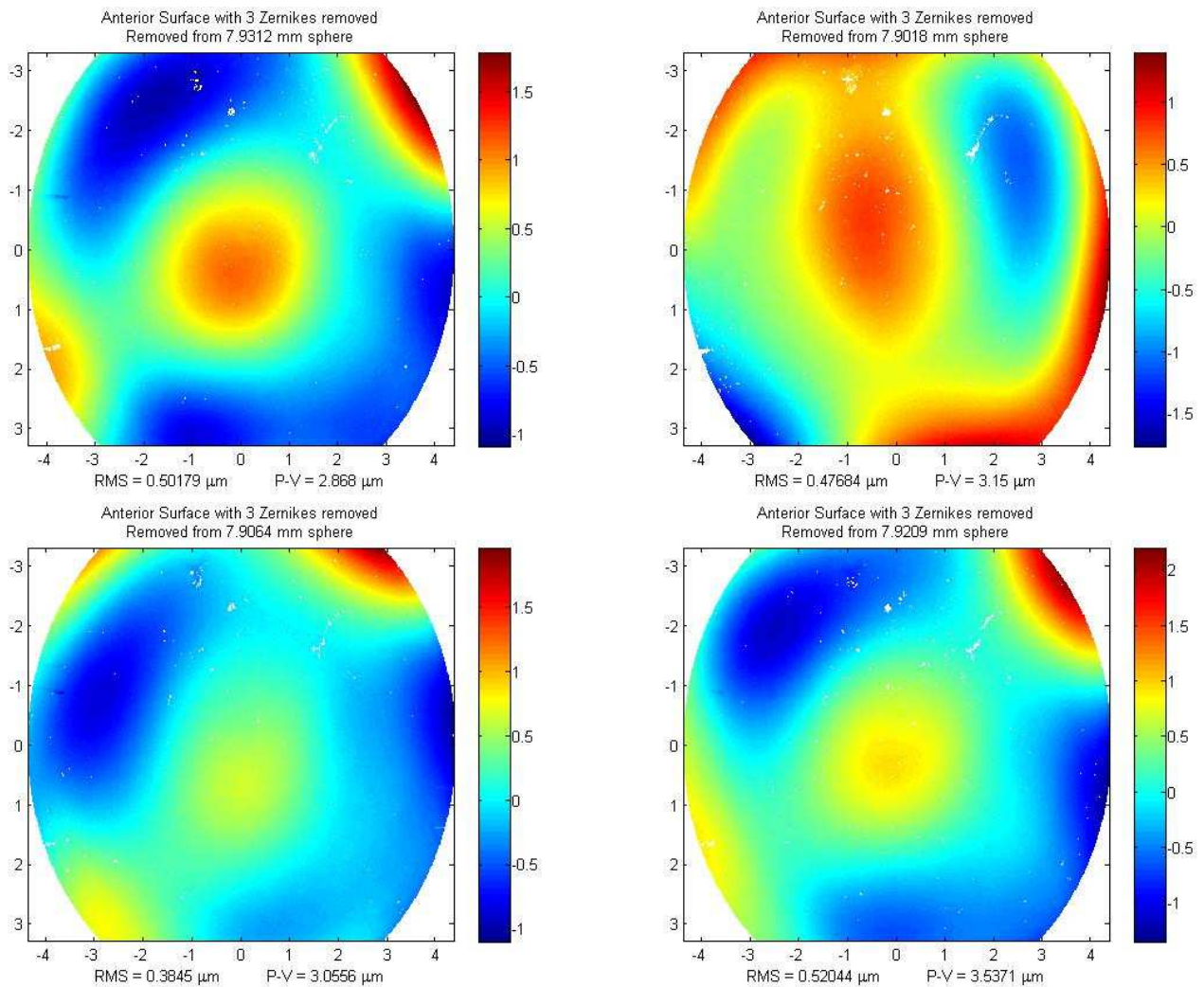|	Mean	Standard Deviation	% Repeatability
Radius (mm)	7.7786	0.0084	99.8920
RMS (μm)	0.5255	0.1185	77.4566
Peak to Valley (μm)	3.1780	0.3537	88.8710
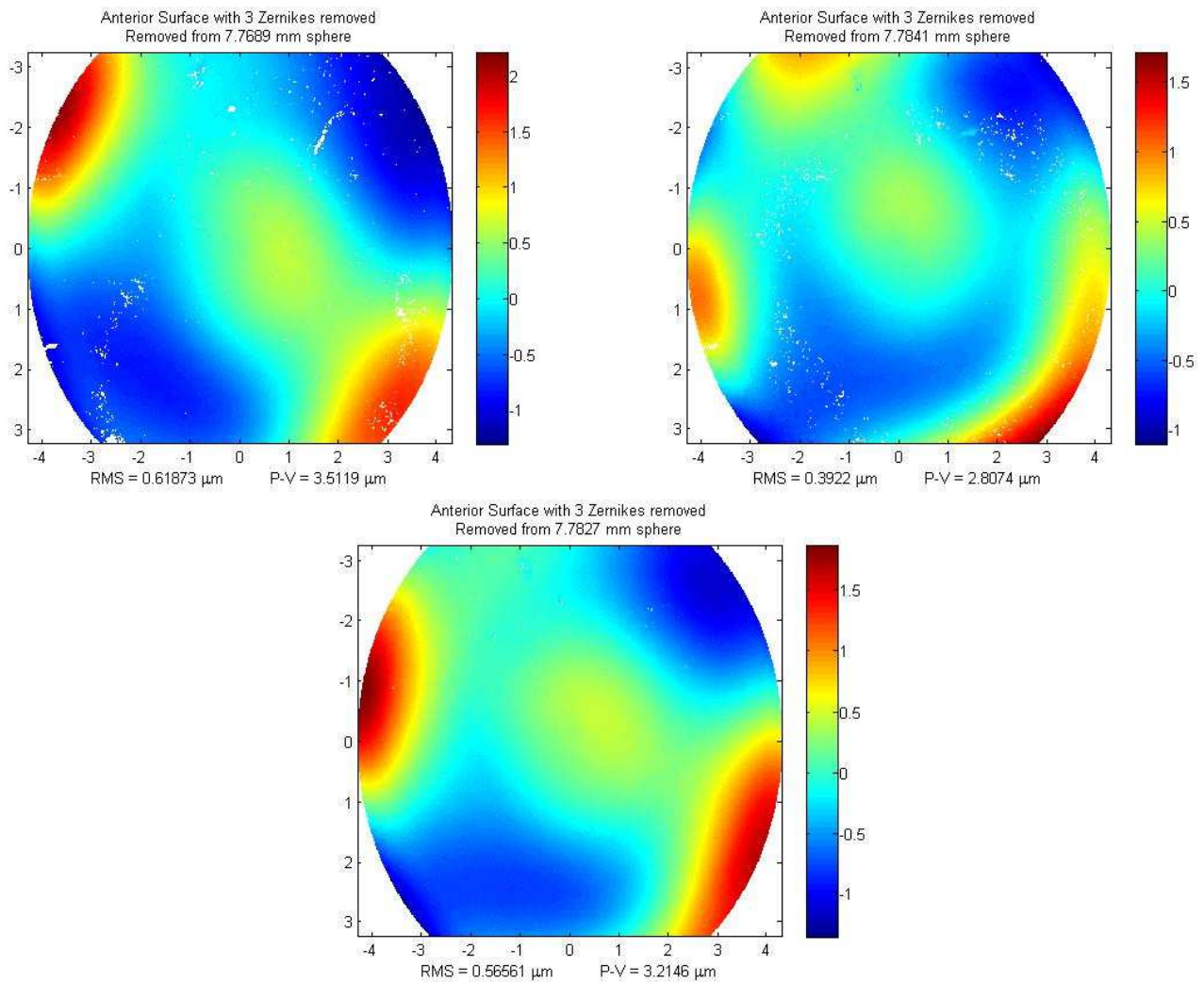
Figure 8.18) Comparison of Anterior Surface - 3 Zernikes Removed, Removed between Measurements, 13 mm mount

Table 8-19) Statistics of Anterior Surface - 15 Zernikes Removed, Removed between Measurements, 13 mm mount

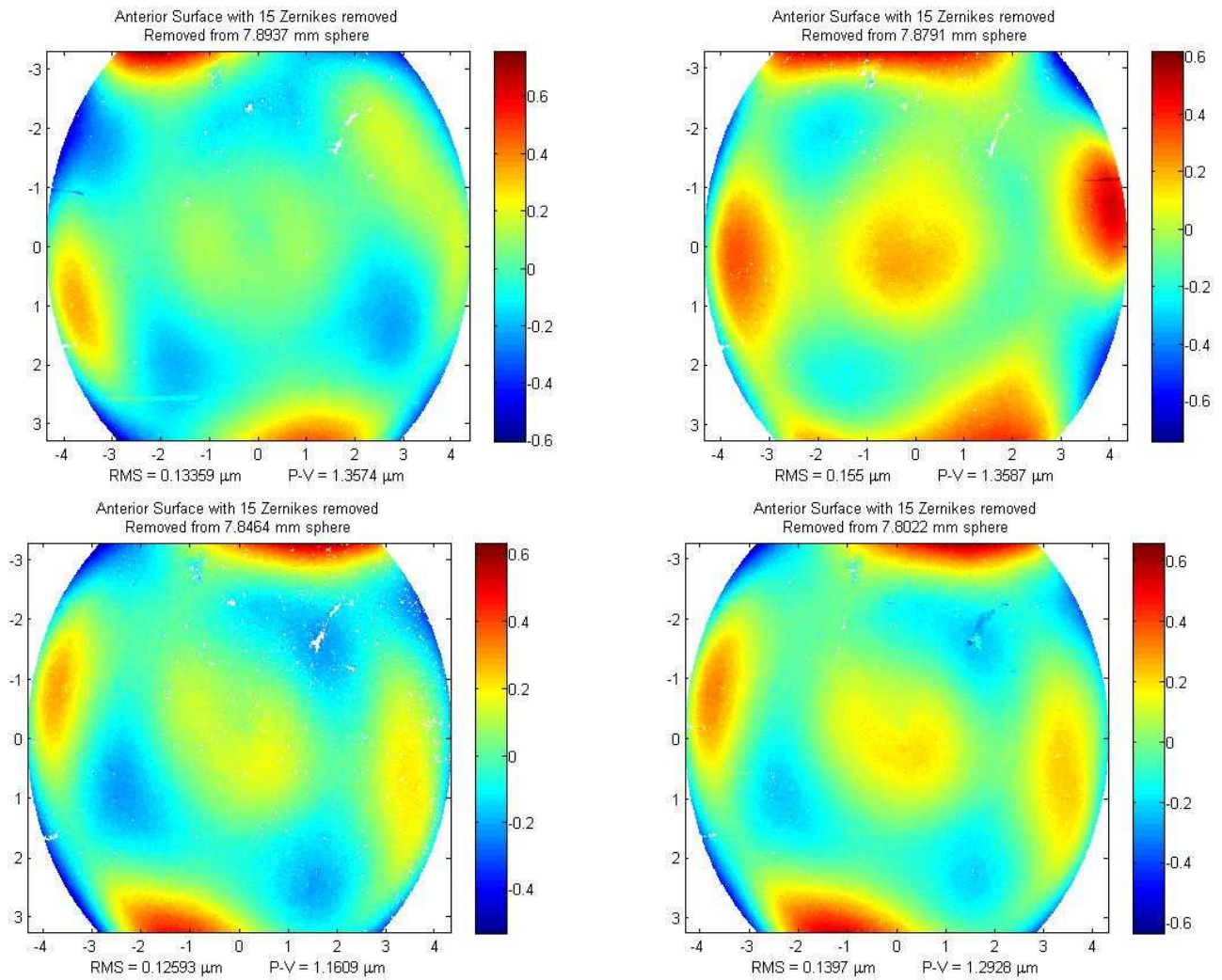|	Mean	Standard Deviation	% Repeatability
RMS (μm)	0.1740	0.0214	87.7192
Peak to Valley (μm)	1.5746	0.0753	95.2206
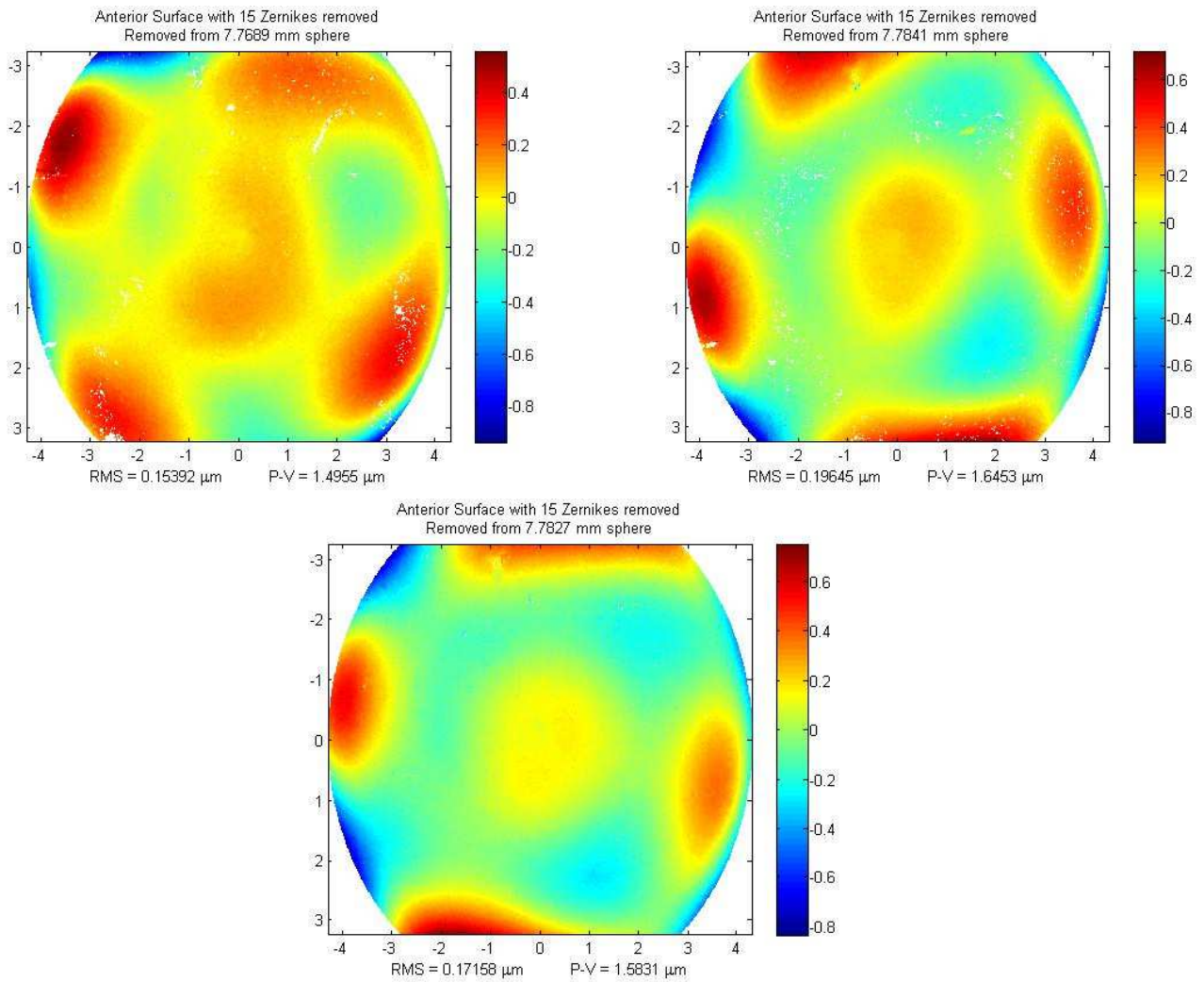
Figure 8.19) Comparison of Anterior Surface - 15 Zernikes Removed, Removed between Measurements, 13 mm mount

Table 8-20) Statistics of Thickness Profile - Removed between Measurements, 13 mm mount

	Mean	Standard Deviation	% Repeatability
Central Thickness (μm)	177.8236	5.7360	96.7743
Peak to Valley (μm)	0.1077	0.0011	98.9549
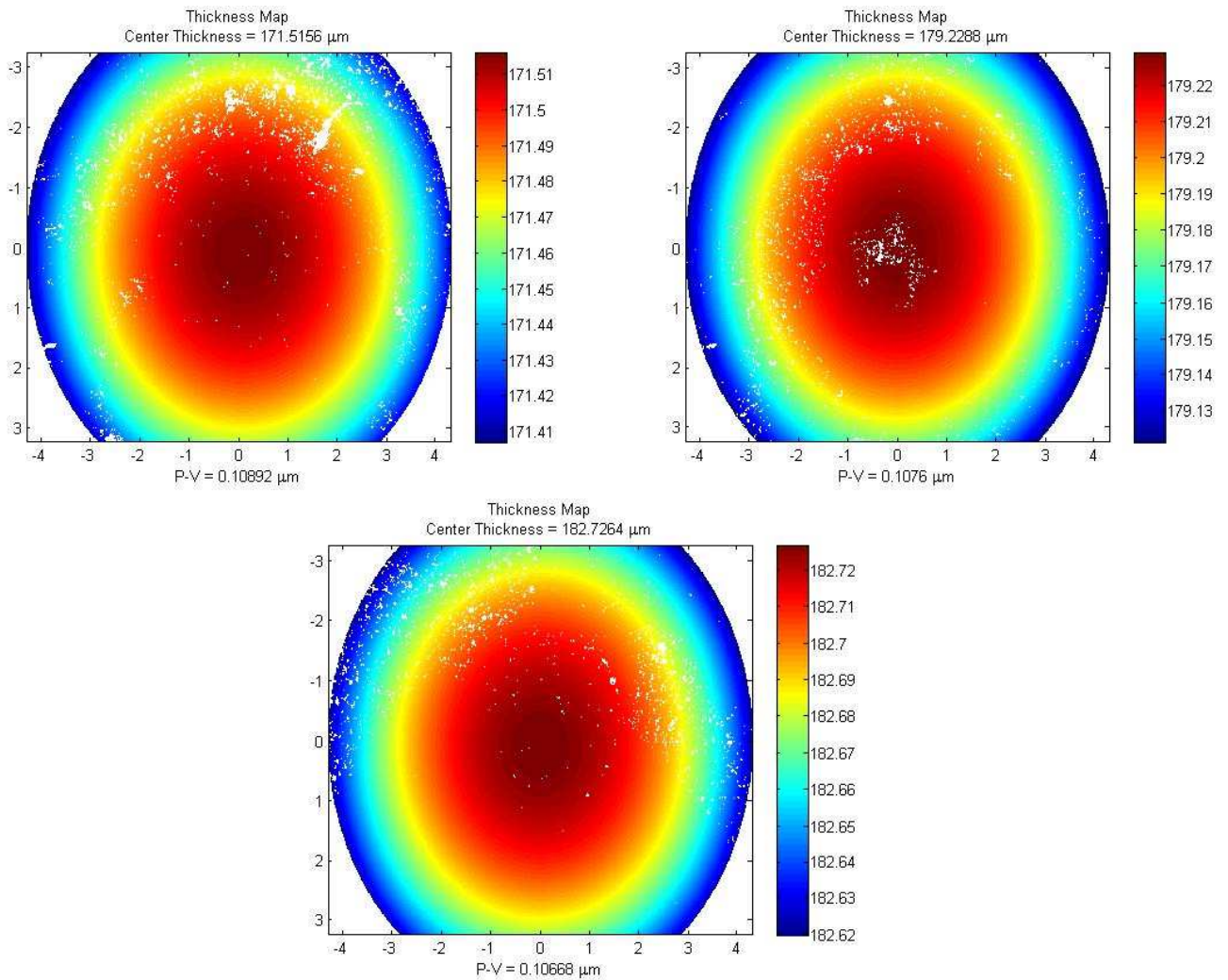
Figure 8.20) Comparison of Thickness Profile - Removed between Measurements, 10.5 mm mount

With the results gathered using the 13 mm mount, it was shown that there is an error of about

130nm RMS, 560nm peak to valley, and a radius and central thickness error to within 8 microns.

8.2.4 Mount Repeatability Conclusion

To get a clear picture of how the mounts performed with respect to one another, Table 8-21

shows the error limits found from each mount along with the error limits from the vibration test. These

errors also include the errors from the user in identifying the exact cat's eye and confocal positions.

Table 8-21) Comparison of Error bars from the different mounts

	Vibration/ User Error	9 mm Mount	10.5 mm Mount	13 mm Mount
RMS	30 nm	20 nm	41 nm	130 nm
Peak to Valley	450 nm	287 nm	140 nm	560 nm
Radius	15 μm	15 μm	45 μm	8 μm
Central Thickness	15 μm	10 μm	26 μm	8μm

Since the vibration error is inherent in all measurements, the error limits from the vibration test

will set the floor for the minimum error that can be achieved. Based off this, the best mount to choose

would then be the 9mm mount since the error limits found from the mount are within the vibration

error limits. Thus, the interferometer can determine an RMS value to within 30 nm, a peak to valley

value to within 450 nm, a radius measurement to within 15 microns, and a central thickness

measurement to within 15 microns.

8.2.5 Central Thickness Error

By analyzing the data collected in the previous sections, it can be seen that if a 9mm base radius is

assumed, the radius measurement error corresponds to an accuracy to within of 0.167 %. Performing

the same analysis for the central thickness error, this measurement error corresponds to an accuracy to

within 8.14% using the average central thickness value of 184.3 microns for this lens. This is a large error

considering the precision achievable in determining the position of the contact lens. The ZYGO

(Middlefield, CT) DMI used to determine the position is accurate to within the nm range, so the question

is raised in why the central thickness has errors in the microns.

As stated in section 2.5, the central thickness measurement is inferred from the contact lens index

and the difference in cat's eye positions of the two surfaces. The central thickness error is actually not

due to determining the actual position of the contact lens, but it is due to the limited resolution of the

position control.

Recall that contact lens' axial position is controlled by the Thorlabs (Newton, NJ) MTS50-Z8 linear

stage. The reported minimal repeatable step size of the stage is 800 nm; however, the control program

written in the IDL software allows for a minimum step size of 10 microns. Furthermore, this 10 micron

movement is actually only repeatable to within 6 microns due to the backlash limit of the stage. Thus, it

makes sense that the resolution limit of the central thickness is around 15 microns since the contact lens

position is not controlled to a precision lower than this limit.

8.3   Verification with a Calibrated Surface

With an understanding on the limiting repeatability of the interferometer, the next verification

necessary was to see how well the interferometer reports surface data of a known surface. For this test,

two glass lenses provided by Optimax (Ontario, NY) were used. The lenses were made from the same

drawing, and data sheets were provided by the vendor from their QA test.

At Optimax, the lenses were tested on a Zygo Commercial interferometer with an RMS and peak

to valley value given from the surface profiles with tip, tilt, and power removed. The central thickness

was also provided within the spec sheets.

8.3.1 Calibration Surface 2-SN2

Without knowing the full details of the Optimax test, it was assumed that the Zygo interferometer was setup in a Fizeau fashion. This is pretty important to understand since the errors given were in terms of fringes. It was known that the surface was tested at 632.8 nm so the fringes could be converted back into units of lengths such as microns where one fringe is half of the test wavelength.

The profiles provided by Optimax for the first surface (the posterior surface) are shown in Figure 8.21 whereas the LOCOH profile is shown in Figure 8.22. The reported values for the radius, central thickness, RMS, and peak to valley errors from both interferometers is listed in Table 8-22.

Table 8-22) LOCOH to Optimax Comparison of SN2 Lens - Posterior Surface, 4 Zernikes removed

	Optimax Reported	Optimax Reported	LOCOH Measured	Difference
Radius	7.980 mm	-	7.9684 mm	0.00604 mm
Center Thickness	1.505 mm	-	1.467 mm	0.0380 mm
RMS	0.032 Fringes	$0.0101\ \mu m$	$0.062\ \mu m$	$0.0519\ \mu m$
Peak to Valley	0.156 Fringes	$0.0494\ \mu m$	$0.6051\ \mu m$	$0.6007\ \mu m$
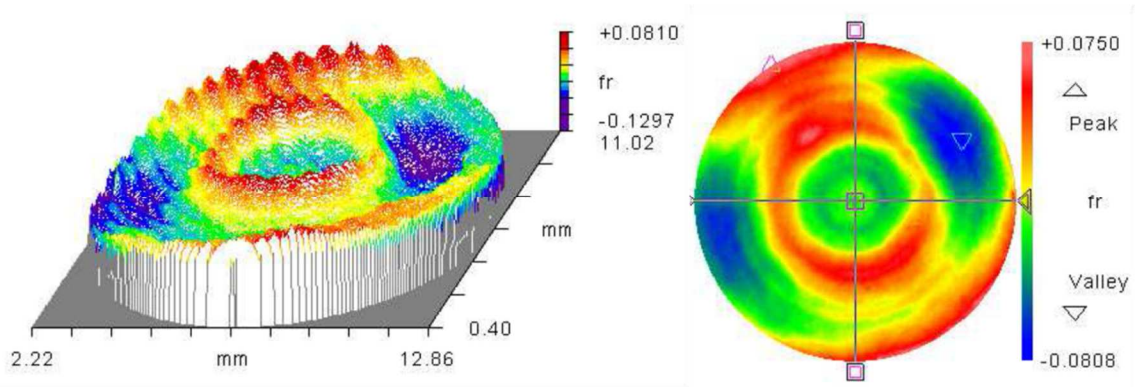
Figure 8.21) Optimax Profiles of the posterior surface for the calibration lens- SN2
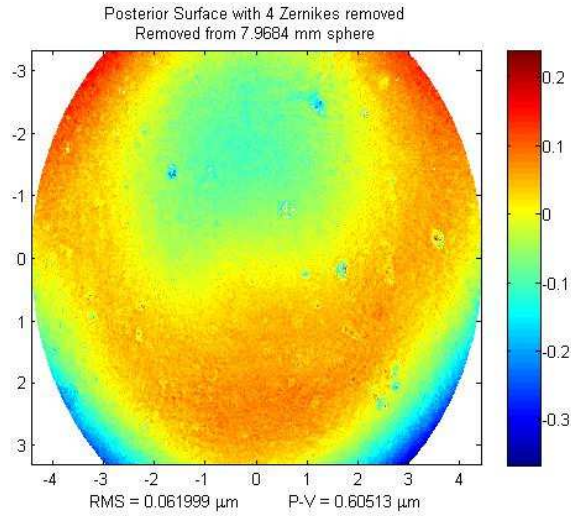
Figure 8.22) LOCOH profile of the posterior surface for the calibration lens - SN2

The first obvious difference is that the two surface profiles have opposite signs with the features. For example, where Optimax reports a valley, LOCOH reports a peak. This is due to opposite geometry setups. In LOCOH the shape of the lens is such that the concave feature is towards the beam. In the Optimax setup, the shape of the lens is such that the convex feature is towards the beam.

It should also be noted that for this surface, the interferometer used by Optimax was able to capture a diameter of 9mm from the surface whereas LOCOH captured 8.825 mm. For the second surface, Optimax was able to capture a diameter of 12.6 mm, whereas LOCOH would capture 11.051 mm. The tabulated data for the second surface is shown in Table 8-23 with Figure 8.22 and Figure 8.23 showing the Optimax and LOCOH profiles respectively.

Table 8-23) LOCOH to Optimax Comparison of SN2 Lens - Anterior Surface, 4 Zernikes removed

	Optimax Reported	Optimax Reported	LOCOH Measured	Difference
Radius	10.004 mm	-	9.9783 mm	0.0257 mm
RMS	0.023 Fringes	0.0073 μm	0.0702 μm	0.0629 μm
Peak to Valley	0.131 Fringes	0.0414 μm	0.6154 μm	0.5740 μm

Figure 8.23) Optimax profile of the anterior surface for the calibration lens 2-SN2
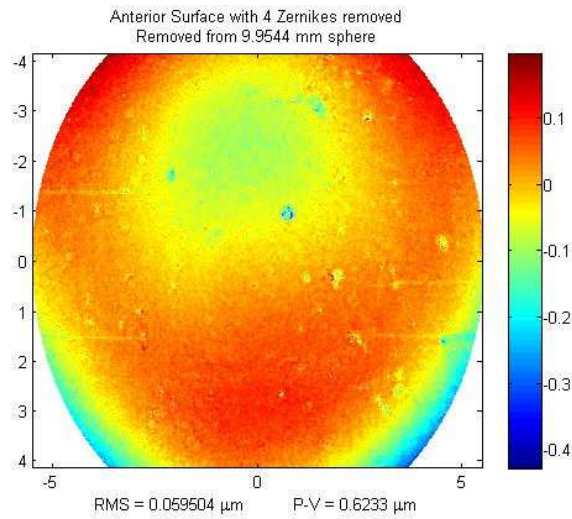
Figure 8.24) LOCOH profile of the anterior surface for the calibration lens 2-SN2

8.3.2   Calibration Surface 2-SN3

Just as with the previous lens, another calibration lens was placed in LOCOH to analyze its performance on a known surface. The tabulated data is shown in Table 8-24 and Table 8-25, and the surface profiles are shown in Figure 8.25 through Figure 8.28Figure 8.24.

Table 8-24) LOCOH to Optimax Comparison of SN3 Lens - Posterior Surface, 4 Zernikes removed

	Optimax Reported	Optimax Reported	LOCOH Measured	Difference
Radius	7.982 mm	-	7.9642 mm	0.0178 mm
Center Thickness	1.509 mm	-	1.511 mm	0.002 mm
RMS	0.079 Fringes	0.025 μm	0.0748 μm	0.0498 μm
Peak to Valley	0.361 Fringes	0.1142 μm	0.6706 μm	0.5564 μm
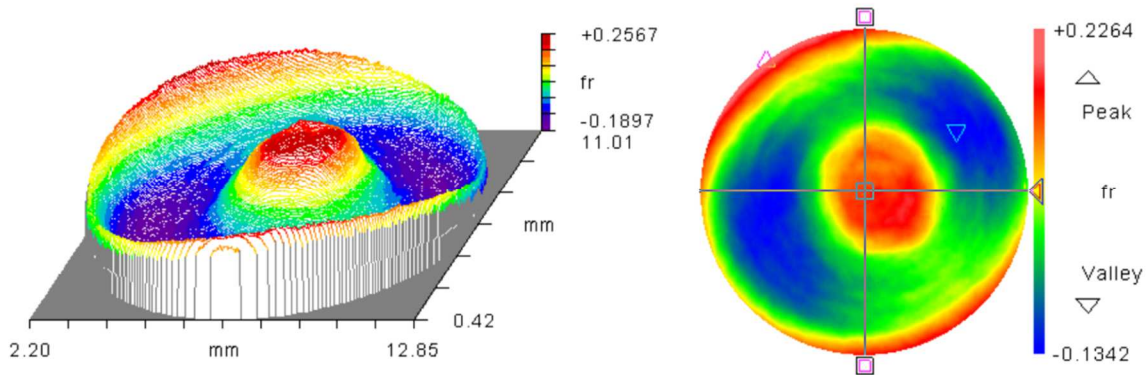
Figure 8.25) Optimax Profiles of the posterior surface for the calibration lens 2-SN3
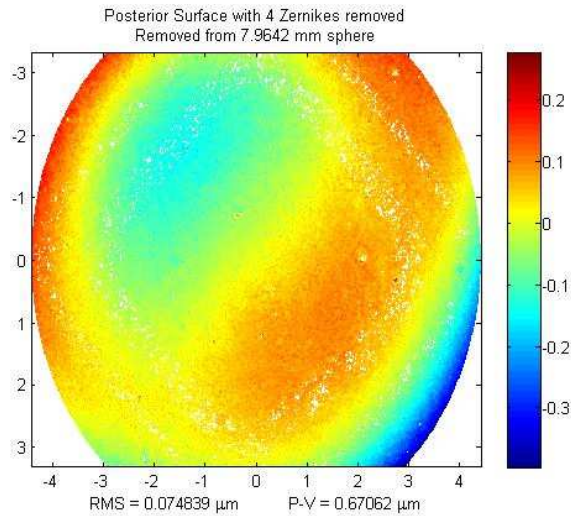
Figure 8.26) LOCOH profile of the posterior surface for the calibration lens 2-SN3

Table 8-25) LOCOH to Optimax Comparison of SN3 Lens - Anterior Surface, 4 Zernikes removed

|	Optimax Reported	Optimax Reported	LOCOH Measured	Difference
Radius	9.992 mm	-	9.9783 mm	0.0137 mm
RMS	0.038 Fringes	0.012 μm	0.0662 μm	0.0542 μm
Peak to Valley	0.193 Fringes	0.0611 μm	0.6382 μm	0.5771 μm

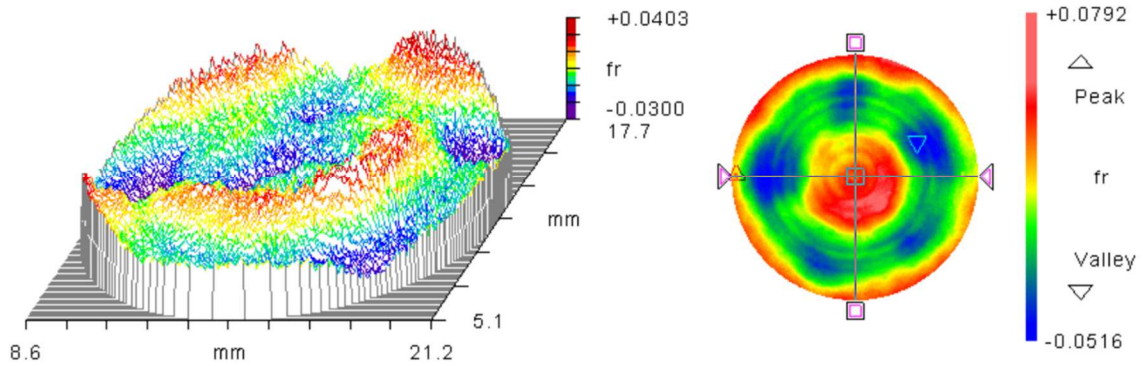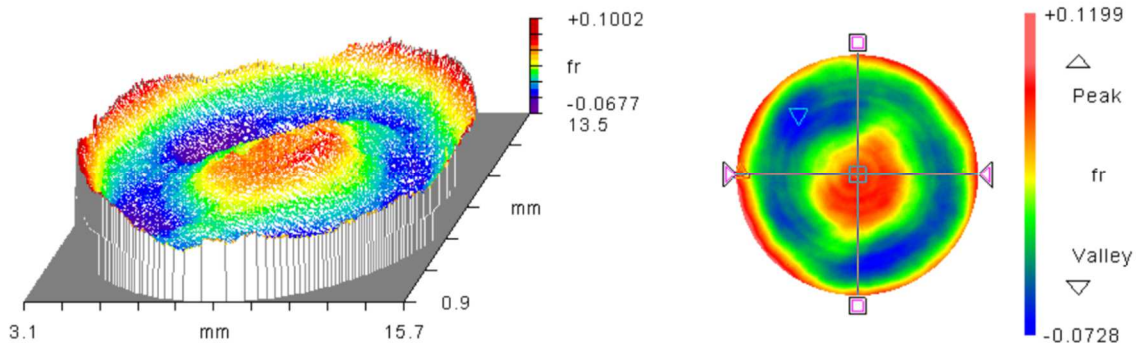*Figure 8.27) Optimax profile of the anterior surface for the calibration lens 2-SN3*
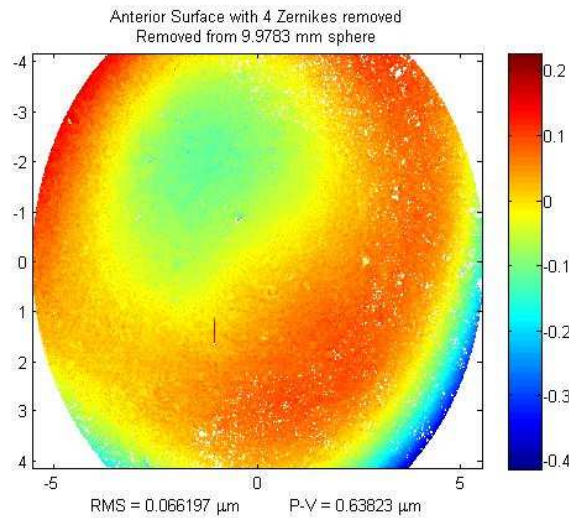
Figure 8.28) LOCOH profile of the anterior surface for the calibration lens 2-SN3

132

8.3.3   Comparison to Optimax Conclusion

Though the results of the two systems are not identical, they provide quite repeatable results. The LOCOH radius measurements have the highest correlation with the Optimax radius measurements. The average difference between the two is about 15 microns. This corresponds to a percent error to within 0.2 % assuming a standard radius of 8 mm. The central thickness values differ to within 20 microns which is about 30% larger than the known tolerance error of the LOCOH measurement for central thickness. At 20 microns, this corresponds to a percent error of about 1% considering a 1.5 mm thickness.

The RMS and peak to valley errors have larger percent differences between the two systems however. The peak to valley difference is much larger with an average difference of 577 nm. This is about 100 nm larger than the peak to valley error determined in section 8.2.4. For RMS, the average difference is around 55 nm which is not too bad considering the 30 nm tolerance of LOCOH.

To help clarify the analysis, Table 8-26 shows a statistical comparison of the results discussed above. To determine the percent difference with respect to Optimax, the average difference was taken over the average Optimax reported value for that measurement.

Table 8-26) Statistical comparison Optimax/LOCOH measurements

	Locoh Error Tolerance	Average Difference	% Difference (with respect to error)	% Difference (with respect to Optimax)
Radius	15 μm	15.81 μm	5.4 %	0.18%
Central Thickness	15 μm	20 μm	33.33%	1.33%
RMS	30 nm	54.7 nm	82.33 %	82.18%
Peak to Valley	450 nm	577.05 nm	28.23 %	767.42%

8.4   Simulated Transmission Profile

Continuing with the system performance analysis, arguably the most exciting result of LOCOH is to generate a transmission wavefront map from the data captured. Since the CLOVER interferometer briefly discussed in section 1 is used as a standard to verify the performance of manufactured contact lenses, having LOCOH agree with CLOVER allows for improved verification of manufactured contact lenses. For the sake of this report, this comparison also ensures that LOCOH is providing sensible results.

Three different lenses were chosen to be tested both in CLOVER and LOCOH for this test. To create the transmitted wavefront, software written in IDL was used to generate the raytracing from the two surface profiles and thickness profile captured by LOCOH interferometer. The CLOVER phase profile was also loaded into the software which models the entire CLOVER interferometer to determine the wavefront and remove interferometer induced errors (Heideman, 2014). The results of these measurements are shown below.

8.4.1   Etafilcon-A, 3.5 Diopters

The first lens tested is identical to the same lens used in the repeatability tests; however, it is not the same lens used previously. The lens prescription is 3.5 Diopters of spherical power and a base curvature of 8.5 mm. Figure 8.29 shows the data captured by LOCOH with 3 and 15 Zernikes removed as shown previously. Figure 8.30 shows the simulated transmitted wavefront along with the CLOVER measured wavefront and the difference between them. It should be noted that the profiles are shown with a percentile value of 0.98 to enhance the smaller features. This is part of the reason why the simulated wavefront has a "hole" in the center of the data. The other reason is due to a calculation error directly on axis from the raytracing. The results of CLOVER and LOCOH agree to about 55 nm RMS and 230 nm peak to valley.
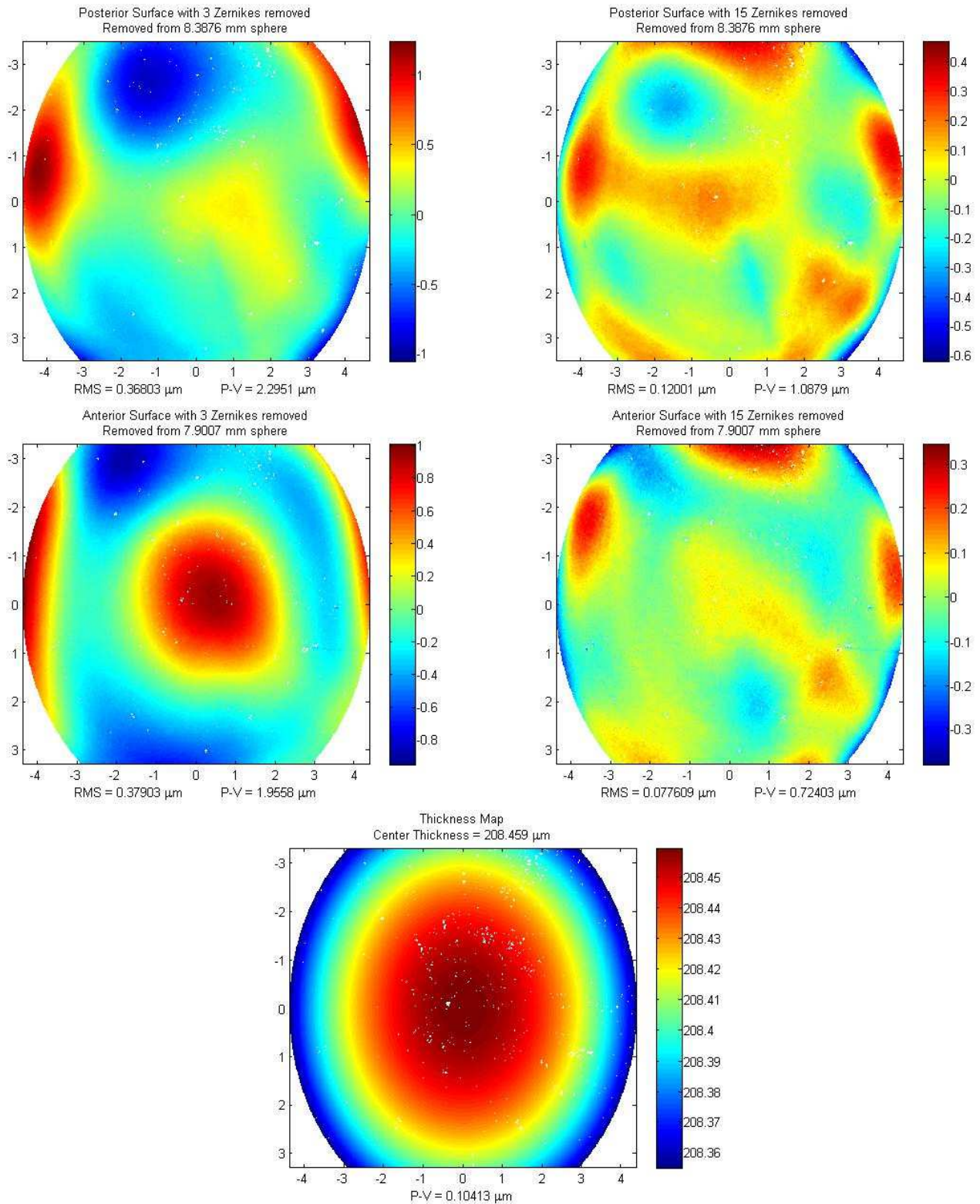
Figure 8.29) Locoh Captured Profiles – Etafilcon-A Lens, 3.5 Diopters

LOCOH

CLOVER

RMS = 319.52nm | P-V = 1110.77nm

RMS = 269.28nm | P-V = 949.87nm

Difference Between Simulated and Measured Transmission Maps

RMS = 54.78nm | P-V = 231.37nm
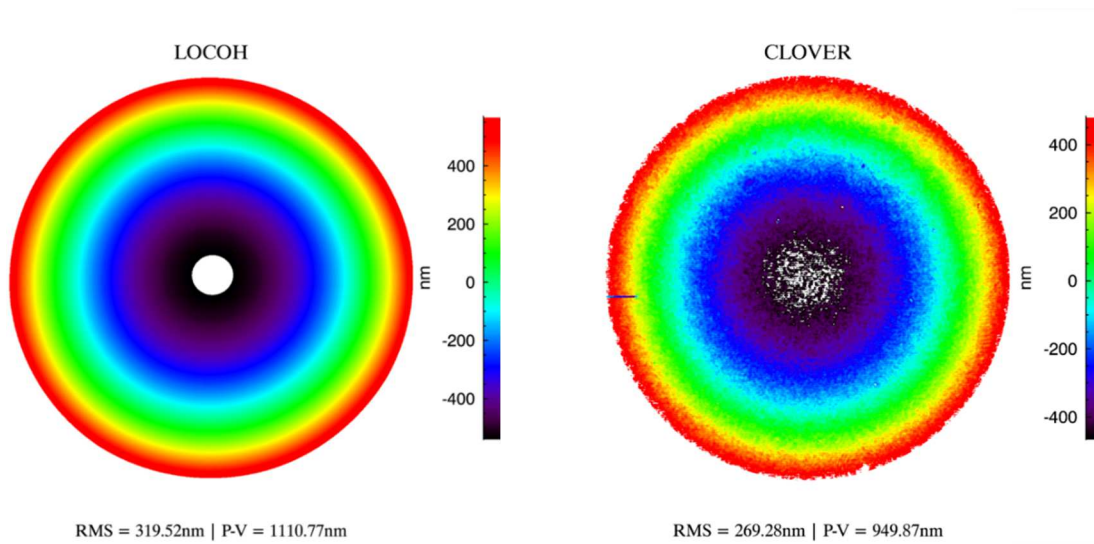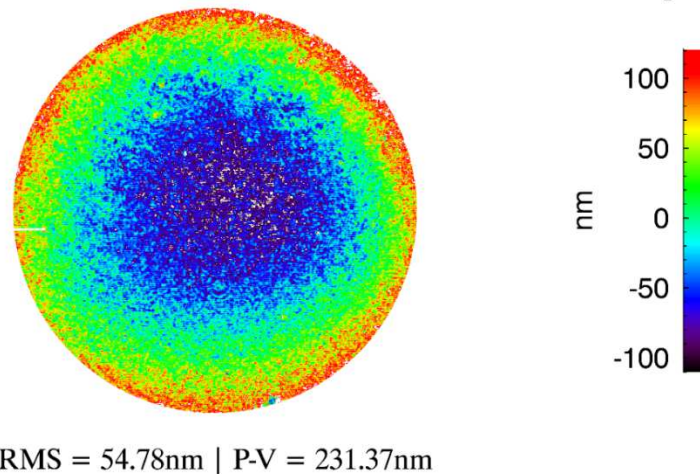
Figure 8.30) Transmission Comparison of Etafilcon-A Lens, 3.5 Diopters

8.4.2   Clinical Trial Lens, -1.25 Diopters

The next lens tested was a clinical trial lens and very little data is given about it. It was reported to have a spherical power of -1.25 Diopters. Figure 8.31 and Figure 8.32 show the LOCOH captured profiles along with simulated wavefront. All lenses processed in this section have consistently been positive lenses. Interestingly enough, the thickness profiles follows what should be expected of a negative lens with a thinner center and thicker edges. The transmitted profiles also agree with a RMS error of about 40 nm and peak to valley error of about 184 nm.

Posterior Surface with 3 Zernikes removed
Removed from 7.8154 mm sphere

RMS = 1.1458 µm   P-V = 5.7312 µm

Posterior Surface with 15 Zernikes removed
Removed from 7.8154 mm sphere

RMS = 0.24784 µm   P-V = 2.4147 µm

Anterior Surface with 3 Zernikes removed
Removed from 8.0421 mm sphere

RMS = 1.4011 µm   P-V = 6.804 µm

Anterior Surface with 15 Zernikes removed
Removed from 8.0421 mm sphere

RMS = 0.25579 µm   P-V = 2.5621 µm

Thickness Map
Center Thickness = 110.1062 µm

P-V = 0.063152 µm

Figure 8.31) Locoh Captured Profiles – Clinical Trial Lens, -1.25 Diopters

137

LOCOH

RMS = 129.62nm | P-V = 449.23nm

CLOVER

RMS = 96.55nm | P-V = 370.28nm

Difference Between Simulated and Measured Transmission Maps

RMS = 40.29nm | P-V = 183.56nm
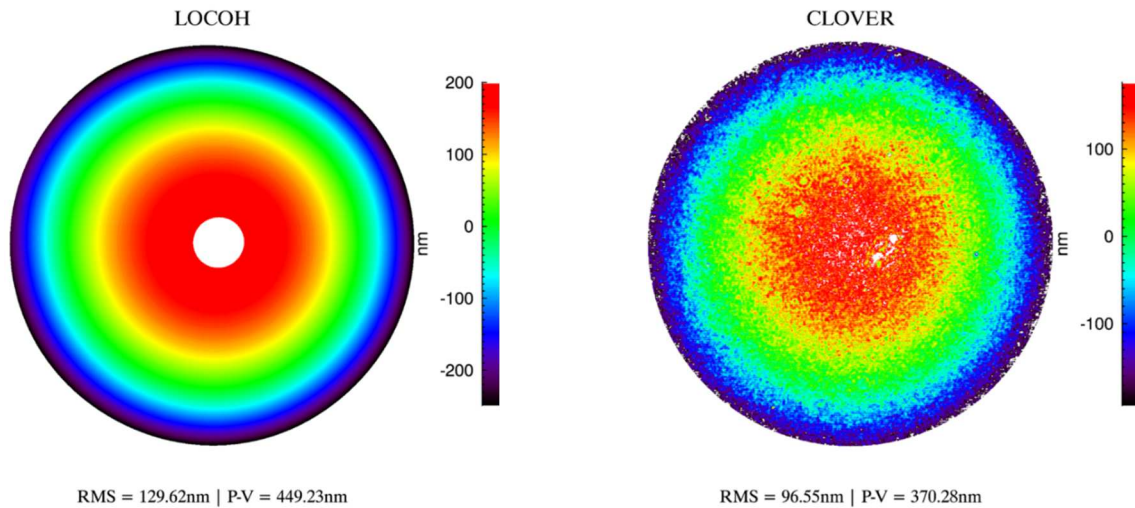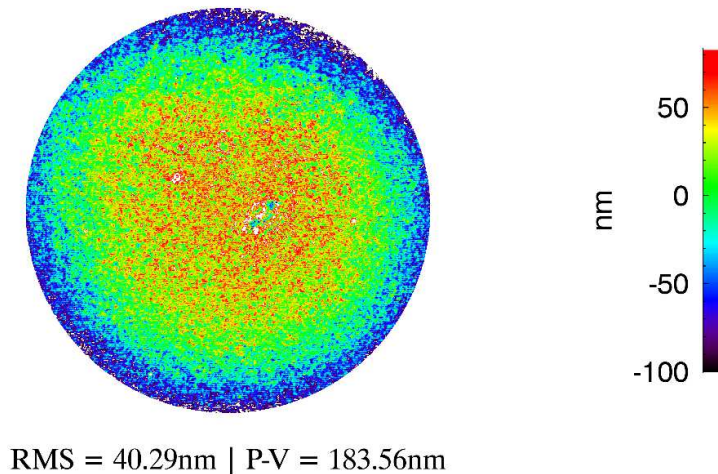
Figure 8.32) Transmission comparison of Clinical Trial Lens, -1.25 Diopters

8.4.3   Toric, -1 Diopters & -1.25 Diopters

The last lens tested was a Toric lens with a reported spherical power of -1 diopters and cylindrical power of -1.25 diopters. Special care was taken to ensure that lens was mounted in the same orientation between the two interferometers or that they would be at least rotated by 90 which could be fixed in post processing. Figure 8.33 and Figure 8.34 show the LOCOH captured profiles along with the transmitted comparison. The reported RMS error is 98 nm with a peak to valley error of about 406 nm.
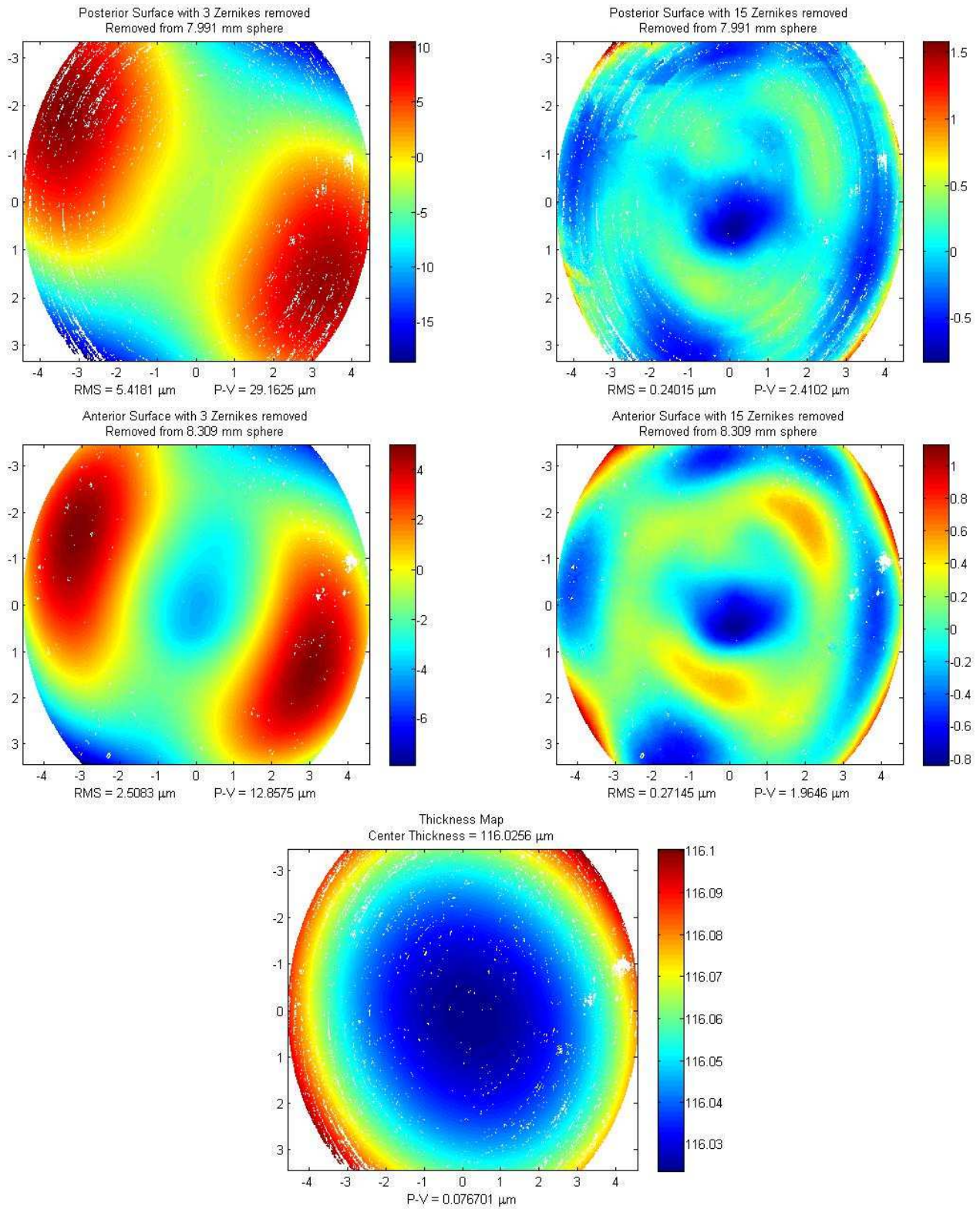
Figure 8.33) LOCOH Captured Profiles –Toric, -1 & -1.25 Diopters

LOCOH

CLOVER

RMS = 230.53nm | P-V = 925.25nm

RMS = 152.62nm | P-V = 631.74nm

Difference Between Simulated and Measured Transmission Maps

RMS = 97.69nm | P-V = 406.31nm
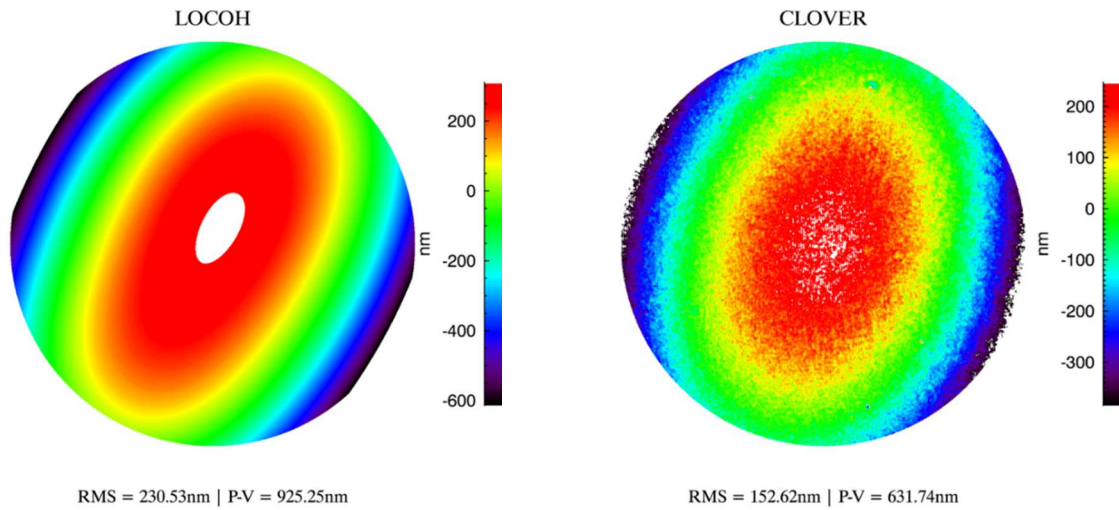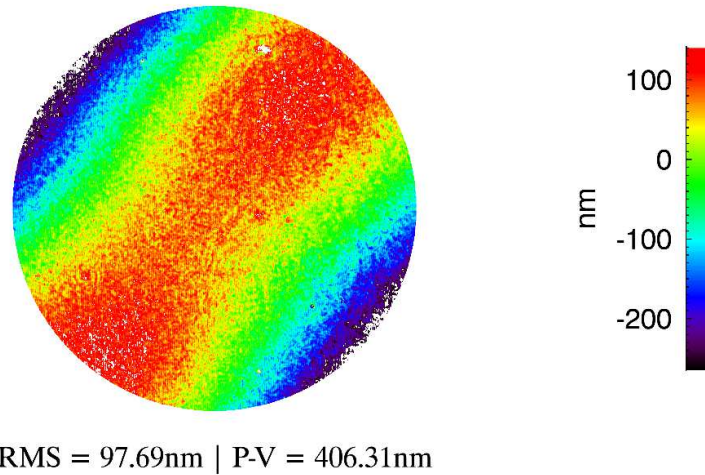
Figure 8.34) Transmission Comparison of Toric, -1 & -1.25 Diopters

8.4.4   Transmitted Comparison Conclusion

The results are quite promising for the transmitted profiles. The average RMS error is 64.25 nm, and the average peak to valley error is 273.75 nm. The two spherical lenses provide a reasonably uniform difference profile, while the toric lens does show more features. This makes sense since the toric lens is very sensitive to rotational errors.

To make a proper comparison of the toric profiles, the lens should be mounted identically in both LOCOH and CLOVER. Initially the, CLOVER data had the transmission profile rotated 90 from what is

shown. A simple 90 degree matrix rotation was performed on the clover data after being processed; however, fine tuning of the LOCOH transmitted profile and the CLOVER profile show that there is still a few degrees of error. Thus, the regions of the contact lens in the measurements were not properly overlapped when determining the difference. The effect is small so it wasn't addressed, but it should be noted.

8.5   Comparison to Old Data

The last test performed was to see if there had been an improvement by comparing data from the initial build of LOCOH with the data captured in the new configuration. For this, two lenses were selected that were presented in section 5. The first data presented is from the E3 lens (+8 Diopters with a base curvature of 8.3mm) shown in section 5.1.1. The second lens was the special distorted lens shown in section 5.2.1 tagged 07.

Since there was not a dramatic variation in the profile appearance, one measurement of the new system and one measurement from the old system are shown; however, the statistics presented are taken over several measurements if they existed. For the initial LOCOH E3 lens, only one measurement was taken previously, thus, the mean values of the new measurements was compared to the single initial measurement. The distorted lens had 3 measurements taken in the initial build so the mean value of the new measurements and old measurements are compared.

The data is presented such that the statistics are shown first, followed by the profiles. Like the previous data shown, this includes the posterior and anterior surfaces with both 3 and 15 Zernikes removed along with the thickness profile. Table 8-27 through Table 8-36 list the data and Figure 8.35 through Figure 8.44 show the profiles.

Table 8-27) Statistical Comparison between new and initial measurements of E3 Posterior Surface – 3 Zernikes Removed

	Difference	% Difference	Increase or Decrease
Radius (mm)	0.1896	2.1417	Decrease
RMS (μm)	0.1804	15.4863	Decrease
Peak to Valley (μm)	3.2431	35.3237	Decrease

Figure 8.35) Posterior profile comparison of E3 lens - 3 Zernikes removed
The new system result is on the left, the initial system is on the right – note that there is a scale change between the two

Table 8-28) Statistical Comparison between new and initial measurements of E3 Posterior Surface – 15 Zernikes Removed

	Difference	% Difference	Increase or Decrease
RMS (μm)	0.1460	50.7895	Decrease
Peak to Valley (μm)	1.6820	52.9847	Decrease

Figure 8.36) Posterior profile comparison of E3 lens - 15 Zernikes removed
The new system result is on the left, the initial system is on the right– note that there is a scale change between the two

Table 8-29) Statistical Comparison between new and initial measurements of E3 Anterior Surface – 3 Zernikes Removed

	Difference	% Difference	Increase or Decrease
Radius (mm)	0.1471	1.9165	Decrease
RMS (μm)	0.0773	7.9052	Decrease
Peak to Valley (μm)	2.2802	28.4584	Decrease
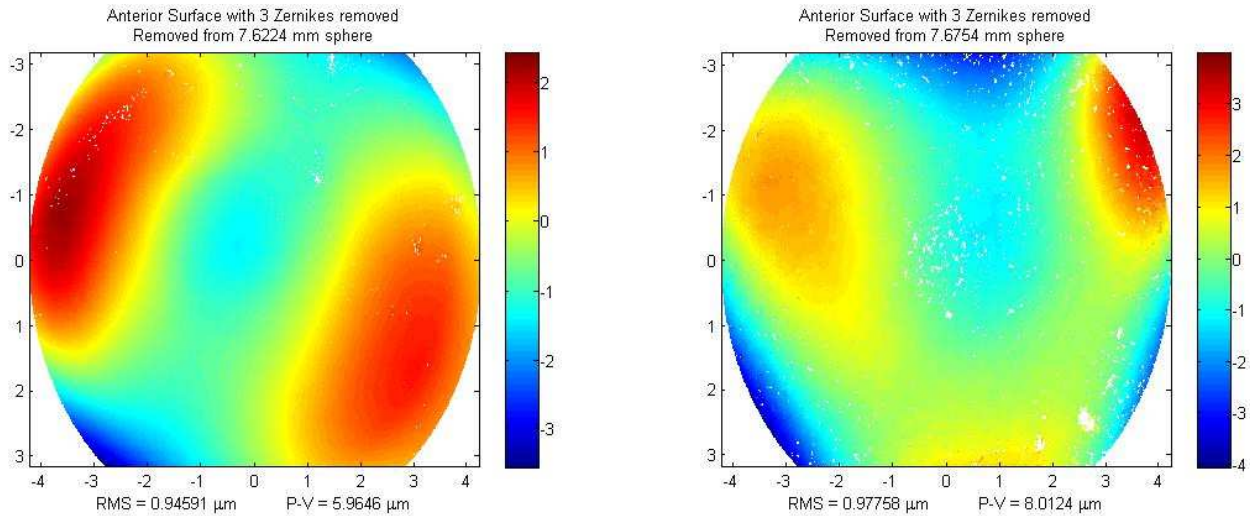
Figure 8.37) Anterior profile comparison of E3 lens - 3 Zernikes removed
The new system result is on the left, the initial system is on the right– note that there is a scale change between the two

Table 8-30) Statistical Comparison between new and initial measurements of E3 Anterior Surface – 15 Zernikes Removed

	Difference	% Difference	Increase or Decrease
RMS (μm)	0.0863	45.2392	Decrease
Peak to Valley (μm)	1.8591	65.6276	Decrease

Figure 8.38) Anterior profile comparison of E3 lens - 15 Zernikes removed
The new system result is on the left, the initial system is on the right– note that there is a scale change between the two

Table 8-31) Statistical Comparison between new and initial measurements of E3 Thickness Profile

	Difference	% Difference	Increase or Decrease
Central Thickness (μm)	9.8388	3.5293	Increase
Peak to Valley (μm)	0.0078	3.8039	Increase

Figure 8.39) Thickness profile comparison of E3 lens
The new system result is on the left, the initial system is on the right

Table 8-32) Statistical Comparison between new and initial measurements of 07 Posterior Surface – 3 Zernikes Removed

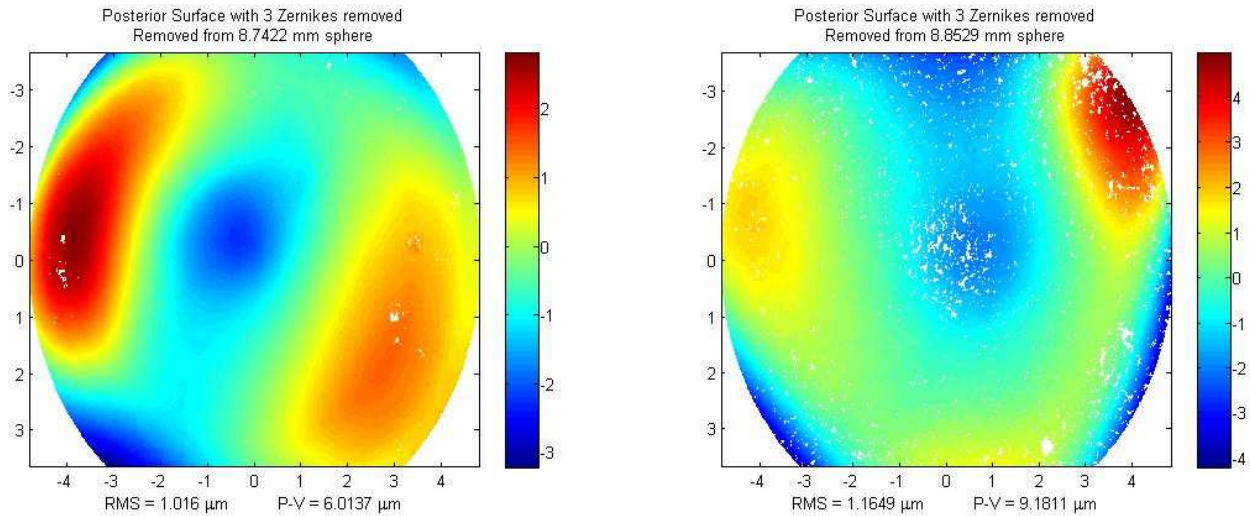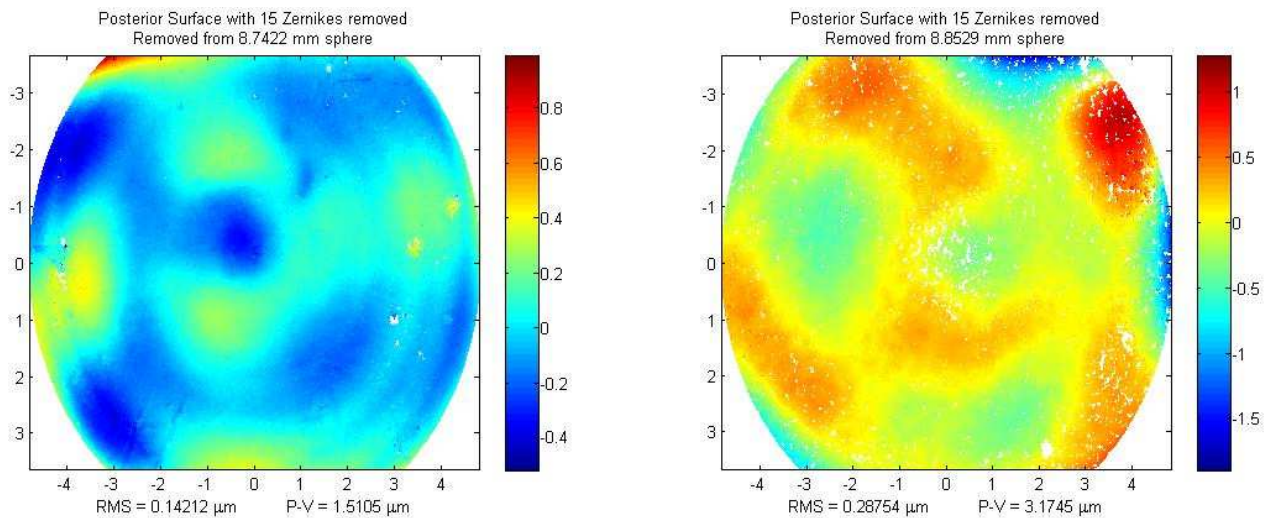|	Difference	% Difference	Increase or Decrease
Radius (mm)	0.0002	0.0023	Increase
RMS (μm)	1.2291	68.3707	Increase
Peak to Valley (μm)	0.9477	5.8773	Decrease
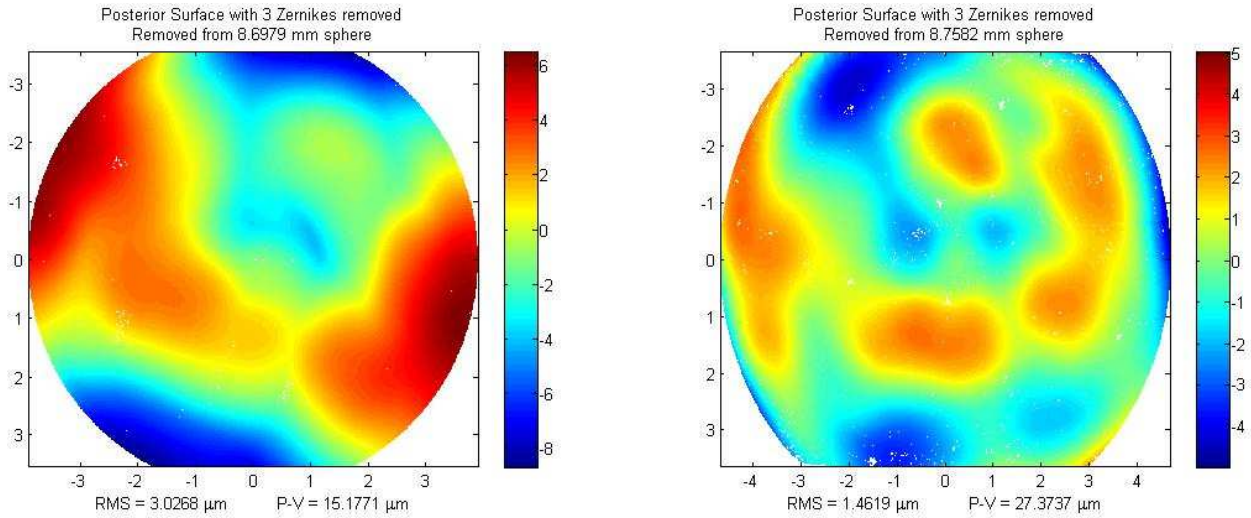
Figure 8.40) Posterior profile comparison of 07 lens - 3 Zernikes removed
The new system result is on the left, the initial system is on the right– note that there is a scale change between the two

Table 8-33) Statistical Comparison between new and initial measurements of 07 Posterior Surface – 15 Zernikes Removed

	Difference	% Difference	Increase or Decrease
RMS (μm)	0.2662	27.3398	Decrease
Peak to Valley (μm)	4.5769	48.2872	Decrease
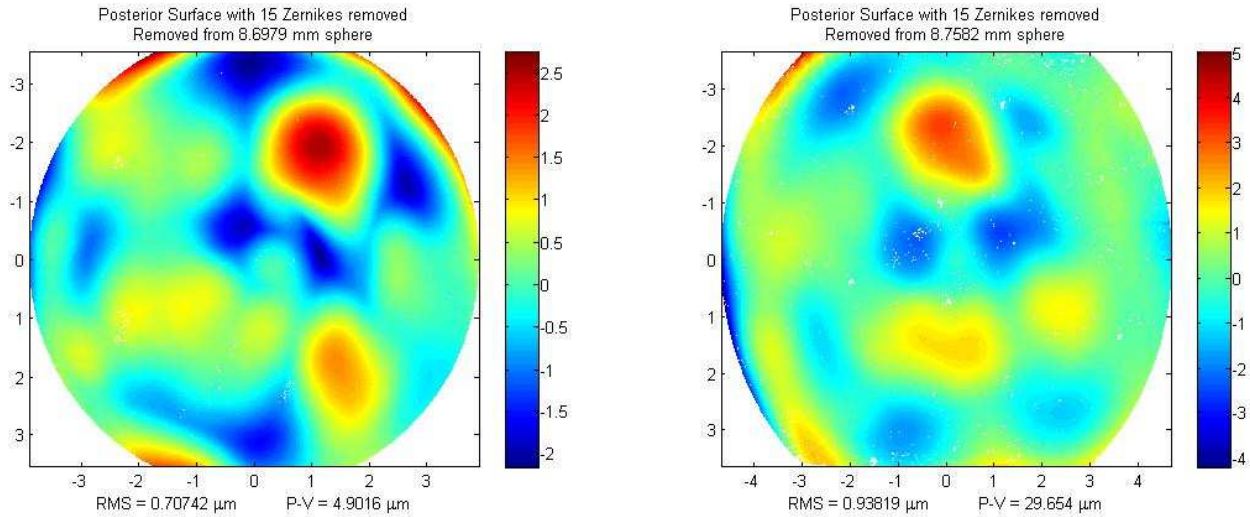
Figure 8.41) Posterior profile comparison of 07 lens - 15 Zernikes removed
The new system result is on the left, the initial system is on the right– note that there is a scale change between the two

Table 8-34) Statistical Comparison between new and initial measurements of 07 Anterior Surface – 3 Zernikes Removed

|	Difference	% Difference	Increase or Decrease
Radius (mm)	0.0597	0.6593	Decrease
RMS (μm)	1.4984	48.5265	Increase
Peak to Valley (μm)	3.7609	23.0148	Increase
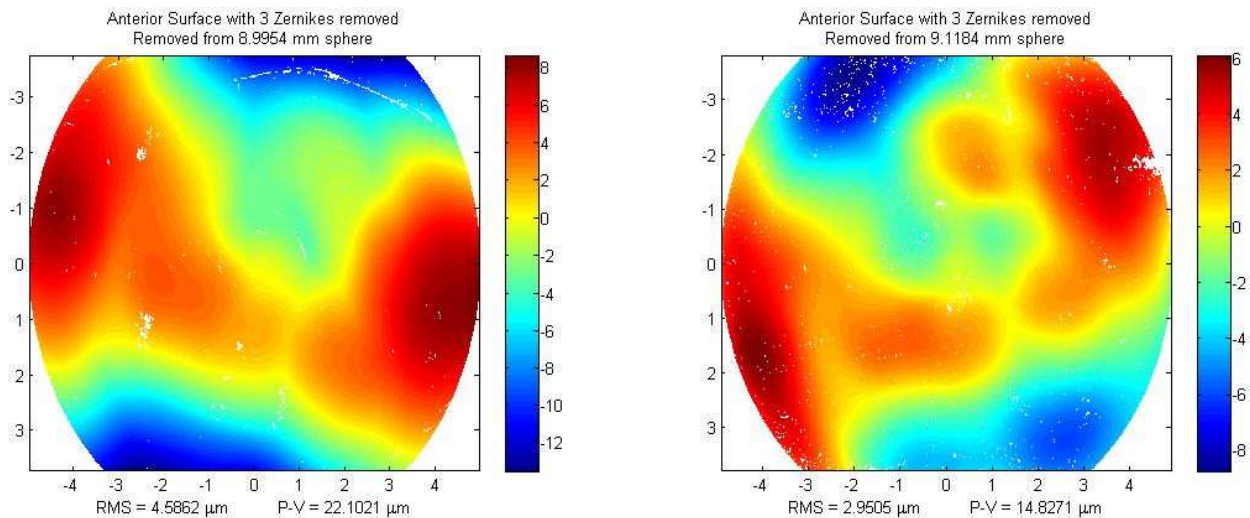
Figure 8.42) Anterior profile comparison of 07 lens - 3 Zernikes removed
The new system result is on the left, the initial system is on the right– note that there is a scale change between the two

Table 8-35) Statistical Comparison between new and initial measurements of 07 Posterior Surface – 15 Zernikes Removed

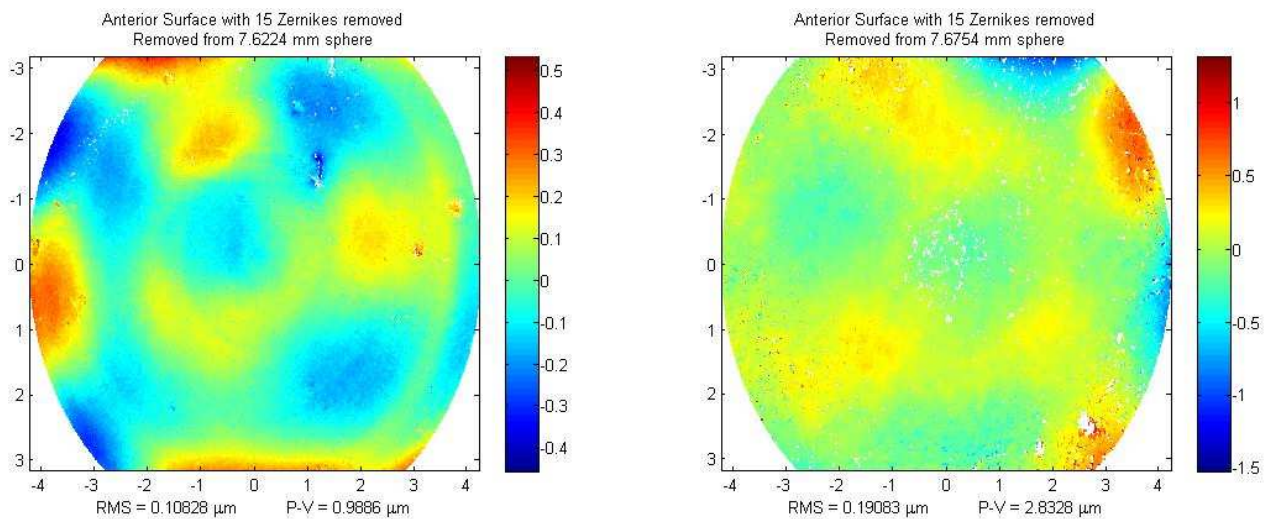|	Difference	% Difference	Increase or Decrease
RMS (μm)	2.2913	74.2040	Decrease
Peak to Valley (μm)	10.4100	63.7040	Decrease
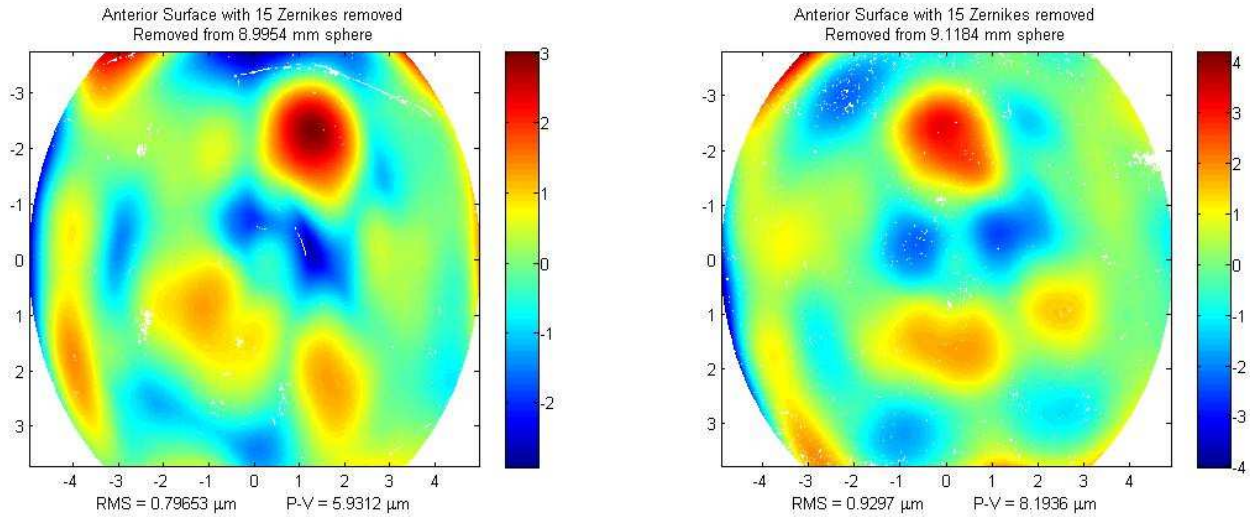
Figure 8.43) Anterior profile comparison of 07 lens - 15 Zernikes removed
The new system result is on the left, the initial system is on the right– note that there is a scale change between the two

Table 8-36) Statistical Comparison between new and initial measurements of 07 Thickness Profile

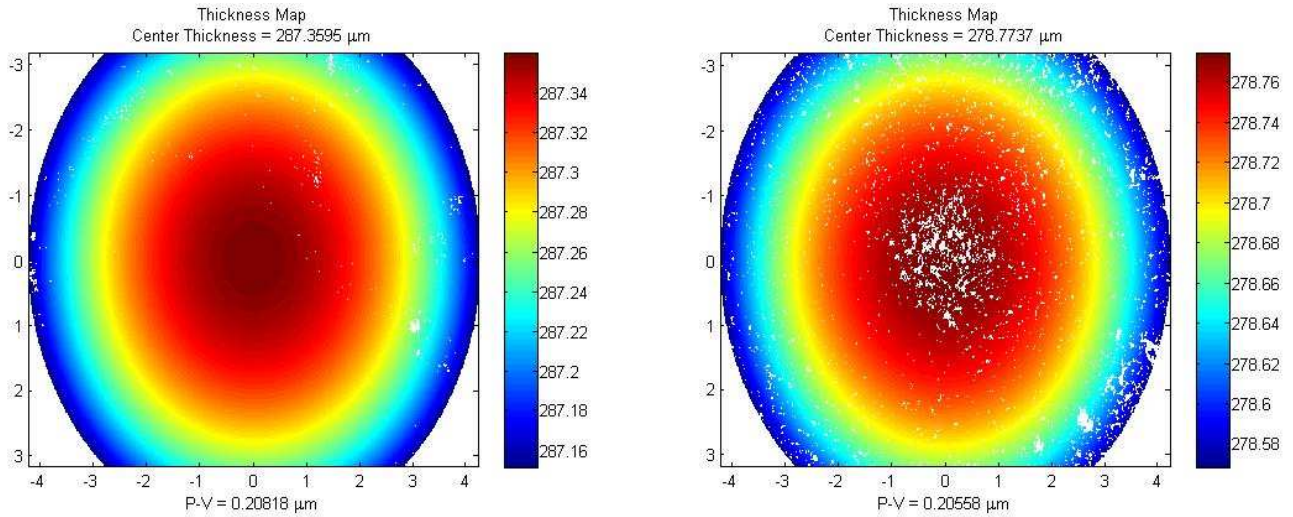|	Difference	% Difference	Increase or Decrease
Central Thickness (μm)	12.6148	14.0103	Decrease
Peak to Valley (μm)	0.0321	59.3771	Decrease
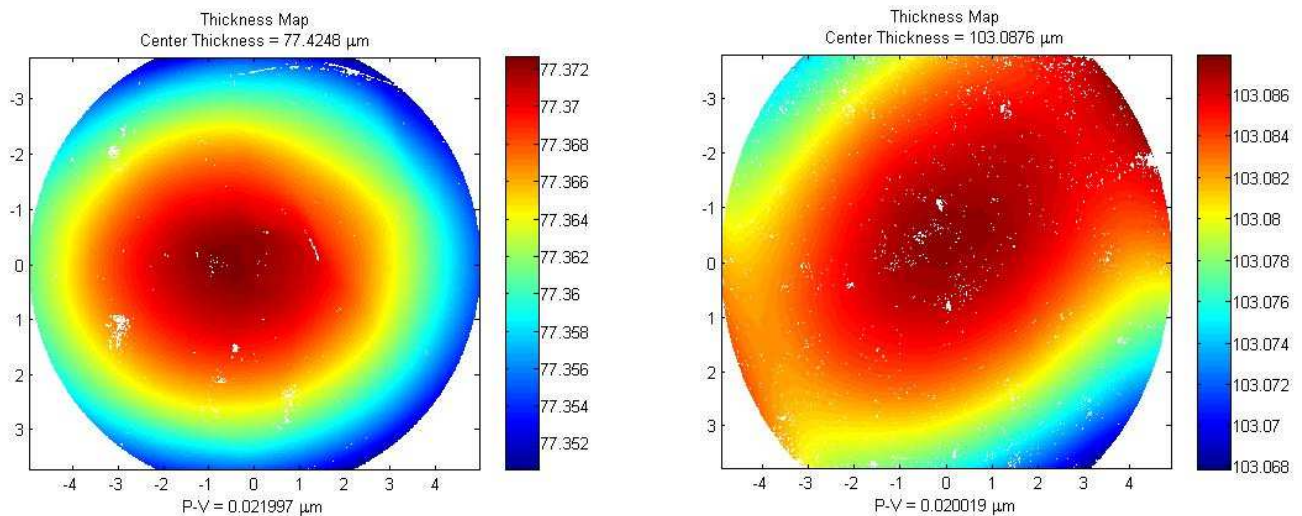
Figure 8.44) Thickness profile comparison of 07 lens
The new system result is on the left, the initial system is on the right

8.5.1 Conclusion on Comparison

By comparing the differences between the mean values of the measurements, the results from the commercial E3 lens show that there has been an improvement in the surface profiles measured with the new system, but not necessarily the thickness profile. The RMS, peak to valley, and radius measurements of the two surfaces have all decreased in magnitude beyond the error limit defined by the vibration and mount analysis. The thickness profile showed an increase in value; however, the difference in means between the initial and new measurements are within the error limit defined previously. Thus, there has been no significant degradation in performance with the new layout. In fact, the trefoil seen in the initial system measurements is gone, and the overall distortion has been greatly reduced.

Comparing the distorted 07 lens does not show the same results as the E3 lens. When the surfaces have 3 Zernikes removed, the RMS and peak to value errors are larger in the new system than in the previous; however, with 15 Zernikes removed, the values are lower. The magnitude of the difference in means is larger than the error limits set by the vibration and mount analysis. The mean differences in radii and central thickness measurements are within the error, and thus can be ignored.

Since the distorted lens was known to be irregular in the surface shape, it would not be ideal to use this lens to compare the performance of the new and old system, but it is interesting to see that the features measured are common to both setups. Thus, it is safe to say that an improvement has indeed been made in performance with the new system, though it is not significantly large. The percentage of improvement averages around 37% but the standard deviation of this improvement is 19%. The distorted lens information should not be discarded lightly though as it shows that system is still sensitive to errors when measuring dramatic features. This will be discussed further in the following chapter.

9   Future Improvement and Conclusion

This report has provided great detail on the upgrades performed to LOCOH in order to address

problems encountered from the initial build of the system. Issues like visibility, the inability to reach

cat's eye measurement positions, and repeatability have been addressed solely with just the mechanical

layout upgrade. The tank system allows for an interchangeable mounts providing future users the ability

to design a small mount based on the needs of any special case measurements. The ring support of the

9mm mounts provide more than adequate stability to the contact lenses without distorting the surface

profile, while the 13 mm mount allows for easy centering of small glass lenses as seen with the

calibration surfaces.

Software improvements have been made to both the measurement and post processing GUI's to

overcome noise in the data as well as improve the accuracy of the reconstructed surface. That said,

these corrections do not solve all issues and there are still improvements that can be made.

9.1   Phase Unwrapping Implementation

Much research and analysis has been presented on an improved phase unwrapping routine which

significantly helps overcome the low visibility inherent to the optical system. Not mentioned in chapter 8

was that the measurements taken did not fully implement the phase unwrapping routine presented in

chapter 7. At the time of this writing, and when analyzing the measurements presented, the main post

processing GUI in IDL (Exelis Visual Information Solutions, 2013）was unable to accept the code

demonstrated in Matlab (Mathworks, 2013) to overcome the noise from the system.

Work is currently ongoing to have the IDL software communicate with the ideal unwrapping routine

since the IDL software has the necessary reverse raytracing algorithm. The IDL software is currently not

robust enough to take outside processed data so the old phase unwrapping routine must still be used. That said, many changes were implemented to help push the old routine along the correct trajectory.

Residue detection was added to the IDL phase unwrapping routine along with visibility correction for low visibility pixels. Low visibility pixels that are typically ignored can be added back into the routine by analyzing which of those ignored pixels satisfy the PDV thresholding method described in section 7.3 and replacing the visibility values of those pixels such that it is larger than 10%. Unfortunately, the visibility threshold is still necessary for the current post processing phase unwrapping as it is not quality guided. Also, since there is nothing to define the order in which the pixels unwrap, using residue detection only, as discussed in section 7.6, will result in phase streaks as shown in Figure 9.1. This is the same profile demonstrated throughout chapter 7.
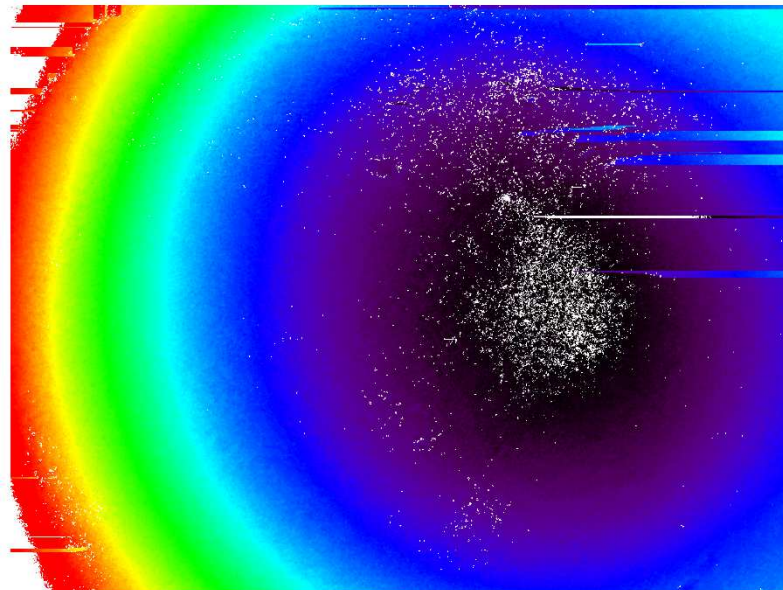
Figure 9.1) Phase Streaks from Lack of Quality Guidance

Once the routine is properly implemented, much analysis code has been developed which should quickly reprocess all the data shown. There is no need to perform another physical measurement on any of the contact lenses presented. Luckily, the phase unwrapping does not seem to be the key problem in

surface reconstruction. The results presented may slightly increase in performance once the ideal routine from chapter 7 is fully implemented, but to better improve the surface reconstruction, the reverse raytracing should be visited.

9.2   Reverse Raytracing

Though this was never shown in the report, many reverse raytraced profiles fall apart at the edges. Often, the data at the edges has very high departure values resulting in discontinuous shapes which can lead to peak to valley errors as high as 10 microns. This is significantly larger than the data shown, and the surfaces are often cropped to remove these errors.

These sharp edges are never seen on the phase unwrapped profile from either the new phase unwrapping routine or old routine. This implies that the error comes from the reverse raytracing algorithm. It should also be noted that these sharp edges are always seen on toric surfaces. If the spherical surface have data captured across the entire aperture, the discontinuous shape never occurs. Toric lenses have to be stitched back together often to capture the entire profile, but if there is some corner on the detector that does not have fringes, the discontinuous shape will occur.

For this upgrade, the reverse raytracing has not been research or improved upon aside for a few sign error corrections. Another member of this lab has demonstrated a powerful reverse raytracing algorithm which should be studied if improvements are to be made (Jason D Micali & Greivenkamp, 2016).

It should also be noted that the algorithm may require a few lens position corrections simply due to altering the opto-mechanical layout. When inverting the system, the interferometer was reconstructed so that the optics were all nominally in the same location as before, but small OPL changes can have a big effect on reverse raytracing (Jason D Micali & Greivenkamp, 2016).

9.3   Improvements to the Diverger Lens Barrel

An issue that remains with the current barrel and tank design is it does not to do a great enough job to mitigate bubbles. The ideal tank and barrel system should be completely submerged in the solution so that no air is introduced when passing contact lenses through.

In the current setup, the contact lens is installed into the mount which is exposed to air. As the tank is brought towards the diverger lens barrel, tiny air bubbles can get trapped between the waveplate and the contact lens. These tiny bubble definitely reduce visibility in regions (as shown in chapter 7), but if large enough, they can simulate fringes with the reference arm blocked. In most cases, they prevent the contact lens from being seen at all.

Currently to get around the problem, the tank is very slowly translated until the barrel is completely submerged in saline. Prior to translating the tank, saline is filled between the wave plate and diverger lens such that the waveplate itself acts as a hermitic seal to prevent the saline from escaping. Once the tank is completely lowered so that the barrel is no longer submerged, this "hermetic" seal will break and the barrel has to be removed for the waveplate to be reapplied. Thus, the waveplate is not actually compressed again the barrel as the design had intended. This is fine for a bench top R&D environment, but a lot of time is consumed ensuring that this setup is bubble free.

This also indicates that the bubble vent holes placed in the design are not doing an adequate enough job. This makes sense in hindsight since the groves are horizontal. If a slight incline is added to the grooves away from the lens, the bubbles will be channeled into air which is ideal. Currently, the bubble can only be channeled while the lens is not completely submerged. This is why the waveplate is applied as "seal" rather than being compressed. Without any significant physical shift, the vacuum created between the waveplate and diverger lens barrel will not break allowing solution to escape.

9.4 Quarter Wave Plate

Continuing with the test arm waveplate, the quarter waveplate film should be upgraded to a higher quality waveplate. Currently, the film is very susceptible to scratches and is often statically charged which attracts dust. These dust particles can be seen moving in the fluid across the interferograms which can lower visibility or corrupt pixel values.

The inherent scratches on the polymer do not provide significant degradation, but as the solution evaporates over time or is wiped off to prevent salt crystal build up, the wave plate slowly loses it transmissive profile and starts to scatter light back into the interferometer. Currently, the waveplate is replaced daily which requires removing the diverger lens. This in turn causes the need for realignment of the test arm to ensure its optical axis is aligned properly with the detector. This is not impossible, but takes time which is not ideal in industrialization.

9.5 Summary

To conclude the report on this upgrade, a new opto-mechanical layout has been designed and implemented which reduces back scatter from the use of a proper beam dump while stabilizing the contact lens during measurements with a ring mount. To overcome low visibility inherent of the contact lens, phase unwrapping has been improved though the use residue detection, and proper thresholding. The interferometer has been demonstrated to have a repeatability to within 15 microns for both the central thickness and radius measurements, a repeatability to within 30 nm ($\approx \lambda/20$) RMS, and a peak to valley repeatability of 450 nm. The transmitted wavefronts modeled using LOCOH captured data match very closely to CLOVER measured profiles with a 65 nm RMS variation and 275 nm peak to valley variation. It is very likely these errors reported are high and can be shown to be lower with more repeatability measurements. The typical peak to valley error reported is very often within the 450 nm error determined.

About a 50% increase in overall performance has been shown from previously measured surface profiles; however, the idea that the previous mount was inducing significant low frequency distortions may be true, but it is not as significant as was expected. Previously measured features still appear with this new ring mounted scheme; however, the stability of the contact lenses, increased repeatability, and significant improvement in measurement ease demonstrates that this upgrade was necessary. Table 9-1 compares the initial LOCOH tolerance found in section 5.3 with the new layout discussed in section 8.2.4.

Table 9-1) Comparison of Old and New System Errors

	Initial Error	New System Error	% Change
Radius (μm)	57	15	73.68%
RMS (nm)	55	30	45.45%
Peak to Valley (nm)	600	450	25%
Central Thickness (μm)	57	15	73.68%

REFERENCES

Ghiglia, D. C., & Pritt, M. D. (1998). *Two-dimensional phase unwrapping: theory, algorithms, and software*. Wiley.

Goodman, J. W. (2000). *Statistical Optics* (Wiley Clas). Wiley.

Goodwin, E. P. (2007). *Dual interferometer system for measuring index of refraction*. University of Arizona.

Greivenkamp, J. E., Williby, G. a., Goodwin, E. P., Primeau, B. C., Heideman, K. C., Micali, J. D., & Spaulding, R. T. (2014). Interferometry and ophthalmics at the College of Optical Sciences. *SPIE Proceedings*, *9186*, 91860W. http://doi.org/10.1117/12.2064333

Hariharan, P. (2007). Multiple-Pass Interferometers. In D. Malacara (Ed.), *Optical Shop Testing* (pp. 259–274). Wiley Interscience.

Heideman, K. C. (2014). *Surface Metrology of Contact Lenses In Saline Solution*. University of Arizona.

Heideman, K. C., & Greivenkamp, J. E. (2016). Low-coherence interferometer for contact lens surface metrology. *Optical Engineering*, *55*(3). http://doi.org/10.1117/1.OE.55.3.034106

Malacara, D., Creath, K., Schmit, J., & Wyant, J. C. (2007). Testing of Aspheric Wavefronts and Surfaces. In D. Malacara (Ed.), *Optical Shop Testing* (Vol. 1, pp. 435–497). Wiley Interscience.

Micali, J. D. (2015). *Interferometer for Measuring Dynamic Corneal Topography*. University of Arizona.

Micali, J. D., & Greivenkamp, J. E. (2016). Method for reconstruction of complex surface shapes from a reflection-based non-null interferometric measurement. *Optical Engineering*, *55*. http://doi.org/10.1117/1.OE.55.3.034101

Millerd, J. E., Brock, N. J., Hayes, J. B., North-Morris, M., Novak, M., & Wyant, J. C. (2004). Pixelated Phase-Mask Dynamic Interferometer. *Proceedings of SPIE*, *5531*(520), 304–314. http://doi.org/10.1117/12.560807

Pixton, B. M., & Greivenkamp, J. E. (2006). Automated Hilger-Chance refractometer for index measurement of liquids. *Frontiers in Optics, OSA Technical Digest (CD) (Optical Society of America)*. Retrieved from https://www.osapublishing.org/abstract.cfm?uri=OFT-2006-OFMC7

Schreiber, H., & Bruning, J. H. (2007). Phase Shifting Interferometry. In D. Malacara (Ed.), *Optical Shop Testing*. Wiley Interscience.

Schwiegerling, J. (2014). *Optical Specification, Fabrication and Testing*. Bellingham, Washington: SPIE.

Williby, G. A., Smith, D. G., Brumfield, R. B., & Greivenkamp, J. E. (2003). Interferometric testing of soft contact lenses. *Proceedings of SPIE*, *5180*, 329–339.